TECHNISCHE
UNIVERSITÄT
DARMSTADT

Physik

Thin and Responsive Polymer Coatings:

Insight into Polyelectrolyte Multilayer and their Composites with Polyelectrolyte Brushes and Halloysite Nanotubes

Dem Fachbereich Physik
der Technischen Universität Darmstadt

zur Erlangung des Grades
eines Doktors der Naturwissenschaften (Dr. rer. nat.)

vorgelegte Dissertation von
Master of Science Oliver Löhmann
aus Nauen

Darmstadt 2018
D17

Löhmann, Oliver: Thin and Responsive Polymer Coatings
Darmstadt, Technische Universität Darmstadt
Jahr der Veröffentlichung der Dissertation auf TUprints: 2019
URN: urn:nbn:de:tuda-tuprints-84005
Tag der mündlichen Prüfung: 21.01.2019

Prüfungskommission:

Referentin: Prof. Dr. Regine von Klitzing
Korreferent: Prof. Dr. Bernd Stühn
Prüfer: Prof. Dr. Marcus Rose
Prüfer: Prof. Dr. Jens Braun

Tag der wissenschaftlichen Aussprache: 21.01.2019

TECHNISCHE
UNIVERSITÄT
DARMSTADT

Physik

Erklärung gemäß §9 Promotionsordnung

Hiermit versichere ich, dass ich die vorliegende Dissertation selbstständig angefertigt und keine anderen als die angegebenen Quellen und Hilfsmittel verwendet habe. Alle wörtlichen und paraphrasierten Zitate wurden angemessen kenntlich gemacht. Die Arbeit hat bisher noch nicht zu Prüfungszwecken gedient.

Datum und Unterschrift

Wissenschaft: Es ist nicht ihr Ziel, der unendlichen Weisheit eine Tür zu öffnen, sondern eine Grenze zu setzen dem unendlichen Irrtum.

Bertolt Brecht

Danksagungen

Zuerst möchte ich Regine von Klitzing danken, die mir die Möglichkeit gab meine Dissertation in ihrer Arbeitsgruppe anzufertigen. Samantha Micciulla danke ich herzlich für die Betreuung wärhend meiner Masterarbeit und dass sie mir zu Beginn meiner Promotionsphase mit Rat und Tat zur Seite stand. Danke für die Hilfe während der Messzeit und die stets aufmunternden Worte.

Weiterhin bedanke ich mich bei meinen (ehemaligen) Kollegen Martin Uhlig, Jens Meißner und Michael Ludwig, die in der Zeit auch zu guten Freunden geworden. Ohne euch wäre der Arbeitsalltag sehr trist gewesen und die ein oder andere Idee wahrscheinlich niemals entstanden. Außerdem danke ich allen anderen Mitgliedern und Ehemaligen des Stanski-Laboratorium an der TU Berlin sowie den Mitgliedern der Arbeitsgruppe "Weiche Materie an Grenzflächen" an der TU Darmstadt, die mir mit Rat und Tat bei größeren und kleineren Problem stets zur Hilfe kamen. Meinen studentischen Hilfkräften, allen voran Philipp Ritzert, danke ich fü die sorgfältige Arbeit und Ausdauer mit den übertragenen Aufgaben. Die Lernbereitschaft und auch die Begeisterungsfähigkeit war immer wieder Ansporn für die eigene Arbeit. Danke auch für die Geduld mit mir als Betreuer, auch wenn es mal nicht so rund lief. Vielen Dank für den angehmen Alltag im gemeinsamen Büro an Maximilian Zerball, Stephanie Christau und Michael Ludwig.

Für die erfolgreichen Kooperationen danke ich Emanuel Schneck, Olaf Soltwedel und Olivier Felix. Der Rosa-Luxemburg-Stiftung danke ich für die Unterstützung wärend des Studiums.

Weiterhin möchte ich Raphael und Johannes für die schöne gemeinsame Zeit in den Wohngemeinschaften und den wichtigen Gesprächen am Küchentisch danken. Ein lieber Dank geht auch Ana, die mir stets zur Seite steht auch wenn es mal nicht so rund läuft und auch einfach mal die Gedanken auf andere Dinge als die Naturwissenschaften lenken kann.

Abschließend danke ich meiner Familie und vor allem meinen Eltern, Cornelia und Thomas, die mir an vielen Stellen im Leben den Weg geebnet haben und ohne die dieser Abschluss nicht möglich gewesen wäre.

Wissenschaftlicher Werdegang

04/2017 - heute	Wissenschaftlicher Mitarbeiter am Institut für Festkörperphysik an der Technischen Universität Darmstadt im Arbeitskreis von Prof. Dr. Regine von Klitzing
04/2014 - 03/2017	Wissenschaftlicher Mitarbeiter am Institut für Chemie an der Technischen Universität Berlin im Arbeitskreis von Prof. Dr. Regine von Klitzing
10/2011 - 03/2014	Chemiestudium (M. Sc.) an der Technischen Universität Berlin
	Vertiefungsbereich: Materialwissenschaftliche Chemie
	Abschlussarbeit: Functionalization and characterization of solid surfaces coated by polymers
10/2008 - 09/2011	Chemiestudium (B. Sc.) an der Technischen Universität Berlin
	Abschlussarbeit: Soft functional interfaces from an amphiphilic diblock-copolymer
09/2005 - 06/2008	Ausbildung zum Chemielaboranten bei der Beiersdorf Manufacturing Berlin GmbH (ehemals Cosmed Produktions GmbH)

Wissenschaftliche Veröffentlichungen

Publikationen als Erstautor

Water Uptake of Polyelectrolyte Multilayers Including Water Condensation in Voids. Oliver Löhmann, Maximilian Zerball, and Regine von Klitzing, *Langmuir* (2018), 34 (38), 11518 - 11525, dx.doi.org/10.1021/acs.langmuir.8b02258

Swelling Behavior of Composite Systems: Mutual Effects between Polyelectrolyte Brushes and Multilayers. Oliver Löhmann, Samantha Micciulla, Olaf Soltwedel, Emanuel Schneck, and Regine von Klitzing, *Macromolecules* (2018), 51 (8), 2996 - 3005, dx.doi.org/10.1021/acs.macromol.8b00359

Publikationen als Koautor

Gold Nanoparticle Distribution in Polyelectrolyte Brushes Loaded at Different pH Conditions. Dikran Boyaciyan, Larissa Braun, Oliver Löhmann, Luca Silvi, Emanuel Schneck, and Regine von Klitzing, *The Journal of Chemical Physics* (2018), 149 (16), 163322, dx.doi.org/10.1063/1.5035554

Temperature Responsive Behavior of Polymer Brush/Polyelectrolyte Multilayer Composites. Samantha Micciulla, Olaf Soltwedel, Oliver Löhmann, and Regine von Klitzing, *Soft Matter* (2016), 12 (4), 1176 - 1183, dx.doi.org/10.1039/C5SM02256H

Transparent Aluminium Oxide Coatings of Polymer Brushes. Samantha Micciulla, XiaoFei Duan, Julia Strebe, Oliver Löhmann, Robert N. Lamb, and Regine von Klitzing, *Angewandte Chemie International Edition* (2016), 55 (16), 1521 - 3773, dx.doi.org/10.1002/anie.201511669

Table of content

List of Abbreviations and Symbols **1**

English Abstract **5**

Deutsche Kurzzusammenfassung **7**

1 Introduction **9**

2 Scientific Background **11**
2.1 Thermodynamics of Charged Polymers . . . 11
2.2 Adsorption of Polyelectrolytes . . . 13
2.3 End-grafted Polymers . . . 16
2.4 Halloysite Nanotubes . . . 18
2.5 Multicompartment Systems . . . 20

3 Experimental Section **23**
3.1 Materials . . . 23
3.2 Sample Preparation . . . 24
3.2.1 Dip Coating . . . 24
3.2.2 Spin Coating . . . 25
3.2.3 Spray Coating . . . 26
3.2.4 Brush Synthesis . . . 27
3.2.5 Preparation of Brush/PEM Composite Systems . . . 27
3.2.6 Halloysite Suspensions . . . 27
3.3 Methods . . . 28
3.3.1 Ellipsometry . . . 28
3.3.2 X-Ray and Neutron Reflectometry . . . 30
3.3.3 Atomic Force Microscopy . . . 37
3.3.4 Electrophoretic Mobility . . . 38
3.3.5 Polarization Microscopy . . . 39
3.3.6 Transmission Electron Microscopy . . . 40

4 Polyelectrolyte Multilayers: Water Uptake and Water Condensation in Voids **41**
4.1 Introduction . . . 41
4.2 Results . . . 43
4.2.1 PEM Thickness and Refractive Index . . . 43
4.2.2 Swelling Behavior . . . 44

4.2.3 Theoretical Description . . . 45
4.3 Discussion . . . 49
4.4 Conclusion . . . 51

5 Polyelectrolyte Multilayers and Brushes: Mutual Interactions and Swelling Behavior 53
5.1 Introduction . . . 53
5.2 Results . . . 55
5.2.1 Bare Brush . . . 56
5.2.2 Brush/PEM Composite . . . 58
5.3 Discussion . . . 62
5.4 Conclusions . . . 64

6 Polyelectrolytes and Halloysite Nanotubes 65
6.1 Introduction . . . 65
6.2 Results . . . 67
6.2.1 Halloysite Nanotubes and their Suspensions . . . 67
6.2.2 Orientation of HNTs on Solid Substrates . . . 68
6.3 Discussion . . . 72
6.4 Conclusion . . . 76

7 Conclusion and Outlook 77

Bibliography 81

Appendix 95

List of Abbreviations and Symbols

AFM	Atomic force microscopy
α_i	Incident angle
α_f	Final angle
α_c	Critical angle
Å	Ångström
ATRP	Atom-transfer radical polymerization
APTS	3-Triethoxysilylpropylamine
b_c	Coherent scattering length for neutrons
β	Absorption term
BTPAm	2-bromo-2-methyl-N-(3-(triethoxysilyl)propyl) propanamide
c	Concentration
d	Thickness
δ	Dispersion term
δ_p	Phase shift parallel to the plane of incidence
δ_s	Phase shift perpendicular to the plane of incidence
Δ	Ellipsometric angle
ΔG	Change in Gibbs free energy
ΔH	Change in Enthalpy
ΔS	Change in Entropy
dPSS	Deuterated polystyrene sulfonate
$\overrightarrow{E}$	Electric field vector
$\|E_p\|$	Amplitude of electric field vector parallel to the plane of incidence
$\|E_s\|$	Amplitude of electric field vector perpendicular to the plane of incidence
ϵ	Permittivity
ϵ_{min}	Minimum Lennard-Jones potential
γ	Extrinsic bound polymer fraction
GF	Gas flow rate
GIS	Grazing incidence spraying
h	Relative humidity
HNTs	Halloysite nanotubes
$Im(\rho_x)$	Imaginary part for X-Rays
$\overrightarrow{k}$	Wave vector
K	Equilibrium constant
LF	Liquid flow rate
L_n	Ligand

λ	Wave length
M_n	Number average molar mass
MonoM	Concentration referred to the monomer unit
Mt	Transition metal
M_w	Mass average molar mass
n	Refractive index
$n(h)$	exponent of the stretched exponential function
N_A	Avogadro constant
NaCl	Sodium chloride
NR	Neutron reflectometry
ν	Frequency
PAH	Poly(allylamine) hydrochloride
PDADMAC	Poly(diallyldimethyl ammonium) chloride
PE	Polyelectrolyte
PEI	Polyethylenimine
PEM	Polyelectrolyte multilayer
ϕ	Volume fraction
PMMA	Poly(methyl methacrylate)
PMETAC	Poly-2-(methacryloyloxy)ethyl-trimethylammonium chloride
PNIPAM	Poly(N-isopropylacrylamide)
Pol^-	Negatively charged polyelectrolyte
Pol^+	Positively charged polyelectrolyte
ψ	Ellipsometric angle
PSS	Polystyrene sulfonate
Q_z	Momentum transfer
r	Distance
R	Reflected intensity
r_e	Electron radius
r_f	Fresnel reflection coefficient
RH	Relative humidity
r_p	Reflection coefficient of electric field parallel to the plane of incidence
r_s	Reflection coefficient of electric field perpendicular to the plane of incidence
r_0	Distance with zero potential
ρ	Density
ρ_X	Scattering length density for X-Rays
ρ_N	Scattering length density for neutrons
RPM	Rotation per minute
RX	Alkene halogenide
S	Swelling coefficient
S_n	Nematic order parameter
SLD	Scattering length density
σ	Surface roughness
σ_j	Interface roughness

σ_{Brush}	Grafting density of polymer brushes
t	Time
T	Transmitted intensity
τ	Decay length
TEM	Transmission electron microscopy
t_f	Fresnel transmission coefficient
θ	Orientation angle in respect to the main orientation direction
V_{LJ}	Lennard-Jones potential
V	Volume
X	Ratio between transmitted and reflected intensity
XRR	X-Ray reflectometry
$\bar{z}$	Average height
z_i	Height at spot i
Z_i	Atomic number

Abstract

This thesis gives an insight into thin coatings consisting of polyelectrolyte multilayers, polyelectrolyte brushes and Halloysite nanotubes. Thin coatings are able to modify surfaces without affecting the underlying substrate. These coating can be used to protect the substrate and to introduce functionality, e.g. responsiveness to humidity or temperature.

The first part is based on polyelectrolyte multilayers (PEMs). PEMs are build up of oppositely charged polyions via the layer-by-layer technique and can be tailored with nanometer precision. These coating are not densely packed and contain air-filled holes (voids) in the dry state. The knowledge about the amount of voids is of crucial importance for future applications. Here, polystyrene sulfonate/poly(diallyldimethyl ammonium) chloride (PSS/PDADMAC) PEMs were studied at varying humidity to investigate the internal composition. Ellipsometry was used to determine thickness and refractive index as a function relative humidity. The relative swelling behavior is independent of the layer number. While increasing humidity, PEMs swell and air is replaced by water inside the voids. It was shown that above 30% RH the voids are fully filled with water. Additionally, the void fraction and refractive index of the pure polymer mater were determined to $5 \pm 1\%$ and 1.592 ± 0.002, respectively.

The second part describes the mutual interactions between PEMs and brushes. In contrast to PEMs, brushes are perpendicular orientated to the surface. Composites of brushes covered with PEMs retain their responsiveness to variation of external humidity. Therefore, this stimulus is used to study the internal composition of poly-2-(methacryloyloxy)ethyl-trimethylammonium chloride (PMETAC) brushes coated with PSS/PDADMAC PEMs. Ellipsometry measurements showed that the composites swell less than single brushes but more than single PEMs. Neutron reflectometry showed that PEMs penetrate fully a brush and stay mobile. While increasing humidity, brush and PEM start to separate and water accumulates in the transition region. The overlap of brush and PEM decreases down to 10% for a brush coated with a PEM of 17 layers. Swelling and separation are almost reversible.

The last part focuses on the orientation of Halloysite nanotubes (HNTs) on substrates coated with polyelectrolytes. HNTs are charged, tubular shaped alumosilicates and an orientation of them leads to anisotropic coatings. Here, spray coating was used to align HNTs on a surface. The influence of HNT-substrate interactions and different spraying parameters were investigated. Polyethylenimine (PEI) coated silicon wafer provided a sufficient strong interaction with HNTs for orientation on the surface. A low liquid flow rate ($0.2\ mL/min$) and a high gas flow rate ($40\ L/min$) led to best alignment. Increasing concentration and spraying time resulted in increasing coverage. The orientation was quantified by the nematic order parameter and was increased up to 0.81 by optimizing spraying conditions. Additionally, oriented bilayers of PEI and HNTs were produced.

Kurzzusammenfassung

Dünne Beschichtungen können die Eigenschaften von Oberflächen verändern, ohne die Volumeneigenschaften des Substrates zu beeinflussen. Dabei bieten vor allem Polymere eine Vielzahl an Möglichkeiten, um Oberflächeneigenschaften zu beeinflussen. Außerdem können sie zusätzlich responsive Eigenschaften aufweisen, zum Beispiel durch den Einfluss von Luftfeuchtigkeit oder Temperatur. In dieser Arbeit wird der Fokus vor allem auf die innere Struktur von Polyelektrolytmultischichten und deren Kombination mit Polyelektrolytbürsten gelegt. Weiterhin wird die Ausrichtung von Halloysite Nanoröhren auf einem Polymersubstrat studiert.

Im ersten Teil wird die interne Zusammensetzung von Polyelektrolytmultischichten (PEMs) untersucht. Diese über die Layer-by-Layer-Technik aufgebauten Schichten bilden ein Polymernetzwerk aus entgegengesetzt geladenen Polyelektrolyten. Die PEMs enthalten eine gewisse Menge an Hohlräumen. Das Quellverhalten von PEMs, bestehend aus Polystyrolsulfonat (PSS) und Polydiallydimethylammoniumchlorid (PDADMAC), wurde mit Hilfe der Ellipsometrie in Abhängigkeit von der Luftfeuchtigkeit untersucht. Das relative Quellverhalten war unabhängig von der Anzahl der Polyelektrolytschichten. Es wurde gezeigt, dass bis zu einer Luftfeuchtigkeit von 30% ein Luft-Wasser-Austausch in den Hohlräumen stattfindet. Der Volumenanteil der Hohlräume beträgt im Mittel $5 \pm 1\%$. Der Brechungsindex des reinen PEMs wurde zu 1.592 ± 0.002 bestimmt.

Im zweiten Teil wird die gegenseitige Beeinflussung von PEMs und Polyelektrolytbürsten untersucht. Dazu wurden Poly-2-(methacryloyloxy)ethyl-trimethylammoniumchlorid-Bürsten (PMETAC) mit PSS/PDADMAC PEMs beschichtet. Mit Hilfe der Ellipsometrie wurde das Quellverhalten von diesen Kompositmaterialien in Abhängigkeit von der Luftfeuchtigkeit untersucht. Es zeigte sich, dass die Komposite weniger quellen als reine Bürsten, aber mehr als reine PEMs. Um einen Einblick in die interne Struktur zu bekommen, wurde Neutronenreflektometrie verwendet. Mit Hilfe dieser Methode wurde nachgewiesen, dass die PEMs vollständig in die Bürsten diffundieren und sich bei steigender Luftfeuchtigkeit beide Komponenten voneinander entfernen. Wasser lagerte sich bevorzugt in diesem Zwischenraum ein. Dieser Prozess war nahezu reversibel.

Im abschließenden Kapitel wird die Ausrichtung von Halloysite Nanoröhren (HNTs) durch das Sprühen auf Oberflächen untersucht. Es konnte gezeigt werden, dass Oberflächen, die mit Polyethylenemin (PEI) beschichtet wurden, eine ausreichend starke Wechselwirkung für Orientierung aufweisen. Eine hohe Orientierung zeigte sich mit niedrigem Flüssigkeitsstrom (0.2 L/min) und hohem Gasstrom (40 L/min). Die Belegung wurde mit steigender Konzentration der gesprühten Suspension und längerer Sprühzeit dichter. Die Orientierung wurde mit dem nematischen Ordnungsparameter S quantifiziert. Eine Optimierung der Sprühparameter führte zu einem Ordnungsparameter von bis zu 0.81. Außerdem was es möglich orientierte Doppellagen herzustellen.

1 Introduction

Thin surface coatings are an interesting field of fundamental research with a perspective for technical applications. This can include weight reduction, responsive properties to implement functionality, or to change the morphology. Furthermore, biocompatible coatings are of strong interest for applications in medicine, food industry and cosmetics. Thin coatings have a thickness from a few nanometer up to several hundreds of nanometer. Therefore, it is of crucial importance to tailor thin coating in a very precise, and reproducible manner and to get fundamental control about the composition and responsiveness. Current research aims to understand the impact on environment and to develop smart surface coatings for future applications. Promising candidates for such thin film coatings are polyelectrolyte multilayers (PEMs) as well as polyelectrolyte brushes.

PEMs consist of alternating layers of oppositely charged polyelectrolytes adsorbed to a surface. Introduced by Decher *et al.* in the early 90's,[1,2] PEMs were intensively investigated and are still subject of current research. The process of constitution and the influence of different parameters are well understood. Among others, applications of PEMs are reported in literature for sensing,[3] antifouling coatings,[4] and anti-reflective coatings.[5]

In contrast to PEMs, polyelectrolyte brushes are orientated perpendicular to a surface. They are end-grafted on a surface either by the grafting-to or grafting-from approach. The advantage of the grafting-from approach is the higher grafting density, in particular for polyelectrolyte brushes due to their electrostatic repulsion. A sufficient high grafting density is a requirement for brushes. Otherwise the polyelectrolyte chains collapse and form mushroom or pancake-like conformations. Same as PEMs, polyelectrolyte brushes are extensively studied and the synthesis is well controllable. Therefore, they are promising candidates for different applications. It is reported that polyelectrolyte brushes are used as a matrix for catalytic active nanoparticles,[6] as synthetic membranes for selectively transporting ions[7] or as surface coatings with tunable wettability.[8]

The similar nature of PEMs and polyelectrolyte brushes allows to combine both structures. Various polyelectrolytes can be used to build up PEMs and polyelectrolyte brushes, allowing the introduction of a large variety of functionality into the coatings by combining different polymers and architectures. It is reported, that PEMs are used as substrates for brush synthesis[9] and brushes are coated with PEMs.[10] Additionally, inorganic nanoparticles of all shape, e.g. spheres, rods, and wires can be incorporated and introduce further functionality and especially anisotropy into thin coatings. During the last years, new nanoparticles came into focus: Halloysite nanotubes (HNTs). They are charged and biocompatible nanotubes which can be incorporated into a polyelectrolyte matrix or can be coated by the latter. First studies showed that it is possible to load HNTs with drugs and to retard the drug release by PEM coatings.[11]

This Ph.D. thesis aims to investigate the internal structure of thin coatings, consisting of polyelectrolyte multilayers, brushes, and Halloysite nanotubes. After giving a theoretical background (Chapter 2) and an introduction into the used methods (Chapter 3), Chapter 4 discusses the internal structure of PEMs. PEMs consist of a polymer matrix of oppositely charged polyelectrolytes and inclusions (voids) filled with a gas or a liquid. Exposed to external moisture, PEMs will adsorb water readily. This water can be distinguished into two fractions, swelling and void water. Swelling water leads to an increase in thickness and a change in permittivity. Void water replaces air in the voids of the former dry PEM which leads to a change in permittivity but does not affect the thickness. These two fundamentally different processes were monitored by ellipsometry, a sensitive tool to study the refractive index and the thickness increment while increasing the surrounding humidity. For a theoretical description, the void model was extended to correctly describe the refractive index and the thickness over the entire humidity range. It is shown that up to 30% RH an air-water exchange took place until any voids are fully filled with water. Above 30% RH a further water uptake only led to swelling of the entire film. Using this knowledge, the void fraction of the dry PEM was calculated and gave an insight into the internal composition of PEMs.

Chapter 5 examines the mutual influence between PEMs and polyelectrolyte brushes and their collective response to external humidity. Polyelectrolyte chains diffuse inside a polyelectrolyte brush during formation of PEMs on top. These chains stay mobile inside the brush. By increasing humidity, the entire system started to swell as shown by ellipsometry measurements. Compared to the swelling behavior of single PEMs and brushes, the composite showed an intermediate swelling behavior. Using neutron reflectometry, it was possible to resolve the internal structure of the composite during water adsorption, showing that the interdigitated components started to separate with increasing humidity. It was possible to show that this separation process was almost reversible after a full adsorption cycle.

Chapter 6 addresses the interplay of Halloysite nanotubes (HNTs) and polyelectrolytes. HNTs are tubular shaped nanoparticles consisting of aluminosilicates. As a consequence of their specific structure, HNTs have an intrinsic anisotropic surface chemistry with alumina predominating the inner surface and silica predominating the outer surface resulting in an allover negative charge. An alignment of HNTs on a substrate introduces anisotropic properties to thin coatings. Here, it was shown that HNTs align on a surface by grazing incidence spraying. It was possible to manipulate the orientation and coverage by varying different parameters. The samples were mainly analyzed with atomic force microscopy and polarization microscopy. The orientation was quantified by calculating the nematic order parameter.

Conclusively, Chapter 7 finishes this thesis with a conclusion of the different chapters by giving an outlook to possible applications and discussing open questions.

2 Scientific Background

The following chapter introduces the scientific background of this work. This includes the integration into former and recent research as well as important fundamental concepts. The main part of this work is related to surface coatings containing polyelectrolytes (PEs). Therefore, the first paragraph deals with the main driving forces of PE complexation. The second part gives insights into the driving force of the build-up and into the structure of polyelectrolyte multilayers (PEMs). A further building block of nanostructures, polyelectrolyte brushes, is introduced in the third part of this chapter. Afterwards, Halloysite nanotubes (HNTs), an inorganic, stiff material which can be combined with PEs get into focus. Finally, multicompartment systems consisting of PEMs/brushes and PEMs/HNTs are addressed.

2.1 Thermodynamics of Charged Polymers

Oppositely charged PEs build complexes in aqueous solutions.[12] PEs are surrounded by an electrical double layer. During complexation, the double layer is destroyed and small counterions are released.[13] This can be described by the change in Gibbs energy ΔG.

$$\Delta G = \Delta H - T\Delta S \tag{2.1}$$

The change in enthalpy ΔH is mainly correlated to the binding energy of PEs; and the change in entropy ΔS is mainly influenced by a release of counterions. This process is shown in Figure 2.1. Depending on the used polyelectrolytes, the change in enthalpy can have a positive or negative sign. The change in entropy is likely to be positive because the release of counterions predominates the loss in translational entropy of single PE segments. Therefore, the change Gibbs energy can either be negative or positive according to Equation 2.1 and thus PEs can build stable or non-stable complexes, respectively. Stable complexes mostly lead to phase separation or to turbidity of the solution.

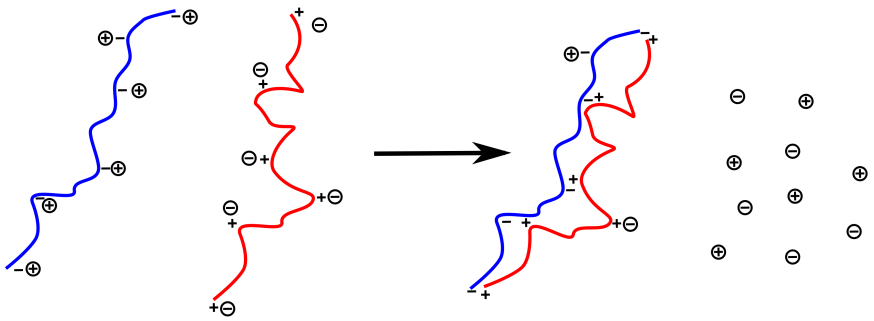

Figure 2.1: Complexation of oppositely charged polyelectrolytes. The release of counterions is the main driving force during the electrostatic complexation.

Both, ΔH and ΔS, are strongly influenced by the concentration of salt in the solution. An increase of salt concentration leads to a decrease of entropy gain but the sign remains positive.[14] The change in enthalpy increases with increasing salt concentration and shift from negative to positive values can be observed. Increasing the salt concentration leads to a lower amount of intrinsic bonds and less tight ion pairing and thus to a shift from exothermic to endothermic complexation. Nevertheless, a high entropy gain can compensate an endothermic complexation and thus, the counterion release is the main driving force of PE complexation. Additionally, the type of counterions as well as the type of external added salt influences the complexation. The influence of the anions is generally greater than the influence of the cations.[15] According to the Hofmeister series,* chaotropic anions strongly screen the PE charges and lead to a more coiled conformation. In contrast, cosmotropic anions lead to a more stretched conformation and thus to more compact complexation.

Furthermore, the complexation is influenced by the charge density of PEs. The charge density of PEs describes the number of ionic groups per monomer. These charged groups can be compensated intrinsically by another PE or extrinsically by a small counterion. A chemical equilibrium, considering sodium chloride as added salt as used in the following studies, is defined as

$$Pol^{-}Pol^{+} + Na^{+} + Cl^{-} \rightleftharpoons Pol^{+}Cl^{-} + Pol^{-}Na^{+}. \tag{2.2}$$

On the left hand side, the PE charges are intrinsically compensated where the binding sites of the positively charged PEs Pol^{+} are compensated by the binding sites of the

*The Hofmeister series is: $ClO_4^- > SCN^- > I^- > NO_3^- > Br^- > Cl^- > CH_3COO^- > HCOO^- > F^- > OH^- > HPO_4^{2-} > SO_4^{2-}$.[16]

negatively charged PE Pol^-. On the right hand side, the PE charges are extrinsically compensated by small counterions. With that, the equilibrium constant K is[17]

$$K = \frac{\gamma^2}{(1-\gamma)[NaCl]^2}. \tag{2.3}$$

The extrinsic bound PE fraction γ is the amount of binding sites compensated by counter ions. Increasing the salt concentration lowers the equilibrium constant and leads to a dissolution of the complexes. The polymer rigidity (backbone rigidity) of single PE influences accessibility of the binding sites and is described by the persistence length of a polymer. The higher the charge density the higher the electrostatic repulsion along the PE chains which results in more stretched chain conformation. Polyelectrolytes used in this study have a comparably low persistence length. The persistence lengths of polystyrene sulfonate (PSS) and poly(diallyldimethyl ammonium) chloride (PDADMAC) are about 1 nm and about 2.5 nm, respectively.[18,19] In contrast, deoxyribonucleic acid (DNA) has a persistence length of 50 nm.[18]

The type of polymer, in particular the chemical composition, influences strongly the complexation. Here, hydrophobic interaction, additionally to electrostatic interactions, between the PEs is important for complexation and strong hydrophobic interactions favor complexation. A further aspect is the PE chain length or in other words the molar mass of PEs. Shorter chains tend to redissolve faster, however, a careful adjustment of PE and salt concentration can lead to stable complexes.[20] Furthermore, the solubility of the polymers is decisive. Commonly used polyelectrolyte are soluble in water and many other polar solvents like methanol and ethanol. The solvent quality is defined by the interaction between the monomer units and solvent molecules. If the interaction between monomer and solvent is favored the solvent is a good solvent. A bad solvent favors the interaction between the monomers. If the chemical potential between monomers and solvent molecules is zero, the solvent is a theta solvent. These solvent properties leads to different conformation of polymers. A bad solvent leads to a more coiled conformation while a good solvent leads to a more stretched conformation. The latter enhances the accessibility of the binding sites along the polymer chain. Further effects, like temperature, electric and magnetic fields can also influence the complexation. As none of these effects are relevant for the polyelectrolytes used in this thesis, these effects are not further discussed.

In general, insoluble PE complexes occur by mixing two oppositely charged PEs. This phenomena is used to deposit PEs on charged surfaces in a controlled manner. The shape or composition of the surface are of minor importance for adsorption. Therefore, it is possible to adsorb PE on flat or curved surfaces[21,22] as well as on hard or soft substrates.[23,24]

2.2 Adsorption of Polyelectrolytes

Polyelectrolytes are able to adsorb on an oppositely charged surface just by immersing the substrate into a PE solution. Repeating this procedure with oppositely charged PEs leads

to polyelectrolyte multilayers (PEMs). This well-known and easy method is called layer-by-layer technique and is first described by Decher *et al.*[1,2] The consecutive adsorption can also be realized by spin coating[25] or spray coating.[26] The different advantages and drawbacks are discussed in Chapter 3 where the different methods are introduced. PEMs are physically adsorbed on a surface and the build-up is governed by the same parameter as discussed for the PE complexation in bulk solution. Thus, PEMs desorb from the substrate by highly concentrated salt solutions.[27] The thickness of PEMs can be tailored on a sub-nm level by adjusting the parameter of dipping procedure.[28,29] The growth by layer deposition can be described either by an exponential or a linear behavior and is differentiated by the thickness increment per deposited layer.[30] Exponential growth occurs when the thickness increment increases with increasing layer number. Otherwise, linear growth is obtained. Porcel *et al.*[30] suggested a model for PEM growth consisting of three different zones as shown in Figure 2.2.

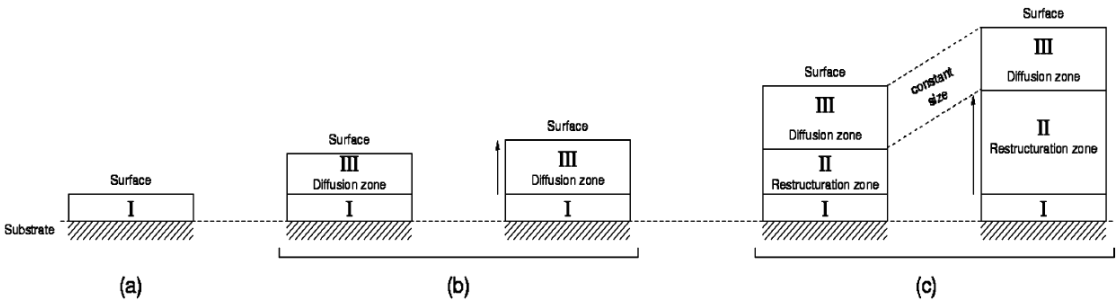

Figure 2.2: Build-up mechanism according to the zone model. (a) Starting layer deposition, the first layer pairs are strongly influenced by the substrate and build up zone I. (b) Further deposition leads to a less compact layer where the PE chains are able to diffuse inside the PEM. The constitution of this zone III induces an exponential growth. (c) When the PE chains are not able to diffuse through the entire PEM while depositing further layer the reconstruction zone is formed (zone II). This leads to a switch from exponential to linear growth. Scheme is adopted from Porcel *et al.*[30]

The first zone is located in direct contact to the substrate. Its behavior is mainly influenced by the substrate and this zone is only a few layers thick. By further PE adsorption the PEM growth and newly generated layers are not affected by the substrate. This allows polymer mobility and looser packing. Therefore, this zone is called the diffusion zone. Here, the layer increment increases with further layer deposition. This results in an exponential growth regime. Within this zone, PE chains are able to diffuse through the entire film because the PEMs are swollen inside the dipping solution and the polymer network is widened. The thickness of the diffusion zone is characteristic for the given PEs and independent from the substrate. When the overall thickness of the PEM exceeds the sum of zone I and the characteristic thickness of zone III the PEs are not able to diffuse through the entire film. Thus, the reconstruction zone (zone II) between zone

I and III arises. Further adsorbed PEs are not able to diffuse into this zone and the layer increment is constant with further layer deposition. Therefore, a shift from exponential to linear growth occurs.[30–32] The assumption that PEMs are inhomogeneously distributed perpendicular to the surface is confirmed by neutron reflectivity measurements.[33] It was shown that the thickness per layer is lower near the substrate than near the PEM interface. PEMs do not build up a compact dense coating and with that, it is important to gain insight into the internal structure for further applications.

PEMs are sensitive to external stimuli, e.g. temperature,[34,35] humidity,[36–38] pH,[39] salt,[40] or external fields.[41] The response of the PEM-functionalized surfaces to variations in environment is essential for technical applications.[42] Especially for medical application, it is of crucial importance to control the interaction between drugs and living organisms.[43,44] Here, PEMs can be used as a mediator to avoid side effects. Hossfeld *et al.* proved that PEMs decreases the adhesion of blood cells. This leads to an inhibition of thrombosis on implanted stents.[45] Furthermore, PEMs can be used to trigger cell growth. Salloum *et al.* reported that different PEMs influence the cell growth of smooth muscle cells and that a patterned surface triggers directional growth.[46]

This work focuses on improving the understanding of the responsiveness of PEMs to water. For that, the changes in thickness and optical properties of PEMs are available parameter to investigate their behavior. PEMs act like a sponge by providing water in humid air or in liquid form. It was shown that polystyrene sulfonate/poly(allylamine) hydrochloride (PSS/PAH) PEMs swell in a nonlinear behavior.[36,37] Different models are reported in literature to describe the swelling behavior.[47] The thickness model, based on the dry and swollen thickness, assumes that amount of incorporated water ϕ_{swell} leads only to a change in thickness.

$$\phi_{swell} = \frac{d(h) - d_{dry}}{d(h)} \tag{2.4}$$

Later on, neutron reflectometry (NR) showed that the total amount of incorporated water does not only lead to an increase in thickness. Hence, the density model was proposed which describes the amount of water by the change in optical properties. The amount of incorporated water ϕ'_{swell} can be described by the change in scattering length density (SLD).

$$\phi'_{swell} = \frac{SLD(h) - SLD_{dry}}{SLD_{H_2O} - SLD_{dry}} \tag{2.5}$$

A mismatch between ϕ_{swell} and ϕ'_{swell} was found for PSS/PDADMAC PEMs.[48] It was shown that the total amount of adsorbed water is the sum of two different fractions of water in a PEM: void and swelling water.[40,47] The void water fills the cavities (voids) between the PE chains which exist also in vacuum. This amount of water changes optical properties, e.g. the SLD or the refractive index, but does not lead to a swelling of the PEM. The swelling water leads to a swelling of the PEM and changes the optical properties. To describe the void fraction inside PEMs, two different approaches were applied: The Garnett model and the void model.[47,49] The Garnett model leads not to an

exact description because it assumes a two component system which is not the case for a system of PEM, air and water.[50,51] The void model takes into account that the voids can be filled either by air or water. Applying the void model, the void water of PSS/PAH PEMs is found to be 0.12.[47] Furthermore, NR experiments showed that the water is inhomogeneously distributed along the surface normal.[52] Near the substrate less water is absorbed. While increasing the distance from the surface more water can be absorbed and water adsorption reaches the maximum near the PEM interface. The amount of swelling water increases with increasing the ionic strength and increasing size of anions during preparation.[53] Both trends are ascribed by an increase of the extrinsic charge compensation which allows an easier rearrangement and a stronger swelling of PEMs.[54] The void water shows the opposite effect. This means that the density of dry PEMs increase due to a stronger chain coiling in solution. Combining ellipsometry and quartz crystal microbalance with dissipation gives information about the swelling behavior in a liquid environment. The swelling in salt solutions with different concentration is fully reversible with changing the salt concentration.[55] The water content for PSS/PDADMAC can reach a maximum up to 70% in a 0.5 M NaCl solution.

PEMs influence the interaction between a surface and the environment. Recent published results showed the importance of tailoring the internal structure. On the one hand, ice propagation on solid surface is reduced by PEMs and therefore PEMs avoid damage of the surface.[56] On the other hand, PEMs can be used to protect the environment against the influence of the surface. It was shown that PEMs coated stents lowers adsorption of blood cells and thus, it inhibits thrombosis after stent implantation.[45] Furthermore, PEMs are used as a responsive matrix for controlled release. Polylactic acid sealed PEMs were used as a matrix for a controlled release of Rhodamine B by ultra sound.[57] These examples show that the internal structure is of crucial importance for the technical application because the interaction and responsiveness of PEMs is dependent on the PEM's constitution.

Chapter 4 deals with the swelling behavior and theoretical description of the internal composition of PSS/PDADMAC PEMs. It is shown that void model can also be used to evaluate ellipsometry data, namely thickness and refractive index.[49] Nevertheless, the void model cannot describe precisely the trend of refractive index over the entire humidity range. Therefore, the void model was extended. This extended model reproduced the experimental data over the entire humidity range to evaluate the measured refractive indices. Additionally, the void fraction and the refractive index of the pure polymer matrix without voids were calculated.

2.3 End-grafted Polymers

In contrast to physisorbed PEMs, polyelectrolytes can also be chemically end-grafted to a substrate.[58] Thereby, two different methods, the grafting-to[59] and the grafting-from approach,[60] are established. The grafting-to approach is based on end-functionalized polymers tethered covalently to a substrate. This methods typically results in a low grafting density due to steric and electrostatic repulsion of the individual polymer chains

during formation of the polymer-substrate bond. This can be overcome by the grafting-from approach. Here, the initiator is linked to the substrate and the polymerization leads to a polymer growth perpendicular to the surface.[61] This results in a higher grafting density because the individual binding sites are occupied before the chain growth. The grafting density σ_{Brush} is defined by

$$\sigma_{Brush} = \frac{d\rho N_A}{M_n} \tag{2.6}$$

where d is the thickness of the polymer layer, ρ the polymer density, and M_n the molecular weight.[62,63] Thus, σ_{Brush} describes the number of polymer chains per surface area. The grafting density and molecular weight cannot be simultaneously determined for the grafting-from approach. For that, the grafting density of the initiator has to be determined before the polymerization or the molecular mass has to be determined by cleaving the polymer-substrate bond. Both methods introduce some uncertainties because they cannot used in-situ. The grafting density can be easily tuned by using different initiator concentration[64] or a mixture of initiator and "dummy" molecules, which are chemically similar to the initiator but do not participate during polymerization.[65] End-grafted polymers can have different conformation on the surface, namely pancake, mushroom, and brush conformation. At low grafting densities the individual polymer chains do not interact with each other and will lay flat on the surface, resulting in a pancake conformation. By increasing the grafting density, the polymer chains start interacting with each other. Due to steric and in case of polyelectrolytes strong electrostatic repulsion the chains will stretch away from the surface and a mushroom conformation is observed. A brush is formed if the grafting density is smaller than twice the radius of gyration of the free polymer.[66] Beside homopolymer brushes, it is also possible to synthesize heteropolymer brushes with random[67] or block[68] distribution. With this strategy, brush synthesis and structure can be arbitrarily complex, and thus it is possible to synthesize brushes sensitive to different stimuli. Among different techniques of the grafting-from approach, atom-transfer radical polymerization (ATRP) is suitable to synthesize brushes. Therefore, the initiator is linked directly to the surface. Figure 2.3 shows the typical reaction scheme for the ATRP.[69]

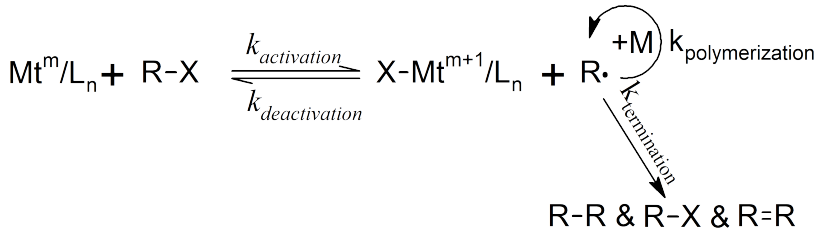

Figure 2.3: Reaction scheme of an atom-transfer radical polymerization.

The covalently bound initiator contains a carbon-halogen bond RX which can be cleaved by transition metal Mt^m. The transition metal Mt^m is oxidized to Mt^{m+1} during the homolytic cleavage of the RX-bond. A radical is formed at the end of the initiator or the end of the polymer chain. The double bond of the monomer reacts with this radical and extends the surface linked initiator or the polymer chain of one monomer unit. The unpaired electron of the radical at the end of the polymer chain reacts with a further monomer unit and a chain growth is observed. The degree of polymerization is controlled by the reaction time. Proper quenching terminates the radical polymerization resulting in defined chain length. The polymerization can be fine-tuned by the transition metal ratio, Mt^{m+1} to Mt^m, as well as by type and concentration of ligand, counterions, solvent, or initiator. The ratio Mt^m/Mt^{m+1} influences the polymerization ratio because only the reduced form is catalyticly active and the first reaction step is reversible.[70] Additionally, it is necessary to add a ligand L_n to avoid a precipitation of the transition metal.[61,71]

Brushes are responsive to various external stimuli and can undergo structural changes,[72,73] which renders them promising building blocks for smart coatings in chemical sensing and drug delivery.[8,74] In this work, ATRP was used to build up Poly-2-(methacryloyloxy)ethyl-trimethylammonium chloride (PMETAC) brushes. PMETAC brushes are strong polyelectrolytes and are sensitive to external humidity. These brushes were used as a soft substrate for PSS/PDADMAC PEMs adsorption. The resulting multicompartment systems are introduced in the last paragraph of this chapter.

2.4 Halloysite Nanotubes

Halloysite nanotubes (HNTs) are natural clay minerals and can be exploited from mines.[75] The internal structure is shown in Figure 2.4 and is similar to kaolinite where tetrahedral sheets of silica are linked through oxygen atoms to octahedral sheets of alumina. The difference in the crystal structure leads to a bending of the sheets and this results in a roll up into tubes.[75] Within these sheets water can be incorporated. The chemical formula is $Al_2Si_2O_5(OH)_4 \times nH_2O$ where the number of hydrate water molecules dictates the interlayer distances. The hydrated form with $n = 2$ results in an interlayer distance of 1 nm and the dried form with $n = 0$ results in an interlayer distance of 0.7 nm. The latter one is obtained by heating up the native HNTs.[75]

The length and diameter of HNTs depend on the mine. HNTs, used in this work, were obtained from a Chinese and an American mine. The length varies from 500 nm to 1.5 μm, the external diameter varies from 50 nm to 100 nm and the internal diameter from 10 nm to 20 nm.[75] This results in an aspect ratio of about $5-40$. HNTs dispersed in water lead to semi-stable suspensions. Therefore, their suspensions can partially treated as colloids. As defined by Thomas Graham, colloids have a low diffusion coefficient and fail to sediment due to gravity. This results in a length of the dispersed particles from approximately 1 nm up to 1 μm. The diameter of HNTs is in between this range but the length is partially longer. Thus, suspensions of shorter HNTs are colloidally stable while longer ones start to sediment.

A well-known example of elongated nanotubes are carbon nanotubes.[76] The main dis-

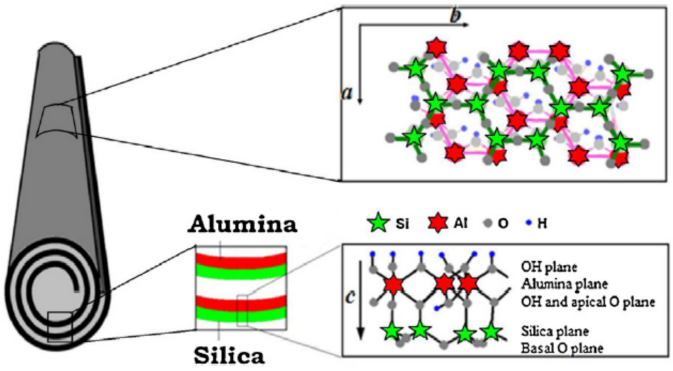

Figure 2.4: Internal structure of HNTs. Figure is adopted from Lvov *et al.*[75]

advantages for technical applications of carbon nanotubes are health hazard and high costs.[77,78] This can be overcome by the use of HNTs which are cheap and biocompatible.[75,79] The different surface properties of the inner and outer surface offer the possibility of selective surface modification. The outer surface is predominated by silica and negatively charged at intermediate pH. In contrast to the outer surface, the inner surface is predominated by alumina and positively charged at intermediate pH. Due to different surface charges, it is possible to load the inner volume (lumen) with negatively charged polymers,[80] surfactants,[81] alkanoates[82] or drugs.[83] Cavallaro *et al.* showed that anionic surfactants adsorb at the inner surface.[81] This results in a decrease of the net charged and increase of the colloidal stability of the suspension. Furthermore, they showed that cationic surfactants adsorb at the outer surface, resulting in a decrease of the colloidal stability due to less electrostatic repulsion of the dispersed particles. But not only electrostatic interactions can be used for selective modification. Yah *et al.* showed that octadecylphosphonic acid binds selectively to the inner alumina surface of HNTs.[84] Furthermore, catechol groups are used as anchors to synthesize polymer brushes on the inner surface.[85] The encapsulation of drugs inside the lumen or blocking of the lumen is achieved by different approaches. Joshi *et al.* reported on HNTs used as containers for corrosion inhibitors.[86] Veerabadran *et al.* showed that PEMs build up directly on HNTs are able to retard drug release.[11] Here it is worth to mention, that HNTs can be part of layer-by-layer structures and thus a part of multilayers. Moreover, Levis *et al.* reported of drug loaded HNTs coated with chitosan. This approach leads to retarded release of drugs.[87]

The bottom-up approach allows to build up well tailored structures based on small repetitive units.[88,89] In this work, HNTs were combined with PEs. Furthermore, an orientation of HNTs on a surface was studied and optimized. HNTs are a versatile material and can be multifunctional building block for bottom-up superstructures.

2.5 Multicompartment Systems

PEMs, brushes and HNTs can be combined in different compositions to obtain multicompartment surface coatings. These combinations lead to new properties and enhance or suppress one or more properties of the single compartments.

The combination of end-grafted brushes and adsorbed PEMs has been exploited for the design of robust, multifunctional coatings.[10,24] Tailored structural rearrangements of composites upon specific stimuli could potentially be used for chemical sensing, molecular recognition, or to trigger the uptake and release of substances. Composites of polyelectrolyte brushes and PEMs open novel technological applications in which PEMs are used as sacrificial layers to protect and release embedded molecules under certain conditions.[90,91] As Rühe and co-workers demonstrated, polyelectrolyte brushes are suitable as substrates for PEMs,[24] accounting for a pronounced diffusion of the first layer into the brush. This creates an intermixing zone between the two compartments. Nevertheless, complete charge compensation does not occur. Therefore, oppositely charged polyelectrolytes further adsorb and a PEM is built up via the layer-by-layer technique.[92,93] For brushes with high grafting and charge densities, the resulting brush-supported PEMs are found to be homogeneous.[24,92] A general structure of PEM coated brushes is shown in Figure 2.5.

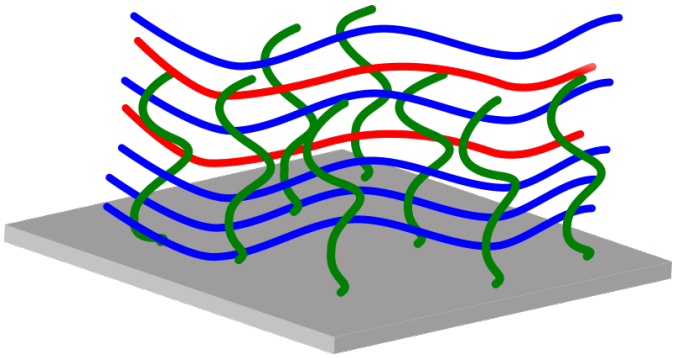

Figure 2.5: Composite build-up of a strong polyelectrolyte brush (green) and a PEMs consisting of negatively charged (blue) and positively charged (red) PEs as an example for multicompartment systems.

It shows the mixing of a strong PE brush covered with a PEM. Recent studies on brush/PEMs composites featuring temperature sensitivity reveal that mutual interdiffusion and the ensuing molecular interactions are responsible for their responsive properties. Detailed insight into the internal structure of polymer composites is of crucial importance to the design of functional coatings with desired properties.[10] Part of this work focuses on the understanding of the response of PMETAC brushes and PSS/PDADMAC PEMs to external humidity. The characterization of the swelling behavior of brush/PEM composites was compared to the single, individual components. Furthermore, the influence of the PEM thickness on the structure and properties of the composites was investiga-

ted.[61,94] Ellipsometry and neutron reflectometry (NR) were used to study the change in structure with varying humidity. It was possible to understand the level and relevance of mutual interactions between the two compartments.

Over the last years the incorporation of inorganic particles into a polymer matrix moved into the focus of scientific attention.[95–98] Responsive polymers can be also triggered after the incorporation of inorganic nanoparticles. As an example, strong polyelectrolyte brushes show pH sensitivity by incorporating pH sensitive gold nanoparticle.[99] Furthermore, clays can modulate different properties of thin coatings, e.g. mechanical strength, optical properties or thermal stability. These multicompartment systems can be tailored in a very specific way. As one example, the composites of montmorillonite clay nanosheets and poly(N-isopropylacrylamide) (PNIPAM) show that the temperature response of PNIPAM is preserved and new properties like a decrease in permeability are introduced.[100] Nevertheless, the used sheets are isotropic in planar dimensions and the modulation of the properties is isotropic in lateral direction. HNTs can also be incorporated into a polymer matrix. The incorporation of HNTs into PEMs opens the possibility to build up multicompartment systems with an anisotropy in lateral direction. Introducing anisotropic properties by using elongated particles can be achieved by grazing incidence spraying (GIS).[101–104] It is reported that spraying under grazing incidence angles leads to an orientation of silver nanowires.[104] The high aspect ratio of silver nanowires of about 90 is beneficial for a well ordered coating but from a sustainable and biocompatible point of view silver nanowires are not suitable. To overcome this problem, HNTs can be used as a replacement for silver nanowires. Although HNT have a low aspect ratio of $5-40$, Zhao *et al.* showed that HNTs loaded with PSS are able to self-assemble to an ordered film at the rim of an evaporating suspension droplet.[80] The successful alignment can be the basis to build up multilayer with a superstructure and therefore, to implement completely new surface properties. This can result in mimicking natural structures.[105] With that, a cheap and biocompatible alternative to carbon nanotubes or silver nanowires arises.

The orientation of an assembly is quantified by the nematic order parameter S_n.[101]

$$S_n = \langle 2\cos^2\theta - 1 \rangle \tag{2.7}$$

Here, θ is the angle of each particle in respect to the mean orientation direction. Random distribution leads to $S_n = 0$, while perfect alignment leads to $S_n = 1$.

Chapter 6 focus on the orientation of HNTs. Therefore, HNT were loaded with PSS to increase the electrostatic repulsion. Pristine and loaded HNTs were characterized by transmission electron microscopy (TEM) and zeta potential measurements. Afterwards, HNTs were sprayed on polyethylenimine (PEI) or PSS/PDADMAC PEM coated surfaces under grazing incidence. Figure 2.6 shows a scheme of a HNTs monolayer on a coated substrate. PEI, a positively charged polymer, showed a sufficient strong interaction with HNTs and was used to increase the adhesion of the HNTs to the substrate and between the layers of HNTs during spraying. Spraying conditions were optimized to obtain homogeneous, anisotropic monolayer and bilayer of HNTs. HNTs were successfully aligned on the surface over several hundreds of micrometer. The coatings were characterized

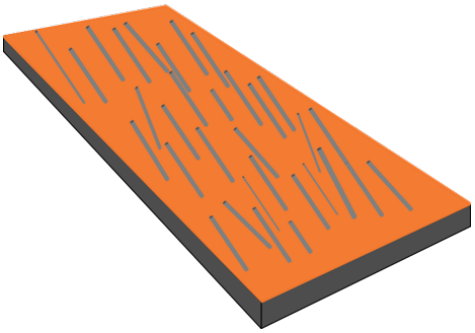

Figure 2.6: Scheme of HNTs aligned on a PEI coated substrate.

with atomic force microscopy (AFM) and optical polarization microscopy. The successful alignment can be the basis to build up multilayer with an anisotropic superstructure and therefore to implement completely new surface properties. Furthermore, a cheap and biocompatible alternative to carbon nanotubes or silver nanowires arises to mimic natural structures.[105]

3 Experimental Section

3.1 Materials

Polystyrene sulfonate sodium salt (PSS, $M_w = 70000\ g/mol$), polyethylenimine (PEI, $M_w \approx 2000\ g/mol$, 50 % in H_2O), 2-(methacryloyloxy)ethyl-trimethylammonium chloride (METAC, $M_w = 207.70\ g/mol$, 80 % in H_2O), toluene (99.9 %), bipyridine ($\geq$ 99 %), copper(I) chloride ($\geq$ 99 %) and copper(II) chloride (97 %) were purchased from Sigma-Aldrich (St. Louis, MO, USA). Hydrogen peroxide, sulfuric acid, and methanol were purchased from Th. Geyer (Renningen, Germany). Sodium chloride (NaCl, > 99.99 %) was purchased from Merck (Darmstadt, Germany). Deuterated poly(styrene sulfonate) (dPSS, $M_w = 78300\ g/mol$, $PDI \leq 1.20$) was purchased from Polymer Standard Service (Mainz, Germany). Polydiallyldimethylammonium chloride (PDADMAC, L121: $M_w = 105000$ g/mol, L124: $M_w = 135000\ g/mol$) was a kind gift from A. Laschewsky (Fraunhofer Institute of Applied Polymer Research, Potsdam, Germany). The synthesis is described elsewhere.[19] In contrast to commercial available PDADMAC, the one that is used here has a lower polydispersity and fewer side chains. Halloysite nanotubes were a kind gift by Yuri Lvov (Louisiana Tech University, LA , USA) and obtained from an American and a Chinese deposit. Except for PSS used in Chapter 6, chemicals were used without further purification. Therefore, PSS was purified by pressure filtration (Tank 17530, Sartorius, Göttingen, Germany) equipped with an ultra-filtration cell (Amicon 8400, Merck, Darmstadt, Germany, cutoff 30000 g/mol). For that, 10 g PSS were diluted in 250 mL of water and were purified under a pressure of $1.5 - 2\ bar$ with 2.88 L water and a flow rate of 2 mL/min for 24 h. After freeze drying, a yellowish, fluffy solid was obtained.

The synthesis of the initiator 2-bromo-2-methyl-N-(3-(triethoxysilyl)propyl) propanamide (BTPAm) was done in the lab of Regine von Klitzing (TU Darmstadt, Germany) as described by Laurent *et al.*[93] Milli-Q water (Millipore, Merck, Darmstadt, Germany, 18.2 $M\Omega\ cm$) was used as a solvent throughout all studies. As substrates Silicon wafers (100) from two different suppliers were used. Studies, reported in Chapter 4, were carried out on wafers from Micro chemicals GmbH (Ulm, Germany, 1-side polished, boron-doped). In all other studies, coatings were examined on wafers purchased from LG Siltron INC (Korea, 2-side polished, boron-doped). The wafers were cut into pieces depending on the measurement and purpose. Polished silicon blocks of $(7 \times 3.5 \times 1)\ cm^3$ (Siltronic AG, Munich, Germany) were used as planar substrates for neutron reflectometry.

3.2 Sample Preparation

This work focuses surface coatings with different stimuli responsive polyelectrolytes with and without the addition of inorganic nanoparticles. For this purpose, different coating techniques were applied. They are well established in the last decades and have their specific advantages and disadvantages. This will be discussed in the following paragraphs. Prior to the coating, silicon substrates were cleaned by etching with piranha solution (H_2O_2/H_2SO_4 1:1) for 30 *min* followed by intensive rinsing with water. Afterwards, the substrates were stored in water at most for 5 *h* to ensure a constant silicon oxide thickness.

3.2.1 Dip Coating

This method is based on dipping a substrate into a solution or dispersion of a material which will be deposited on the respective surface. Independent of the geometrical shape, charged surfaces can be coated with polyelectrolytes via the layer-by-layer technique. First described by Decher *et al.*[1,2] oppositely charged polyelectrolytes build up PEMs by consecutive adsorption. Here, the deposition is independent of the withdraw velocity because the deposition occurs while the substrate is immersed in the solution. Drawbacks of this method are high consumption of the respective solution and the long equilibration time for each adsorption step.

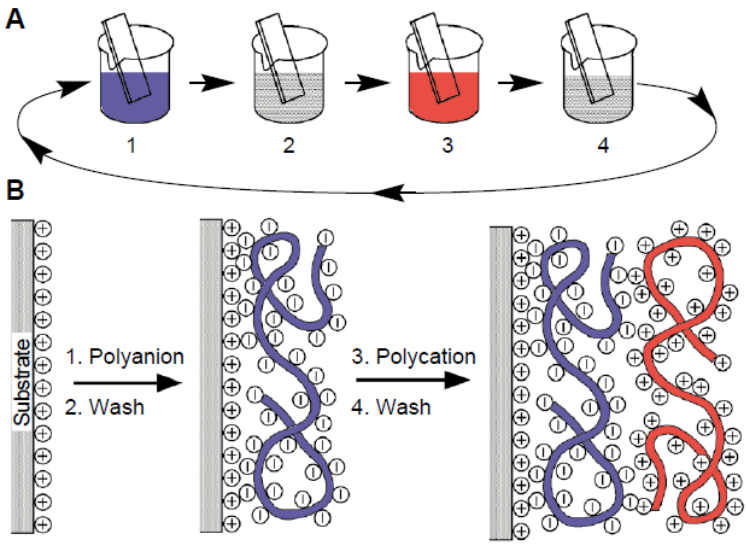

Figure 3.1: Consecutive adsorption of polyelectrolytes leads to the formation of multilayer. Scheme is adopted from Decher.[2]

Figure 3.1 shows a typical dipping procedure. A charged substrate is immersed into a solution containing polyelectrolytes (1). Followed by a rinsing step (2), the substrate

is immersed into a solution containing an oppositely charged polyelectrolyte (3). After a second rinsing step (4), a double layer is adsorbed. Rinsing steps are necessary to remove loosely bounded polyelectrolytes. This procedure is repeated until the desired layer number is reached. The adsorption can be tuned with nanometer precision leading to well-defined PEMs. Typical parameters, which are adjusted during preparation, are the dipping time, concentration and type of the used polyelectrolytes, the type and concentration of added salt, temperature, and pH. The influence of the different parameter is discussed in Chapter 2.

Here, silicon substrates ($1 \times 3\ cm^2$) were coated with a dip robot (Riegler & Kirstein, Berlin, Germany). PEI was used as a precursor to achieve better adsorption of the PEMs and a more homogeneous coating.[106] Therefore, a 0.01 $monoM$* solution of PEI was prepared in which the wafer was immersed into the solution for 30 min and rinsed three times with water afterwards. The precursor does not count as a layer. Subsequently, a 0.01 $monoM$ solution of PSS and a 0.01 $monoM$ solution of PDADMAC were prepared in 0.1 M sodium chloride solution. PEM were build up by immersing PEI coated substrates into the PSS solution for 20 min and rinsed three times with water for 1 min. Then, the samples were immersed into the PDADMAC solution for 20 min and rinsed again three times for 1 min. Dipping and rinsing were repeated until the desired number of layers was reached. For neutron reflectivity measurements, the dipping procedure was performed manually with same concentrations and intervals since the wafers for neutron reflectometry are too big and too heavy for the dip robot.

3.2.2 Spin Coating

Spin coating is a fast method to coat planar surfaces. It is possible to coat large areas with a low amount of solution within seconds. This is an advantage over dip coating because one dipping step takes several minutes and consumes much more solution per coated area. Unfortunately, using curved surfaces leads to inhomogeneous coatings and thus this method is limited to planar surfaces. As shown in Figure 3.2 the surface is mounted on a rotatable sample holder and covered with a polymer solved in a volatile solvent. During rotation, excess solution is sheared of and the remaining solvent evaporates. As residual a homogeneous polymer film is observed. The thickness of the coating depends on the polymer concentration, the rotation speed and time, the viscosity, and vapor pressure of the solvent.[107]

In this work, spin coating was used to modify the substrates before spray coating with Halloysite nanotubes. Therefore, freshly etched silicon wafers ($2 \times 4\ cm^2$) were coated with a 0.01 $monoM$ solution of PEI with 2000 rpm for 30 s. This leads to a charge reversal of the substrate and thus, it is possible to adsorb negatively charged HNTs. Spin coating was preferred over dip coating and spray coating because it was less time and solution consuming.

*concentration referring to the monomers

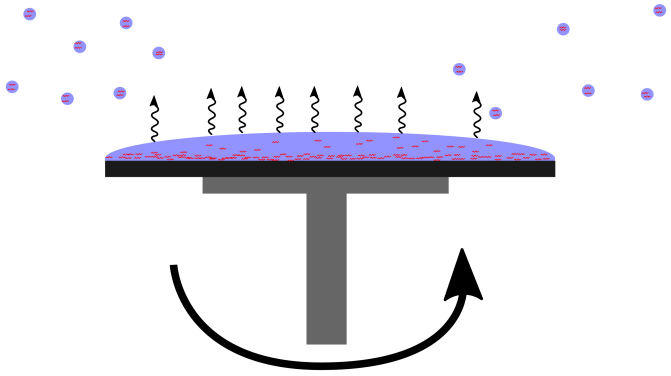

Figure 3.2: Spin coating of a polymer (red) solved in a volatile solvent (blue).

3.2.3 Spray Coating

For industrial applications it is important to decrease preparation time. In previous studies it was shown that the layer-by-layer built-up is also possible via spray coating.[26] The same solutions are suitable as used for dip coating. The preparation time decreases from several minutes to only a few seconds per layer. A more systematic study was carried out but some parameter are still not well controllable.[108] Additionally, larger areas can be coated with less solution because the substrate is not immersed into a reservoir. It is worth to be noted, that it is hard to control the homogeneity of the coating when using non-planar surfaces. The entire spraying process is very comlex and not well understood. Nevertheless, a careful adjustment and movement of the nozzle opens the possibility to coat reproducibly non-planar surfaces. Typical spray coatings were carried out with a perpendicular spray cone in respect to the surface. By lowering the spray angle it was shown that it is possible to obtain an orientation of anisotropic particles on the surface.[101–104] This approach is called grazing incidence spraying (GIS) and a typical setup is shown in Figure 3.3. Gas and liquid are dispersed by a nozzle and can be controlled by independent pump systems. By doing this, droplets with adjustable size and velocity move to the surface and form a thin film on the sample's surface.

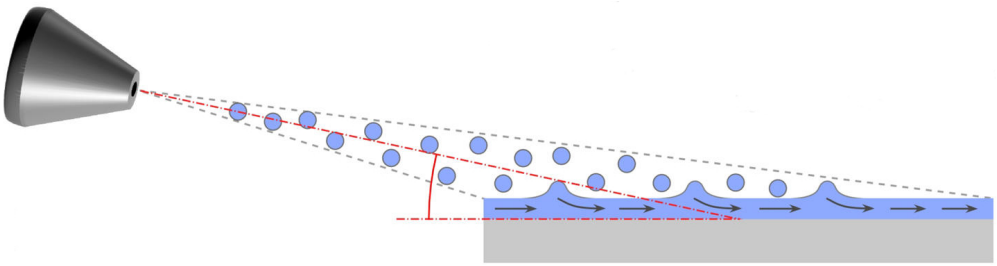

Figure 3.3: Scheme of grazing incident spraying. Adopted from Blell *et al.*[103]

In this work, GIS was used to align Halloysite nanotubes (HNTs). Therefore, HNTs were loaded with PSS to increase electrostatic repulsion between individual HNTs and to increase the affinity to a positively charged surface (see Section 3.2.6). The experiments were carried out at Institut Charles Sadron (Strasbourg, France). A homemade spraying setup, equipped with fluid nozzle (Schlick Mod. 970, Coburg, Germany), was placed 2 cm above and 5 mm apart from the sample. The angle of incidence was 10°. Spray deposition was carried out on silicon substrates (4 x 2 cm^2) spin coated with PEI. Concentration, spraying time, liquid flow rate, and gas flow rate were varied between $0.1 - 1.0$ g/L, $10 - 400$ s, $0.2 - 5$ mL/min, and $20 - 40$ L/min, respectively.

3.2.4 Brush Synthesis

Silicon substrates (1×3 cm^2) for were cleaned as described above. Subsequently, the surfaces were functionalized with a self-assembled monolayer of BTPAm initiator molecules as suggested by Laurent *et al.*[93] The BTPAm layer was stable under ambient conditions and was used to initiate the polymerization by atom-transfer radical polymerization (ATRP). For this purpose, 16 mL (80 $\%wt$, 68.1 mol) of METAC was diluted in 4.8 mL of water and 19.2 mL of methanol. After removing solved oxygen with a nitrogen stream for 15 min, 0.531 g (3.4 $mmol$) of bipyridine, 0.1386 g (1.4 $mmol$) of copper(I) chloride, and 0.0094 g (0.07 $mmol$) of copper(II) chloride were added. Subsequently, the solution was degassed for another 15 min and the wafers were left in this solution for 5 h. Termination was accomplished by exposing the solution to air. The wafers were sonicated four times in water for 5 min. To prepare polyelectrolyte brushes on the larger silicon substrates ($7 \times 3.5 \times 1$ cm^3) used for neutron reflectivity, the recipe was scaled up by a factor of 7.5.

3.2.5 Preparation of Brush/PEM Composite Systems

The PMETAC brushes, synthesized as mentioned above, were used as substrates for PEMs. Composites with PEMs of different layer numbers were prepared by using the layer-by-layer deposition method described in Section 3.2.1.

3.2.6 Halloysite Suspensions

Pristine HNTs were ground, solved in water and sonicated for 5 to 10 min. The pH value was checked with a pH meter inoLab pH 720 equipped with a WTW electrode SenTix 41 (Xylem Analytics, Weilheim, Germany, $pH \pm 0.01$). PSS loading was done according to Zhao *et al.*[80] Therefore, 4 g PSS were dissolved in 200 mL water and stirred for 30 min. Afterwards, 4 g HNTs were added in portions and the suspension was stirred for 48 h. The suspension was left standing for 1 h and the supernatant was centrifuged at 4300 rpm for 10 min. The obtained centrifuged sediment was washed with water and centrifuged for another four times. After freeze drying, around 0.5 g of a yellowish to reddish solid was obtained and ground to powder for further studies. Depending on the purpose, suspensions with different concentrations were prepared by mixing HNTs with water. The suspensions were sonicated for $5 - 10$ min.

3.3 Methods

3.3.1 Ellipsometry

Ellipsometry is a fast and non-destructive method to determine the thickness and the refractive index of thin films. It is based on the change in polarization of light. The electric field vector $\overrightarrow{E}$, which oscillates perpendicular to the direction of propagation, is a superposition of parallel and perpendicular vectors with respect to the plane of incidence and can be described as

$$\overrightarrow{E}(\overrightarrow{r},t) = \begin{pmatrix} |E_p| cos(2\pi\nu t - \overrightarrow{k} \cdot \overrightarrow{r} + \delta_p) \\ |E_s| cos(2\pi\nu t - \overrightarrow{k} \cdot \overrightarrow{r} + \delta_s) \end{pmatrix} \tag{3.1}$$

where $|E_p|$ and $|E_s|$ are the amplitudes, ν the frequency, $\overrightarrow{k}$ the wave vector with $|\overrightarrow{k}| = 2\pi/\lambda$ and δ_p and δ_s the phase shift. Since the wavelength λ is much longer than the film thickness, the time dependence can be neglected. Equation 3.1 simplifies to

$$\overrightarrow{E} = \begin{pmatrix} |E_p| e^{i\delta_p} \\ |E_s| e^{i\delta_s} \end{pmatrix}. \tag{3.2}$$

The difference in phase shifts between the parallel and the perpendicular vector of the electric field determines the polarization of light

$$|\delta_p - \delta_s| = \frac{i}{2} \cdot 180°;\ i \geq 0. \tag{3.3}$$

If i is an even or an odd integer, light is linear or circular (for equal amplitudes) polarized, respectively. For all other allowed numbers, the light results in elliptical polarization. As a result of the time independence, the change of the electric wave is only dependent on amplitudes and phase shift. One can define two ellipsometric angles Δ and ψ which combine the properties of the incoming and the reflected beam.

$$\Delta = (\delta_p^r - \delta_s^r) - (\delta_p^i - \delta_s^i) \tag{3.4}$$

$$\tan\psi = \frac{|E_p^r|/|E_p^i|}{|E_s^r|/|E_s^i|} \tag{3.5}$$

Additionally, the reflection properties can be described by two reflection coefficients r_p and r_s for the parallel and perpendicular light.

$$r_p = \frac{|E_p^r|}{|E_p^i|} e^{i(\delta_p^r - \delta_s^r)} \tag{3.6}$$

$$r_s = \frac{|E_s^r|}{|E_s^i|} e^{i(\delta_s^r - \delta_p^r)} \tag{3.7}$$

The relation of these reflection coefficients is connected with the ellipsometric angles.

$$\tan\psi \cdot e^{i\Delta} = \frac{r_p}{r_s} \tag{3.8}$$

The parameter Δ and ψ can be measured directly with an ellipsometer. Unfortunately, they are not independent from each other. Hence, a model is required to extract the optical properties. The setup of the used null-ellipsometer (Optrel, Sinzing, Germany) is shown in Figure 3.4.

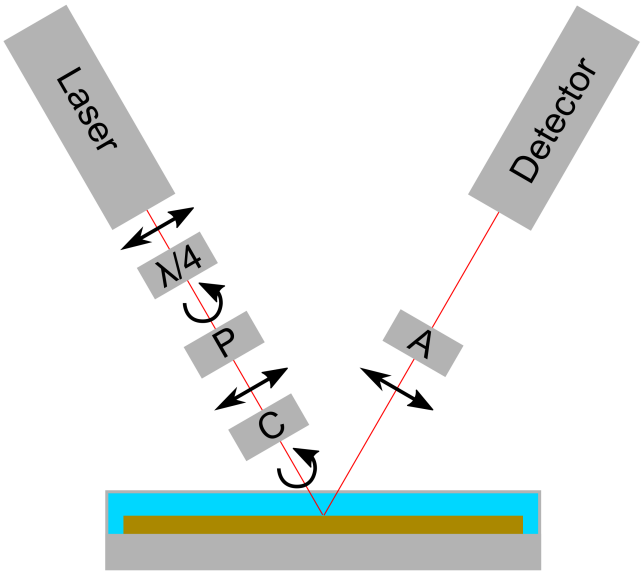

Figure 3.4: Schematic setup of a PCSA (polarizer-compensator-sample-analyzer) Null-ellipsometer. Arrows indicates the polarization of light.

A monochromatic, linear polarized laser beam is transformed into circular polarized light with a quarter wave plate to avoid angle dependent intensity. A polarizer and a compensator (a second quarter wave plate) generated elliptic, or in special cases circular or linear polarized light before it is reflected from the sample. The reflected beam passes the analyzer, which turns to get a minimum of intensity on the detector. The angle of incidence with respect to the surface normal is chosen near the Brewster angle of the substrate, in order to get a high difference between the two reflection coefficients. Consequently, measurements were carried out at an angle of incidence of 70° in respect to the surface normal against air. The ellipsometer was equipped with a home-built humidity cell to measure at controlled relative humidity h. The relative humidity was adjusted by mixing a dry and a water-saturated nitrogen stream. The lowest humidity ($1 \pm 1\%$ RH) was reached by using just a pure nitrogen stream. Prior to the measurements, every sample was equilibrated under the respective humidity at least 20 min. The accuracy of the

humidity sensor (Testo 6614 sensor, Testo 6681 humidity measuring transducer, Testo Ag, Leinkirch, Germany) was ±1% RH. The data were fitted with Elli v3.1. (Optrel, Sinzing, Germany) based on a two-layer model as shown in Table 3.1.

Table 3.1: Layer model for fitting a polymer film on silicon wafer against air. Parameters are refractive index n, absorption coefficient k and thickness d. Empty arrays imply bulk properties with an infinite thickness and the term "fit" marks the respective fitting parameters.

	layer	n	k	d [nm]
Continuum	air	1	0	
1. layer	Polymer	fit	0	fit
2. layer	SiO_x	1.4598	0	1.1
Continuum	Si	3.8858	-0.0200	

Except for the silicon oxide thickness, which was taken from the XRR data, all fixed parameters were adopted from Dodoo *et al.*[53] Thickness and refractive index were fitted simultaneously for PEMs thicker than 10 nm. The refractive index for PEMs thinner than 10 nm was fixed to the average value of the fitted ones. The fitting procedure was started with refractive index of 1.466 and thicknesses between 5 and 60 nm depending on the layer number. Composites of PEMs and brushes were fitted with the same layer model starting thicknesses as obtained by XRR.

3.3.2 X-Ray and Neutron Reflectometry

Thin films with a thickness lower than 100 nm can be characterized with the help of X-Ray or Neutron reflectivity measurements.[109] Reflectometry is a well-established technique to resolve the internal composition of thin films along the z-axis perpendicular to a flat surface. If the frequency of the incoming electromagnetic wave is smaller than the resonance frequency of the scattering medium the refractive index n can be described by

$$n = 1 - \delta + i\beta \tag{3.9}$$

where δ and β are the dispersion and absorption term, respectively. The dispersion term is described by

$$\delta = \frac{\lambda^2}{2\pi} \cdot \rho_{X,N} \tag{3.10}$$

where $\rho_{X,N}$ is the scattering length density for X-Rays or neutrons and λ the wavelength of the respective beam. For soft matter, the value of the dispersion term δ is in the order of 10^{-6} and the value of the absorption term β in the order of 10^{-12}. Thus, the latter is negligible. Above a critical angle α_c, the wave is split into a reflected wave

$\vec{k}_f$ and a transmitted wave $\vec{k}_t$. The critical angle is specific for each material and is defined as

$$\alpha_c \approx \sqrt{2\delta} = \lambda\sqrt{\frac{\rho_{X,N}}{\pi}}. \tag{3.11}$$

In general, the refractive index is smaller than unity and the critical angle is usually some tenths of a degree. Negative SLDs which can be obtained for neutrons lead to an absence of a critical angle. Below the critical angle, total external reflection occurs. The electromagnetic wave can be described by the wave vector $\vec{k}$. The magnitude is defined as

$$|\vec{k}| = k = \frac{2\pi}{\lambda}. \tag{3.12}$$

The interaction between an incident electromagnetic wave $\vec{k}_i$ and an interface between air and matter is shown in Figure 3.5.

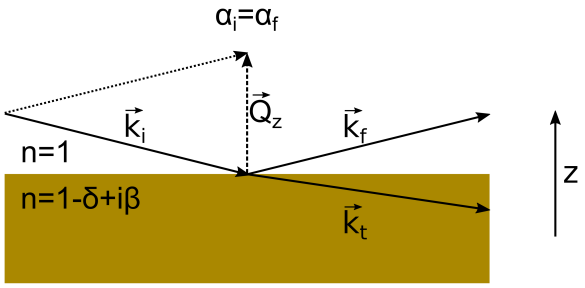

Figure 3.5: An incoming plane wave $\vec{k}_i$ is split at a surface into a reflected wave $\vec{k}_f$ and a transmitted wave $\vec{k}_t$ if the incident angle α_i is above the critical angle α_c. Otherwise a transmitted wave is not observed and total external reflection occurs.

The reflection coefficient r_f and the transmission coefficient t_f are described by the Fresnel formulas.

$$r_f = \frac{k_i - k_t}{k_i + k_t} \tag{3.13}$$

$$t_f = \frac{2k_i}{k_i + k_t} \tag{3.14}$$

The resulting reflected intensity R and transmitted intensity T are

$$R = |r_f|^2 \tag{3.15}$$

and

$$T = |t_f|^2. \tag{3.16}$$

Based on these equations, the interaction of $\overrightarrow{k}_f$ with multiple, stacked interfaces is described by the recursive Parratt algorithm.[110] Taking into account that the substrate has an infinite thickness and thus no reflection from its backside, the reflectivity at the bottom surface of the substrate is zero. Furthermore, the transmission coefficient is expressed by $t_{j+1,j} = 1+r_{j+1,j}$. Surface roughness for each interface is taken into account by an exponential dumping factor with the roughness σ_j. With that, the recursive formulas end up in

$$r_{j,j+1} = \frac{k_{z,j} - k_{z,j+1}}{k_{z,j} + k_{z,j+1}} exp(-2k_{z,j}^2\sigma_j^2) \tag{3.17}$$

and

$$t_{j+1,j} = 1 + r_{j+1,j} exp\left\{-(k_{z,j} - k_{z,j+1})^2\sigma_j^2/2\right\}. \tag{3.18}$$

The ratio X_j between reflected and transmitted intensity is expressed by

$$X_j = \frac{R_j}{T_j} = exp(-2ik_{z,j}z_j)\frac{r_{j,j+1} + X_{j+1}exp(2ik_{z,j+1}z_j)}{1 + r_{j,j+1}X_{j+1}exp(2ik_{z,j+1}z_j)}. \tag{3.19}$$

Finally, the overall reflected intensity is

$$R = |X_1|^2 = |R_1|^2. \tag{3.20}$$

The thickness d of a layer is defined by the distance between two interfaces

$$d = z_{j-1} - z_j. \tag{3.21}$$

According to Bragg's law, constructive interference occurs if the path way of the wave $2d\sin\alpha$ is a multiple of its wavelength λ

$$2d\sin\alpha = n\lambda. \tag{3.22}$$

Therefore, maxima, so called Kiessig fringes, occur if

$$d = \frac{n\lambda}{2\sin\alpha}. \tag{3.23}$$

Independent of the measurement principle (either constant wave length or constant angle), the momentum transfer Q_z (shown in Figure 3.5) perpendicular to the surface in specular reflection conditions is defined as

$$Q_z = k_f - k_i = \frac{4\pi}{\lambda}\sin\alpha_i \tag{3.24}$$

and the thickness in term of Q_z is

$$d = \frac{2\pi}{\Delta Q_z} \tag{3.25}$$

The difference of X-Rays and Neutrons will be discussed in the following paragraphs.

X-Ray reflectometry (XRR)

X-Ray radiation is scattered at electrons. The atomic scattering factor can be approximated by $f_i \approx Z_i$ for glancing incident angle. With that, the X-Ray scattering length density ρ_X of a volume V scales with atomic number Z_i by

$$\rho_X = \frac{1}{V} \sum_{i=1}^{n} Z_i r_e. \tag{3.26}$$

An insight into the internal composition of soft matter, which consists mainly of hydrogen and carbon, is hard to reach because the scattering contrasts between the different molecules are very low. Therefore, the overall thickness can be precisely determined but the different components cannot be resolved.

In this thesis, all measurements were carried out with the X-ray reflectometer D8 Discover (Bruker, Karlsruhe, Germany). The beam consists of $K\alpha$ radiation from a copper anode ($\lambda = 1.54$ Å). The scan range varies from $2\Theta = 0° - 5°$ with a step width of 0.01°. The resolution was $\Delta Q_z = 2.46 \cdot 10^{-3}$ Å^{-1}. The data were footprint corrected,[111] normalized to the intensity I_0, and fitted with Parratt32 v1.6. from HZB Berlin-Wannsee,[112] on the basis of a model of two independent layers as shown in Table 3.2. Fixed values were adopted from Voets *et al.*[111]

Table 3.2: Layer model for X-ray reflectometry. Parameters are thickness d, scattering length density ρ_X, the respective imaginary part $Im(\rho_X)$ and the roughness σ of the interface above the respective layer. Empty arrays imply bulk properties with an infinity thickness and "fit" arrays are the fitting parameters.

	layer	d [nm]	ρ_X [Å^{-2}]	Im(ρ_s) [Å^{-2}]	σ [nm]
Continuum	air		0	0	0
1. layer	Polymer	fit	fit	$6.451 \cdot 10^{-8}$	fit
2. layer	SiO_x	fit	$1.891 \cdot 10^{-5}$	$2.445 \cdot 10^{-7}$	fit
Continuum	Si		$2.015 \cdot 10^{-5}$	$4.588 \cdot 10^{-7}$	0

In Chapter 4 PEMs were characterized by X-ray reflectometry to verify thicknesses obtained by ellipsometry under dry conditions. A home-built cell was filled with a drying agent (silicon gel) to obtain relative humidity around 1% RH. The humidity was measured with a HygroPalm - HP23-A (Rotronic, Switzerland, sensor HC2-P05, ±1.5% RH). The samples were equilibrated in the closed cell for at least 60 min.

Neutron Reflectometry (NR)

In contrast to X-Rays, neutrons interact with the nucleus of an atom and therefore it is possible to generate a contrast between different compounds without changing their chemical behavior. This allows to generate contrasts between different isotopes. The scattering length density (SLD) ρ_N does not follow a systematic order and can have

positive as well as negative values. The SLD ρ_N is the sum of the coherent scattering length b_c of all atom in the respective volume V.

$$\rho_N = \frac{1}{V}\sum_{i=1}^{n} b_{c,i} \tag{3.27}$$

For soft matter, an exchange of hydrogen (e.g. for water $\rho_{H2O} = -0.559 \cdot 10^{-6}\text{Å}^{-2}$) and deuterium (e.g. for deuterated water $\rho_{D2O} = 6.36 \cdot 10^{-6}\text{Å}^{-2}$) gives insight into the internal composition. Furthermore, different mixing ratios of the solvent can highlight or suppress various compounds.

Chapter 5 deals with the internal structure of brush-PEM composites and is based NR. Therefore, a bare PMETAC brush and brush/PEM composites were studied. Experiments were carried out at the Heinz-Maier-Leibnitz center (FRM II, Garching, Germany). The setup of the instrument $NREX^+$ is shown in Figure 3.6. A monochromatic beam ($\lambda = 4.28$ Å) was reflected at the sample and collected under various angle with a 2α geometry by a ^3He detector. The sample environment was a closed humidity chamber where the relative humidity was adjusted by mixing a dry nitrogen stream with a water saturated nitrogen steam by an electronic device. The humidity was measured by HygroPalm - HP23-A (Rotronic, Switzerland, sensor HC2-P05, ±1.5% RH). The samples were equilibrated at least 30 min before each measurement.

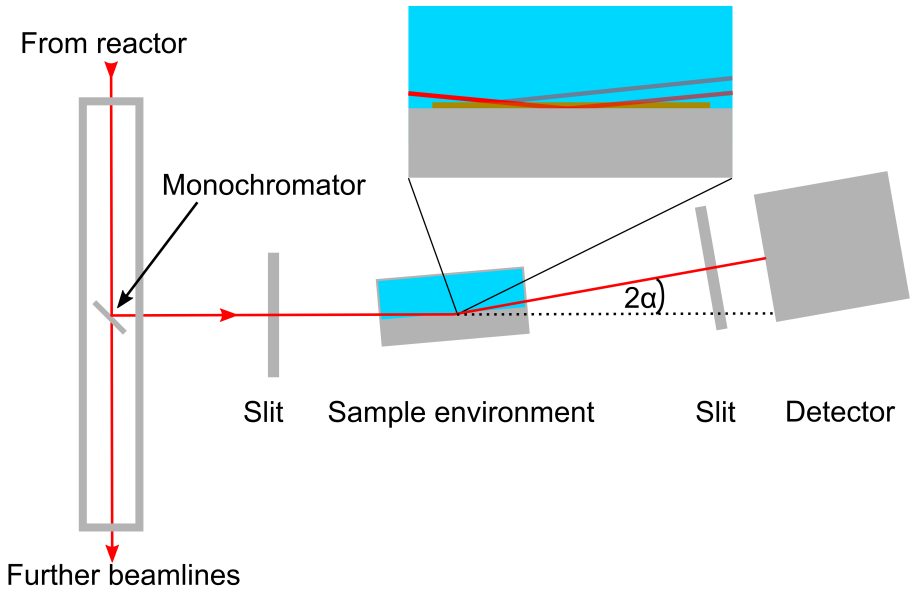

Figure 3.6: Scheme of $NREX^+$ reflectometer. Magnification of the beam-sample interaction shows the reflections at different interfaces. Maxima in intensity are obtained according to Bragg's law.

Data analysis was done with a self-consistent fitting procedure based on fitting procedure developed by Emanuel Schneck and co-workers.[113–115] Based on volume fraction ϕ_i of each compound i the SLD profiles $\rho_i(z,h)$ was defined as

$$\rho(z,h) = \sum_i \phi_i(z,h) \cdot \rho_i. \tag{3.28}$$

In the following, the volume fraction profiles will be explained for the different compounds. The volume fraction of the PMETAC brush ϕ_{PMETAC} was described by a stretched exponential function multiplied by a factor $f_{SiO_2}(z)$ which truncated the profile at the substrate interface.

$$\phi_{PMETAC}(z,h) = f_{SiO_2}(z) \cdot exp\left(-\frac{z}{\tau(h)}\right)^{n(h)} \tag{3.29}$$

The decay length τ and the exponent $n(h)$ allowed a wide range of possible shapes. Both were defined by polynomials, e.g. τ was

$$\tau(h) = \tau_0 \ + A_\tau \cdot h \ + B_\tau \cdot h^2 \ + C_\tau \cdot h^3 \tag{3.30}$$

where τ_0, A_τ, B_τ and C_τ were adjustable parameters during the fitting procedure. For $n(h)$, a second order polynomial was found to be sufficient. The factor $f_{SiO_2}(z)$ described the internal roughness and was expressed by an error function with the roughness σ_{SiO_2}.

$$f_{SiO_2}(z) = 0.5\left(1.0 + Erf\left(\frac{z}{\sqrt{2 \cdot \sigma_{SiO_2}}}\right)\right) \tag{3.31}$$

The amount of polymer per unit area was defined in terms of the equivalent thickness D_{PMETAC}.

$$D_{PMETAC} = \int_{-\infty}^{\infty} \phi_{PMETAC}(z)\ dz \tag{3.32}$$

For a given set of $\tau(h)$ and $n(h)$, the maximal brush volume fraction $\phi^0_{PMETAC}(h)$ was not a free parameter but resulted from the normalization condition according to Equation 3.32. For very low humidities, the volume fraction of air $\phi_{air}(z,h)$ inside the polymer matrix was just the difference from unity calculated by

$$\phi_{air}(z,h) = 1 - \phi_{PMETAC}(z,h), \text{ for } \ h \ < 6\ \%RH. \tag{3.33}$$

For sufficiently high humidities, the polymer brush was assumed to have a constant water fraction for each relative humidity such that

$$\phi_{H_2O}(z,h) = \phi_{PMETAC}(z,h) \cdot (1 - \phi^0_{PMETAC}(h)). \tag{3.34}$$

This definition assured full condensation ($\phi_{PMETAC} + \phi_{H_2O} = 1$) in the plateau region. Furthermore, it was not necessary to account for scenarios in which the brush exceeds the outer surface of the PEM layer. The polyelectrolyte brush formed a compact layer

without PEM, and it did not reach a fully stretched conformation in the absence of PEM. Therefore, the brush profile was truncated at the PEM outer interface by multiplication by a factor $(1 - f_{out}(z,h))$ which is specified further below.

The PEM was found to be a rather compact layer on top of the brush. The alternating adsorption of deuterated and hydrogenated polyelectrolytes leads to a layer with a uniform SLD.[47] Bragg peaks associated with significant SLD oscillations were not observed due to layer intermixing.[33,28] The effective SLD, ρ_{PEM}, was an adjustable fitting parameter. Accordingly, the PEM volume fraction profile $\phi_{PEM}(z,h)$ was expressed in terms of a single rough slab of humidity-dependent center position $z_{PEM}(h)$, thickness $d_{PEM}(h)$, and maximal volume fraction $\phi^0_{PEM}(h) = D_{PEM}/d_{PEM}(h)$. The entire PEM profile was described by

$$\phi_{PEM}(z,h) = f_{SiO_2}(z) \cdot f_{in}(z,h) \cdot \phi^0_{PEM}(h) \cdot (1 - f_{out}(z,h)) \tag{3.35}$$

where the factors $f_{out}(z,h)$ and $f_{in}(z,h)$ truncated the profile at the outer and inner surfaces of the PEM layer in the form of error functions with roughness parameters $\sigma_{in}(h)$ and $\sigma_{out}(h)$. These two roughnesses depended on the humidity according to second-order polynomials. At the SiO_2 surface, the slab was truncated by the error function $f_{SiO_2}(z)$ to prevent the unphysical penetration of PEM into the oxide. For the humidity dependence of z_{PEM} and d_{PEM}, second-order and third-order polynomials were invoked, respectively (compare with Equation 3.30). Finally, all of the remaining volume that was not occupied by the other chemical components was assumed to be filled with air for $h < 6\%\ RH$, or with water for $h > 30\%\ RH$ (according to Equation 3.33 and 3.34).

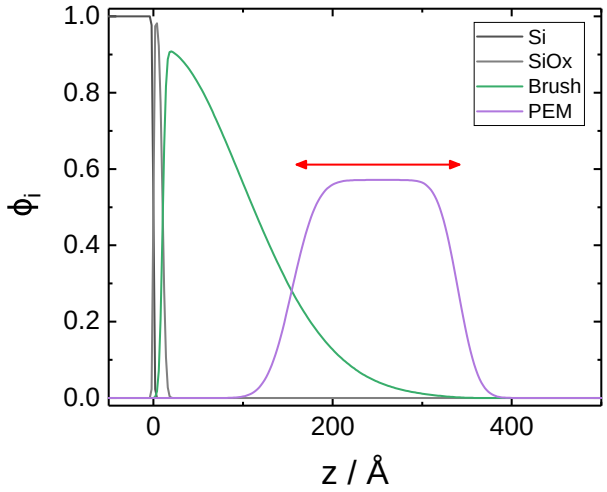

Figure 3.7: Exemplary volume fraction profile. The shape of both profiles and the position of the PEM (marked with red arrow) are varied during the fitting procedure. The difference to unity is either filled by air or water (not shown).

These descriptions ended up in a volume fraction profile for the composites as shown in Figure 3.7. The shape of the brush and PEM profile were variable during the fitting procedure as described above. Furthermore, the position of the PEM was variable to fit the model to the measured data. The simultaneous fits of the reflectivity curves at different relative humidities comprised six humidity conditions for the bare brush and nine humidity conditions for the brush/PEM composite systems. To find the best-matching model parameters, sets of initial parameters were chosen to calculate the corresponding interfacial SLD profiles $\rho(z,h)$ for each humidity. The resulting $\rho(z,h)$ profiles were then discretized into hundreds of thin slabs of 0.2 nm thickness and constant SLD. The corresponding reflectivity curves were then calculated using dynamical reflection theory via application of Fresnel's reflection laws at each slab/slab interface and the subsequent phase-corrected summation using the iterative procedure of Parratt.[110] To account for the finite experimental Q_z resolution, all of the theoretical reflectivity curves calculated for the case of infinite resolution were convoluted with Gaussian functions representing the experimental resolution. In the last step, the parameters were varied until the best simultaneous agreement with all experimental reflectivity curves, characterized by the minimum χ^2 deviation, was reached.

3.3.3 Atomic Force Microscopy

Atomic force microscopy (AFM) is based on the interactions between a nanometer sized tip at the end of a bendable cantilever and the investigated sample. The interaction potential as a function of the tip-sample distance r is described by the Lennard-Jones potential V_{LJ}

$$V_{LJ} = 4\epsilon_{min}\left\{\left(\frac{r_0}{r}\right)^{12} - \left(\frac{r_0}{r}\right)^{6}\right\} \tag{3.36}$$

where ϵ_{min} is the potential minimum, r_0 the distance with zero potential. In principal, the sample can be scanned or indented by the tip.

To scan the sample's surface, tapping mode (marked in Figure 3.8) can be used. It works between repulsive and attractive potential. This ensures less damage than contact mode but higher sensitivity than non-contact mode.[116] Using tapping mode, the cantilever is exited to its resonance frequency. The strength of interaction is then controlled by damping of the free amplitude. Therefore, it is also called amplitude modulation AFM (AM-AFM). A scheme of an atomic force microscope is shown in Figure 3.9.

A feedback loop readjusts the tip-sample distance to maintain a constant interaction strength and therefore a constant damped amplitude. Scanning the sample in x-y direction while mapping the tip-sample distance generates a topographical image. The bending of the cantilever is detected by the displacement of a laser beam which is reflected from the backside of the cantilever. The sample roughness was determined by the root mean square deviation of the height σ.

$$\sigma = \sqrt{\frac{1}{m}\sum^{m}(z_i - \bar{z})^2} \tag{3.37}$$

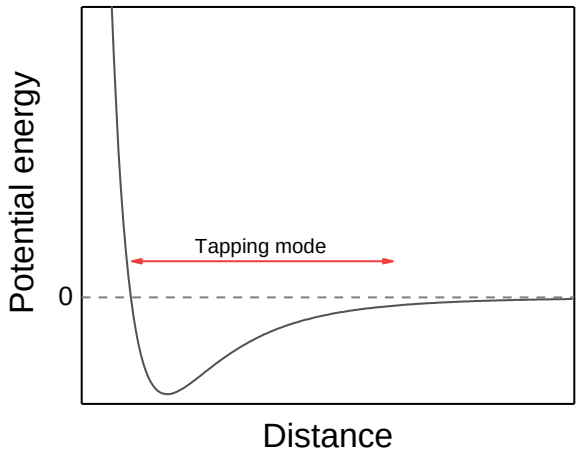

Figure 3.8: Scheme of the Lennard-Jones potential. Range used in tapping mode is marked in red.

In this work, scanning mode was carried out to obtain a real image of the samples' surface topography. Therefore, measurements were carried out either with a Cypher AFM or with a MFP3D from Asylum Research (Oxford Instruments Asylum Research Inc., Santa Barbara, CA, USA) in AC air topography mode. Silicon cantilevers AC160TS-R3 (Olympus, Tokyo, Japan) or FS-1500AuD (Asylum Research) with a spring constant of roughly 20 N/m were used.

Nematic ordner parameters, calculated in Chapter 6, were obtained by using the OrientationJ plug-in for ImageJ.[117,118] Image modification was based on a procedure reported by Probst *et al.*[104] Therefore, AFM images were cutted to get rid of the scale bar and margins. A threshold was set by the method of Yen.[119] Impurities with a circularity between 0.7 and 1 were filtered out. Images of HNTs bilayers were not corrected because it was not possible to distinguish between background, impurities and HNTs. The orientation was calculated with a Gaussian window of 15 *pixel* (roughly referring the diameter of HNTs) and a minimal coherency of 5 %. The nematic ordner parameter was calculated in respect to the mean orientation obtained by a Gaussian fit.

3.3.4 Electrophoretic Mobility

Charged particles and macromolecules dispersed in a solvent move in response of an electric field. If the particle size, field strength, and viscosity are constant, the drift speed only depends on the charge of the respective object. Therefore, it was possible to study the surface modification of HNTs. Pristine and modified HNTs were dispersed in water ($c = 0.1\ mg/ml$) according to Section 3.2.6 and movement of the particles was monitored

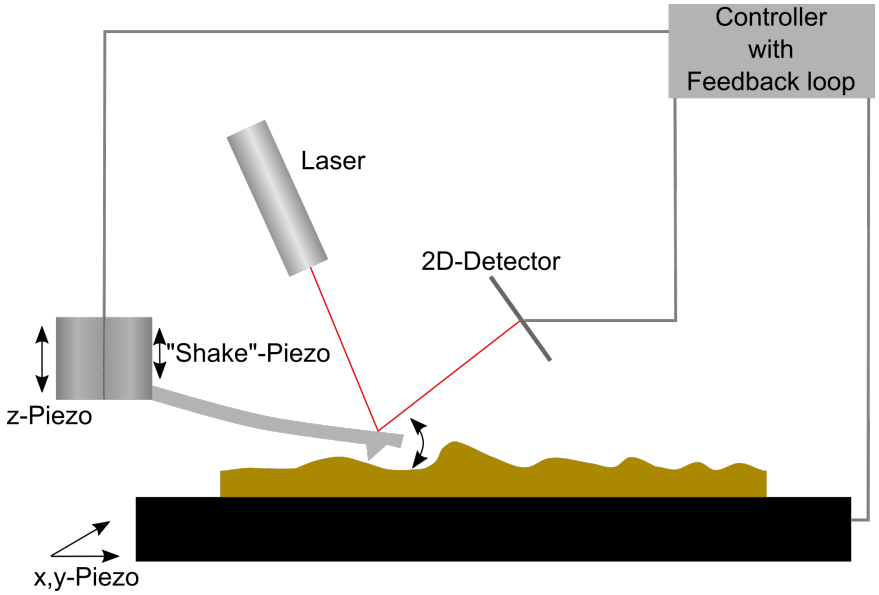

Figure 3.9: AM-AFM scheme. The "shake"-piezo actuator excites the cantilever to its resonance frequency. The amplitude is traced by a 2D-detector. The z-piezo actuator regulates the height of the cantilever to maintain a constant amplitude. The sample is scanned by moving the x,y-piezo actuator.

in an alternating electric field measured with the Malvern Nano-ZS ($\lambda = 433\ nm, 4\ mW$, Malvern, UK) at an angle of 173° (back scattering).

3.3.5 Polarization Microscopy

Polarization microscopy is suitable to investigate anisotropy of coatings. Therefore, linear polarized light interacts the sample. Changing the angle between polarizer and the mean orientation direction leads to a change of intensity. Here, polarization microscopy was used to investigate the orientation of HNTs over a larger area than it is possible with AFM measurements. Figure 3.10 shows the basic principle. For sake of simplicity, the scheme is drawn in transmission setup, although the microscope worked in reflection mode.

Experiments were carried out with polarization microscope Axiophot (Zeiss, Germany) equipped with Axiocam 305 color and different Epiplan Neofluor lenses (20x, 50x, and 100x magnification, Zeiss, Germany). The considered area had a minimum diameter of 150 μm. Polarizer and analyzer were set to 90° and the sample was orientated with respect to the polarizer. Every 15° an image was taken between 0° and 90°. These images were analyzed by calculating the gray value of each image with ImageJ.[102,118]

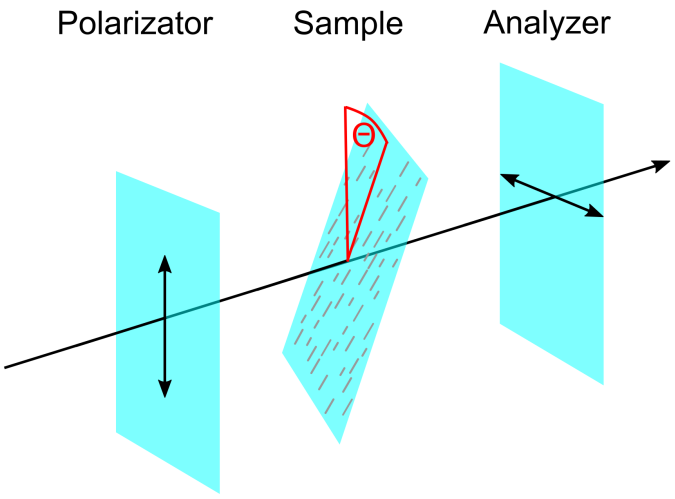

Figure 3.10: Setup of polarization microscopy in crossed-polarizer configuration.

3.3.6 Transmission Electron Microscopy

Experiments were carried out by my colleagues Maren Lehmann and Marcus Witt.

Transmission electron microscopy (TEM) is based on the interaction of an electron beam with the sample. Therefore, an electron beam focused by electromagnetic lenses is absorbed by the sample depending on its chemical composition. Transmitted electrones are detected to obtain an image of the sample. In this work, HNTs were characterized either with a Cryogen TEM JEOL JEM2100 (JEOL, Tokyo, Japan) or a TEM FEI CM20 microscope (FEI, Eindhoven, The Netherlands) equipped with a LaB_6 cathode. The acceleration voltage was 200 kV. The samples were prepared on a copper grid covered with a carbon film (200 mesh or 300 mesh, Science Service, Munich, Germany).

4 Polyelectrolyte Multilayers: Water Uptake and Water Condensation in Voids

Similar content is published in "Water uptake of polyelectrolyte multilayers including water condensation in voids" Oliver Löhmann, Maximilian Zerball and Regine von Klitzing, *Langmuir* (2018), 34 (38), 11518 - 11525 `http://dx.doi.org/10.1021/acs.langmuir.8b02258`

Abstract

The chapter addresses the swelling of PEMs at varying humidity. In particular, a new model will be presented, which takes the gradual filling of voids into account. Absorption of water results in PEM swelling. This absorbed water can be distinguished into swelling and void water. Swelling water leads to an increase in thickness and a change of the optical properties of PEMs, while the void water results only in a change of the optical properties. In former studies, neutron reflectometry was used to distinguish between swelling and void water. However, as we show in this study, it is possible to resolve the two different kinds of water in PEMs by ellipsometry, a much simpler tool. The present study evaluates and interprets the refractive index of PSS/PDADMAC PEMs. Both the swelling behavior and the refractive index change as a function of relative humidity h and were found to be independent of the layer number. The *void model* and the *extended void model* were used to describe the data. The *void model* model allows fitting the experimentally determined refractive index at h beyond 20% RH but fails for h lower than 20% RH. Therefore, we modified the existing model in order to account for air-water exchange.

The *extended void model* assumes a gradual air-water exchange at low h and describes the refractive index over the entire humidity range in a precise way. Up to 30% RH air and water coexist. Above this threshold, the voids are completely filled with water and this threshold does not change neither with layer number nor with the outermost layer. Furthermore, this model allows the determination of the volume fraction of the voids (0.05 ± 0.01) and the refractive index of the pure polymer matter (1.592 ± 0.002).

4.1 Introduction

Polymer coatings can change the morphology and the functionality of surfaces. PEMs are an easy approach to coat charged surfaces independently of their geometrical appearance

and for tuning the functionality.[2,120] Functional surfaces are used to prevent or to favor adsorption of specific target molecules.[121,122] The response of the functionalized surfaces to variations in environment is essential for technical applications.[42] Especially for medical application, it is of crucial importance to control the interaction between drugs and living organisms.[43,44] Here, PEMs can be used as mediators to avoid side effects. The functionality of PEMs is dominated by their chemical composition. Their response to environmental changes leads to a change in the polymer conformation within the PEMs and thus to a change in chemical and physical properties.[123,124]

PEMs are fabricated by consecutive adsorption of oppositely charged PEs. This method is called the layer-by-layer technique and is an easy, well-known, and powerful tool to build up and tailor PEMs.[1,2] The thickness increment per deposited layer depends on the conditions during the dipping procedure.[15,125–127] Typical conditions, which are adjusted during layer deposition, are type and concentration of polyions, concentration and type of added salt, pH, and the dipping time. All of them influence the constitution of PEMs. Here, strong polyelectrolytes like PSS and PDADMAC dissolved in a 0.1 M sodium chloride solution are used to avoid a pH dependence and ensure a sufficient polyelectrolyte mobility.[28] The growing behavior of PSS/PDADMAC PEM is well-investigated and discussed in several papers.[32,40,128–130]

Planar adsorbed PSS/PDADMAC PEMs are responsive to ionic strength and water content in the environment but not very much to thermal treatment.[34,37] In contrast, hollow PSS/PDADMAC PEM capsules respond strongly to thermal treatment.[131–133] PEMs act like a sponge and absorb water reversibly. During immersing PEMs in water, they swell, which leads to a decrease in their polymer network density. As a result of that, the possibility to take up target molecules is much higher than in the dry state. This process is reversible, and therefore, it is possible to incorporate target molecules by drying the PEM films, and subsequently to release them under controlled conditions.[134,135] Thus, PEMs can be used as carrier systems for specific target molecules, e.g., drugs or anticorrosive coatings.

Mainly, PEMs were examined in dry (about 1% RH), ambient (about 30% RH), and water saturated (about 98% RH) air and in water.[32,40,49] Water uptake and distribution within PEMs immersed in H_2O or D_2O were investigated by neutron reflectivity.[40,47] It was shown that the total water content is the sum of two different types of water in a PEM: void and swelling water. The void water fills the voids between the polyelectrolyte chains which exist also in vacuum. This amount of water changes the scattering length density but does not lead to a swelling of the PEMs. The swelling water leads to a swelling of the PEM. The amount of swelling water increases by increasing the ionic strength and increasing size of anions during preparation.[53] The amount of void water shows the opposite effect. Combining ellipsometry and quartz crystal microbalance with dissipation can also give information about the swelling behavior in a liquid environment. The swelling that occurs in salt solutions with different concentrations is fully reversible by changing the salt concentration.[55] The water content for PSS/PDADMAC can reach a maximum of up to 70 % in a 0.5 M NaCl solution.

Although there are already several papers on the void model and the swelling behavior of PEMs, the mechanisms of void water uptake remain unclear and need further inves-

tigation.[32,49] Ellipsometry is suitable to study PEMs in humid conditions. This fast, nondestructive method gives information about thickness and refractive index. Zerball *et al.* showed that this method is also suitable to distinguish between swelling and void water.[49] Nevertheless, the swelling behavior over the entire humidity range from a dry environment to a water saturated environment is not fully described. In this chapter, ellipsometry data are evaluated to obtain information about the thickness and the optical properties of PSS/PDADMAC PEMs as a function of relative humidity h in 10% RH steps. This shows that the swelling ratio with respect to the dry state and the decrease of the refractive index is independent of the number of deposited layers. The refractive index can be described by different models. Here, it is shown that the void model[47,49] cannot describe precisely the trend of refractive index over the entire humidity range. Therefore, the void model is extended. The results show that this model is well suitable over the entire humidity range to evaluate the measured refractive indices. Furthermore, the void fraction and the refractive index of the pure polymer matrix without voids can be calculated.

4.2 Results

4.2.1 PEM Thickness and Refractive Index

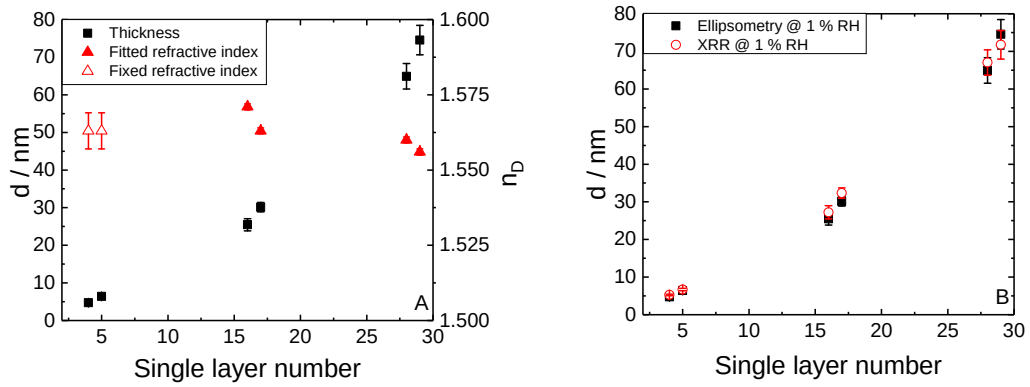

Figure 4.1: (A) Thickness (squares) and refractive index (triangles) of PSS/PDADMAC PEM as a function of single layer number at (1±1)% RH. Closed symbols correspond to fitted refractive index and open ones correspond to fixed refractive index as an average of the fitted values. (B) Comparison between ellipsometry (closed squares) and XRR (open circles) measured at $(1 \pm 1)\%$ RH. For some data points the error bars are not visible, since they are smaller than the symbols.

Figure 4.1A shows the thickness and the refractive index of PSS/PDADMAC PEMs with dependence on the number of deposited layers at 1% RH measured by ellipsometry.

The thickness increases in a nonlinear trend for low layer numbers which is in good agreement with earlier published results.[32,136] The refractive index is fitted for PEMs of 16, 17, 28, and 29 single layers and is independent of the layer number. For PEMs with 4 and 5 single layers, only one parameter (thickness) can be fitted because the change of the ellipsometric angle ψ is too small. Therefore, the refractive index is fixed and corresponds to the average of the fitted values for higher layer numbers.

Figure 4.1B shows the comparison of ellipsometry and XRR data to validate the model for analyzing ellipsometry data. All PEMs were measured at 1% RH, and their thicknesses were reproduced with XRR (reflectivity data and the best fits are shown in the Appendix). This indicates that the fixed refractive index for thin PEMs is suitable for ellipsometry data. The data lead to the conclusion that the refractive index of the dry PEM is around 1.56 which is in good agreement with literature.[49]

4.2.2 Swelling Behavior

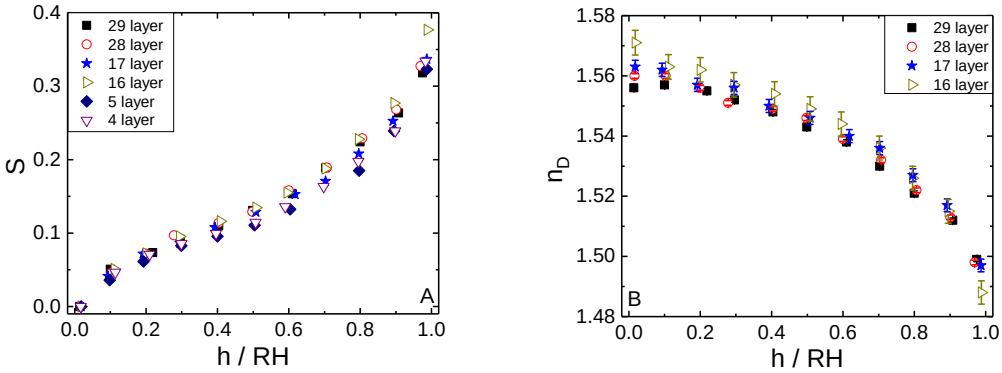

Figure 4.2: (A) Swelling coefficient S of PSS/PDADMAC PEMs as a function of h and layer number. (B) Refractive index n_D as a function of h and layer number.

The increase of h induces multilayer swelling due to water uptake from the surrounding environment. The volume fraction of water, which leads to a swelling, is defined by the swelling coefficient S:

$$S = \frac{d(h) - d_{dry}}{d(h)}. \tag{4.1}$$

S is described by the thickness of the dry PEM d_{dry} and the thickness of the swollen PEM $d(h)$. Figure 4.2A shows that PSS/PDADMAC PEMs do not swell in a linear behavior. Three regimes can be identified: Strong swelling is observed, in the first regime, between 1 and 40% RH. In the second regime, between 40 and 60% RH, flattening of the swelling coefficient is observed. The strongest increment of S is observed in the third

regime above 60% RH. Concurrently, the refractive index decreases, as shown in Figure 4.2B, due to the presence of more water (n=1.33) in the PSS/PDADMAC PEM ($n > 1.5$). Parts A and B of Figures 4.2 show that PEMs swell in the same way independent of the layer number. The error for the swelling coefficient fluctuates around ± 0.1. The error for the refractive index fluctuates around ± 0.002. Zerball *et al.* reported a detailed error analysis.[49]

4.2.3 Theoretical Description

On the basis of the effective medium theory, J. C. Maxwell Garnett reported a correlation between the optical properties and the volume fraction in metal glasses and metallic films.[50,51] Later on it was shown that this can also be adopted to PEM-water systems.[37,137] The Garnett model assumes a two-compound system in humid air (polymer + water) and a compact polymer film in dry conditions, i.e., 100 % polymer without any voids (calculations are shown in the Appendix). The exchange between air and water during the swelling is not considered by this model which causes the overestimation of the decrease of the refractive index at low humidity.[47] Therefore, another approach is made to describe the refractive index during changing h.

Void Model

The void model takes into account that air is replaced by water during swelling.[40,47] Two different kinds of water can be obtained: swelling and void water. Swelling water leads to a swelling of the entire PEM. Concurrently, swelling leads to a change of the optical properties. Void water is absorbed in the holes (voids) of the PEM matrix which occur during the preparation. This leads to a change of optical properties but does not affect the thickness. Neutron reflectivity was used to distinguish between swelling and void water in former studies.[40,47] On the basis of the calculations of the different amounts of water, due to the change in thickness and scattering length density, the void fraction was calculated. In the present chapter, the scattering length density is replaced by the permittivity. PEMs can be described by the permittivity ϵ, which is directly correlated to the refractive index for transparent and nonmagnetic materials by $\epsilon = n_D^2$. The effective medium theory leads to a complex term for a three-component system; therefore, the calculation are based on a linear combination. Here, two assumptions have to be taken into account for the void model.

First, the permittivity of a dry PEM (ϵ_{dry}) can be described by the permittivity of the pure polymers (ϵ_{poly}) and the fraction of voids $(1 - x)$ filled with air

$$\epsilon_{dry} = x \cdot \epsilon_{poly} + (1 - x) \cdot \epsilon_{air} \tag{4.2}$$

Second, during the swelling, PEMs take up water. This water absorbs in two different ways. One part leads to a swelling and is denoted by swelling coefficient S (Equation 4.1). The second part fills the voids with water. The permittivity of a fully swollen film

$\epsilon_{swollen}$ can be described by the permittivity of the water ϵ_{H_2O} and Equation 4.2 with water filled voids

$$\epsilon_{swollen} = S \cdot \epsilon_{H_2O} + (1 - S) \cdot [x \cdot \epsilon_{Poly} + (1 - x) \cdot \epsilon_{H_2O}] \tag{4.3}$$

Fits were carried out with a self-written Python program where measured refractive indices were transferred to permittivities.[138] Here, x was fitted with the least-squares method. In contrast to a former publication,[49] where the linear combination was based on the refractive index, microscopic properties of the medium were the basis of the calculation. Therefore, the polymer fraction x differs slightly but is now based on the polarizability of the respective medium. Calculated values were transferred to refractive index for comparison to experimental values by $n_D = \sqrt{\epsilon}$.

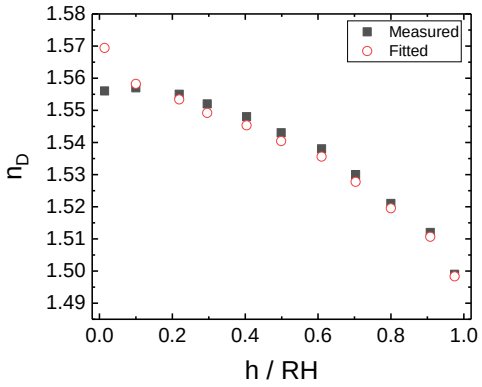

Figure 4.3: Comparison of measured and fitted refractive indices for a PEM of 29 single layers according to the *void model* as a function of relative humidity h. Error bars of the measured values are within the size of the symbols.

This linear combination is the simplest description. Figure 4.3 shows that the linear combination fits well above 20% RH. For $h < 20\%$ RH the fitted data are higher than the measured ones because it is assumed that the voids are filled either by air or water. A gradual filling of the void is not assumed and leads to a mismatch at low humidity.

Extended Void Model

The extended void model assumes that voids are filled with water following a linear trend as a function of the swelling coefficient during increasing h. Above a certain value, it is assumed that voids are completely filled with water. Further water uptake will then result only in swelling of the PEMs. Hence, a new equation is formulated for the permittivity

$$\epsilon_{swollen} = S \cdot \epsilon_{H2O} + (1 - S) \cdot [x \cdot \epsilon_{Poly} + (1 - x) \cdot (a \cdot \epsilon_{H2O} + (1 - a) \cdot \epsilon_{air})] \tag{4.4}$$

The factor a describes the ability of the air-water exchange in the voids and can be described as a function of S containing a linear and a constant part

$$a = \begin{cases} b \cdot S, & \text{for } S < 0.08 \\ 1, & \text{for } S \geq 0.08 \end{cases} \tag{4.5}$$

Other transition values lead to a discontinuity for the fitting parameter a as shown in the Appendix. The fitting parameters b and x will be determined during the fitting procedure using a Python script that was written for this study, where measured refractive indices were transferred to permittivities.[138] For the fitting procedure Equation 4.4 is rearranged by using the permittivities of water ($\epsilon = 1.777$) and air ($\epsilon = 1$) as

$$\epsilon_{swollen} = S \cdot 1.777 + (1 - S) \cdot [\epsilon_{dry} + a \cdot (0.777 - 0.777 \cdot x)] \tag{4.6}$$

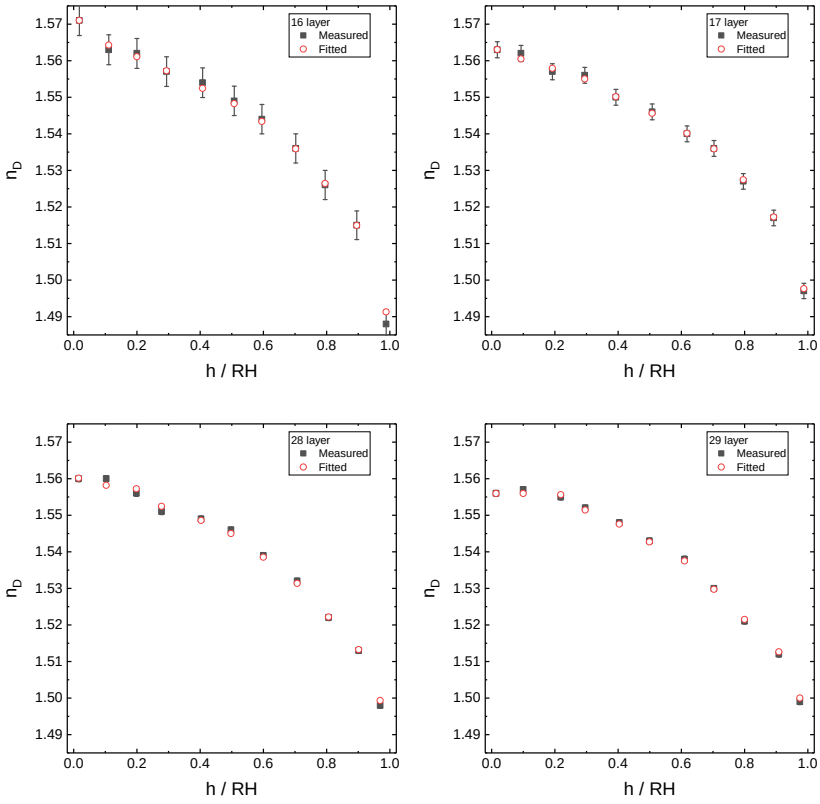

Figure 4.4: Comparison of measured and fitted refractive indices as a function of h according to the *extended void model*. Error bars of the measured values are partially within the size of the symbols.

Figure 4.4 shows measured and fitted data. Calculated values were transferred to refractive index for comparison to experimental values by $n_D = \sqrt{\epsilon}$. The fitted refractive indices are in good agreement with the measured data over the entire humidity range. The fitted parameter are shown in Table 4.1. From these results, the void fraction inside dry PEMs can be calculated. On average, PSS/PDADMAC PEM have a void fraction of 0.05 ± 0.01. This void fraction increases from 0.033 to 0.064 with increasing layer number. The parameter b increases from 11.0 to 13.7 with increasing layer number. It is worth noting that the amount of water does not show any odd-even effect. This is in good agreement with Zerball *et al.*,[49] where the odd-even effect was found for measurements in liquid water but not for humid air. Additionally, the refractive index of the pure polymer matrix can be calculated with Equation 4.2 and it is on average 1.592 ± 0.002.

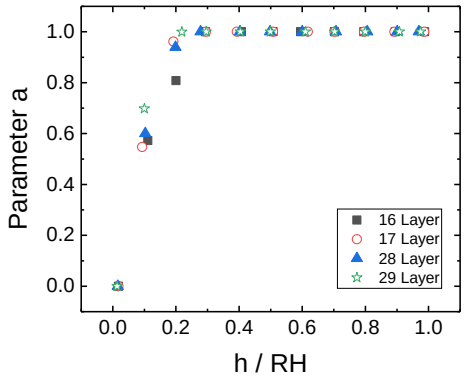

Figure 4.5: Parameter a as a function of h and layer number.

Table 4.1: Fitted values obtained with the *extended void model*.

Layer number	Outermost layer	x	b	n_{poly}
16	PDADMAC	0.967 ± 0.002	11.0 ± 2.0	1.590
17	PSS	0.953 ± 0.001	13.4 ± 0.9	1.591
28	PDADMAC	0.944 ± 0.002	13.0 ± 1.0	1.593
29	PSS	0.936 ± 0.001	13.7 ± 0.6	1.594

Factor a of the initial Equation 4.4 can be calculated by Equation 4.5. The results are shown in Figure 4.5. It is shown that above 30% RH, the voids are completely filled with water without any discontinuity in the trend of parameter a. This threshold of 30% RH does not change either with layer number or with the outermost layer.

4.3 Discussion

This chapter addresses the swelling behavior of PSS/PDADMAC PEMs. Increasing relative humidity (h) leads to nonlinear PEM swelling. The swelling coefficient S describes the fraction of absorbed water which leads to a swelling and is independent of the layer number. This is in agreement with Zerball *et al.*[49]

The swelling behavior can be explained as follows: Most of the charges are intrinsically compensated by the polyelectrolyte-polyelectrolyte complexes due to the low salt concentration.[125] Nevertheless, some charges are extrinsically compensated by small counterions. This induces an osmotic pressure as h increases. Three swelling regimes can be identified for PSS/PDADMAC PEMs. Due to extensive swelling at humidities of $< 40\%$ RH and the resulting counterion hydration, the voids are entirely filled with water. Above 40% RH, the swelling increment flattens and increases again above 60% RH. The polyelectrolyte chains become more flexible, which leads to a gain in entropy and favors further water uptake.

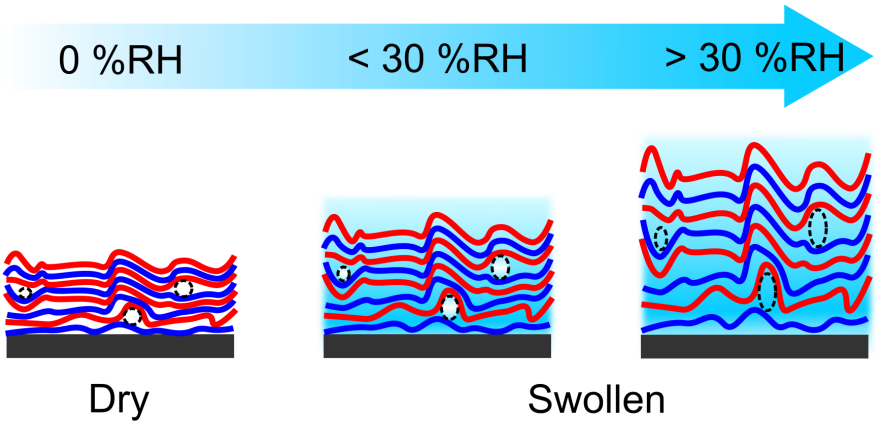

Figure 4.6: Schematic description of water uptake. Up to 30 %RH, the air inside the voids (white circles) is exchanged with water. Concurrently, the entire PEM begin to swell. The sum of both effects leads to a slight decrease of the refractive index. Above 30% RH, the voids are filled with water and a further water uptake leads to further swelling in thickness and a strong decrease in refractive index.

Figure 4.6 shows the proposed model for water uptake of PEMs. PEM consists of a layered polymer network, where the consecutive layers interdigitate strongly. When some specific layers are deuterated, neutron reflectometry can give insight into the structure.[139] In contrast to solid matter, e.g., mesoporous silica, PEMs are very flexible. Therefore, it is not possible to determine a pore diameter with adsorption measurements. When the humidity is changed, the voids change in size and shape to minimize the internal stress. Thus, a clear description of the structure is not possible yet. That explains why none of the basic adsorption models for pore condensation describe the experimental

adsorption isotherms of the present study. However, no model has been reported that can describe how the voids are filled with water. Indeed, Equation 4.6 takes into account the air-water exchange between 0% RH and 30% RH. In this range, a smooth decrease of the refractive index is observed, while at the same time, a strong increase in thickness is observed. This reflects two counteracting effects. First, swelling and water absorption of the PEMs results in a decrease in refractive index. Second, air inside the voids is replaced by water, which leads to an increase in refractive index. The sum of both effects leads to a slight decrease of the refractive index with increasing h. Above 30% RH, the voids are fully filled with water and the decrease of the refractive index only depends on the water uptake during the swelling procedure.

As a first approach, we assumed a linear filling for the voids up to 30% RH. It is possible to calculate the void fraction $(1 - x)$ by using the results shown in Table 4.1. The void fraction is on average 0.05 ± 0.01. It is in good agreement with Zerball *et al.* and Köhler *et al.* although our derivation based on the permittivity is slightly different.[47,49] In comparison to PSS/PAH PEMs the void fraction is low. Delajon *et al.* and Köhler *et al.* reported a void fraction up to 0.25 (published data were converted to void fraction; see Appendix).[47,140] This difference between these two systems, namely PSS/PDADMAC and PSS/PAH, can be explained by the different chain mobility and charge density along the chain.[47,54]

With changing the outermost layer, the swelling behavior of the entire PEM does not change. Similar results were reported by Köhler *et al.* and Zerball *et al.*[47,49] A change with respect to the outermost layer is known as the odd-even effect. This effect was shown for PSS/PDADMAC immersed in liquid water but not in humid air.[37,47,49] In contrast to the swelling behavior, which is independent of the number of adsorbed layers, the ability to fill the voids with water increases with the layer number. This is given by an increase of the parameter b with increasing layer number (see Table 4.1). Additionally, the void fraction $(1 - x)$ increases from 0.033 to 0.064. This is related to the internal structure which is influenced by the layer deposition procedure. The buildup of PSS/PDADMAC PEM is well-investigated, and it is shown that the growth with layer deposition switches from an exponential growth to a linear growth after 24 single layers.[30,49,130] An exponential growth occurs when the thickness increment increases with further layer deposition. Otherwise, the thickness increment is constant with layer deposition and a linear growth is observed. This is associated with the diffusion model where the PEM is subdivided into three zones: the substrate influenced zone, the reconstructing zone, and the diffusion zone as introduced in Chapter 2.[30–32]

The void fraction increases with increasing thickness of the diffusion zone. As shown in Table 4.1, a linear growth regime is not observed for all of the investigated samples. Therefore, the diffusion zone of PEM with 29 and 28 single layers is more pronounced than the one with 17 and 16 single layers. Thus, the void fraction increases with layer number. PEM with a layer number above 22 single layers should show a constant void fraction as shown by Zerball *et al.*[49] The increment of the void fraction decreases with layer number which can lead to a constant void fraction for higher layer numbers.

4.4 Conclusion

PEMs swell in a nonlinear fashion with increasing h. When the swelling coefficient S is calculated, volume fraction of absorbed water is independent of the layer number. Concurrently, the refractive index decreases and can be described by the *void model*. However, for a more exact description over the entire humidity range, the *extended void model* is required.

The *extended void model* assumes a gradual air-water exchange in the low humidity range up to 30% RH. This model describes trends and absolute data over the entire humidity range. The fitting procedures show that above 30% RH the voids are completely filled with water. Additionally, it is possible to extract further information about PSS/PDADMAC PEMs by analyzing the fitting parameter. The refractive index of the pure polymer matter is determined as 1.592 ± 0.002. It is shown that the volume fraction of the voids is on average, 0.05 ± 0.01 and it increases with the layer number. This model is not limited to the shown PSS/PDADMAC PEMs. It can be generalized to all other types of coatings, which swell in surrounding solvents.

PEMs are able to absorb and release immobilized guest molecules, e.g., drugs, nanoparticles, or dyes. The knowledge about the amount of voids and how they are filled with solvent opens the possibility to tailor, very precisely, PEMs for prospective applications. Therefore, it is crucial to understand and to predict the internal composition as well as the response to outer stimuli. In addition, knowledge about the mobility of water and of guest molecules under different humid conditions would be useful. These studies might help to improve stimuli sensitive delivery systems which can potentially be applied in medical applications or in anticorrosive coatings where PEMs serve as stimuli sensitive barriers.

5 Polyelectrolyte Multilayers and Brushes: Mutual Interactions and Swelling Behavior

Similar content is published in "Swelling Behavior of Composite Systems: Mutual Effects between Polyelectrolyte Brushes and Multilayers" Oliver Löhmann, Samantha Micciulla, Olaf Soltwedel, Emanuel Schneck and Regine von Klitzing, *Macromolecules* (2018), 51 (8), 2996 - 3005 https://dx.doi.org/10.1021/acs.macromol.8b00359

Abstract

Based on the last chapter, the concept of thin coatings is extended by combing PEMs and brushes. The PEMs and end-grafted brushes represents a valuable approach to the design of complex organic composite materials with tailored responsive properties. This chapter addresses the correlation between the swelling properties of composites and their internal structure. Here, composites are presented consisting of end-grafted PMETAC brushes covered with PSS/PDADMAC PEMs and are characterize under various relative humidities. Ellipsometry and neutron reflectometry are carried out to monitor the swelling behavior and the internal structure, respectively, of the composites, giving evidence of a significant mutual influence of the two components. The reflectivity data reveal a deep penetration of the PEMs' polyelectrolyte chains into the underlying brush but also a significant humidity dependence of their spatial distribution, indicating considerable mobility within the brush. In contrast to a compact bare brush, for composites a pronounced stretching of the brush after PEM adsorption is observed. The water uptake of the brush is reduced. A PEM on top of a brush is less influenced by the latter one. Swelling gradually reduces the brush/PEM interpenetration, while water accumulates in the interfacial region between the brush and PEM so that these two compartments get increasingly separated with increasing humidity. The swelling process is largely reversible, which demonstrates the potential applicability of these composites as chemical gas or moisture sensors.

5.1 Introduction

Polymer coatings find broad application in materials science and technology since they change the surface properties of many substrates without altering their bulk properties.

One of the simplest routes to preparing polymer coatings is the adsorption of polyelectrolytes parallel to a surface by the layer-by-layer technique.[1,2]

Thereby, the strength of complexation plays an important role and can be controlled by choosing either strong or weak polyelectrolytes[28,121,141] and the dipping parameters.[15,126] This layer-by-layer growth of PEMs is well understood and has been discussed in several papers.[32,40,129,130] Typical adjustable parameters are the type and concentration of the polyelectrolytes and of the added salt, the pH, and the dipping time. For fundamental research, PSS, PDADMAC, and PAH are very commonly used.[47] The preparation of PEMs has also involved the use of biomolecules,[142] clays,[100] and nanoparticles[143] to achieve the desired surface properties.

The functionality of PEMs is determined by their chemical composition. External stimuli can induce a response of the polymer conformation and, in turn, change their functional properties.[123] As an example, planar adsorbed PSS/PDADMAC PEMs respond to ionic strength and water content in the environment but less to thermal treatment.[34,37] In general, PEMs act like a sponge with reversible water absorption. When immersed in water, PEMs swell and the polymer network expands. This enhances the uptake and release of target molecules with respect to the dry state. The reversibility of this process allows the immobilization of target molecules by drying the PEMs and releasing these molecules under controlled conditions afterward.[144] With that, PEMs can be used as tunable carrier and delivery systems as well as a protective coating.[121,145]

Instead of being physisorbed, polyelectrolytes can also be chemically end-grafted onto a solid substrate. This brush conformation provides a predominantly perpendicular orientation, high mechanical stability, and tunable density. The two most commonly used brush preparation methods are the grafting-to and the grafting-from approaches.[58] The latter yields higher grafting densities and a low polydispersity. Similar to PEMs, brushes are responsive to various external stimuli and can undergo structural changes,[72,73] which renders them promising building blocks for smart coatings in chemical sensing and drug delivery.

The combination of end-grafted brushes and adsorbed PEMs has been exploited for the design of robust, multifunctional coatings.[10,24] In such coatings, tailored structural rearrangements upon specific stimuli could potentially be used for chemical sensing or molecular recognition or trigger the uptake and release of substances. Furthermore, composites of polyelectrolyte brushes and PEMs open novel technical applications in which PEMs are used as sacrificial layers to protect and release embedded molecules under certain conditions.[90,91]

As Rühe and co-workers demonstrated, polyelectrolyte brushes are suitable as substrates for PEMs,[24] accounting for a pronounced diffusion of the first layer into the brush which creates an intermixing zone between the two compartments. Nevertheless, complete charge compensation does not occur so that oppositely charged polyelectrolytes further adsorb and a PEM can be built up via the layer-by-layer technique.[92,93] For brushes with high grafting and charge densities, the resulting brush-supported PEMs are found to be homogeneous.[24,92] Recent studies on brush/PEMs composites featuring temperature sensitivity reveal that mutual interdiffusion and the ensuing molecular interactions are responsible for their responsive properties. Detailed insight into the internal

structure of polymer composites is of crucial importance to the design of functional coatings with desired properties.[10]

Here, ellipsometry and NR were used to structurally investigate well-defined composite systems constituted of charged homopolymer (PMETAC) brushes covered with PEMs of pairs of strong polyelectrolytes, namely PSS and PDADMAC. The use of strong polyelectrolytes prevents pH dependence and leads to the formation of PEMs with a strong humidity response yet a weak temperature response.[49,61] By monitoring the change in composition with varying humidity, it is possible to understand the level and relevance of mutual interactions between the two compartments. Therefore, relative humidity is a suitable stimulus for investigating responsive behavior.[34]

This chapter focuses on the characterization of the swelling behavior of brush/PEM composites compared to the single, individual components. Furthermore, the influence of the PEM thickness on the structure and properties of the composites is investigated.[61,94] The humidity-dependent distributions of polyelectrolytes and water in brush/PEM composite systems have so far been unknown. Ellipsometry data show that the overall swelling of single brushes, single PEMs, and a combination of both follows the same trends but differs in the absolute swelling level. Deeper insight into the internal composition can be achieved by neutron reflectometry. Partial deuteration of the PEM has been used to generate a contrast between the brush and PEM. This allows us to study the internal composition during swelling. A fitting procedure based on the volume fractions of all chemical components opens the possibility to investigate the water distribution as a function of humidity along the surface normal.

5.2 Results

The thickness increment as a function of the relative humidity h as obtained by ellipsometry can be expressed in terms of the swelling coefficient S (see Equation 2.4).

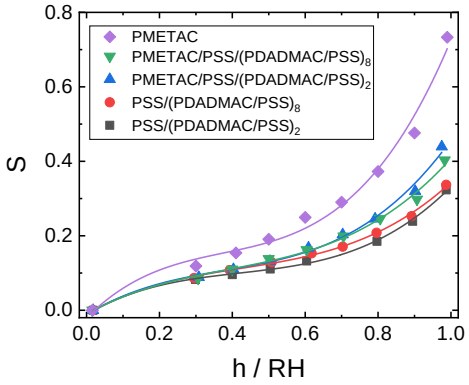

Figure 5.1: Swelling behavior as obtained by ellipsometry of the PMETAC brush, PDADMAC/PSS PEM with different layer numbers, and a combination of both. Corresponding lines are fits with a third-order polynomial.

The experimental data reported in Figure 5.1 demonstrate that the system components, brush and PEM, have different swelling behaviors as individual coating compared to the composite systems. The bare brush swells by up to 73 % of its original thickness, while PEMs swell by only up to 33 % irrespective of their layer number. This is in agreement with the results shown in Chapter 4. The composites have an intermediate degree of swelling compared to the individual components. All swelling curves can be described empirically by a third-order polynomial, as shown by the solid lines in Figure 5.1. This finding motivates the third-order polynomial description of the humidity dependence of Equation 3.30 in the NR analysis (Methods section).

In the following section, the analysis and the interpretation of the NR data are described, which reveal the internal composition of the brush/PEM composites and their response to humidity changes.

5.2.1 Bare Brush

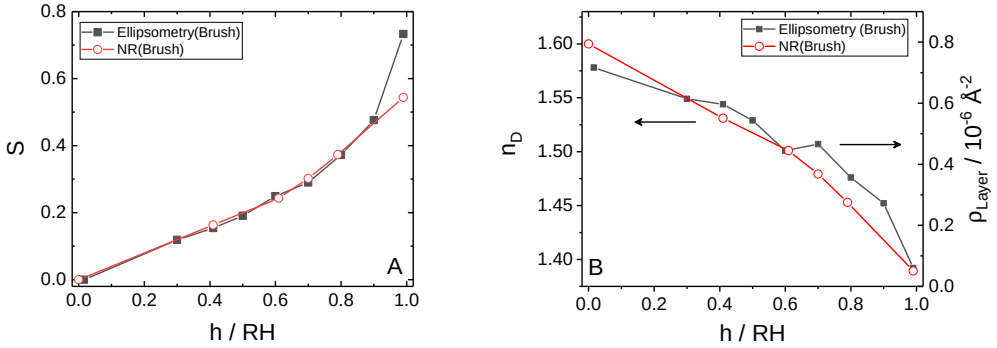

Figure 5.2: Bare PMETAC brush as a function of h measured with ellipsometry (black squares) and neutron reflectometry (red circles). (A) Swelling S. (B) Refractive index n_D and scattering length density ρ_{layer}. This SLD corresponds to the plateau value of the SLD profile.

Figure 5.2 shows the swelling coefficient (left) and its optical constants (right) of the bare brush, namely the refractive index n_D and scattering length density (SLD) ρ_{layer} of the brush/water combined layer as a function of h. The brush thickness measured by ellipsometry increases from 235 to 881 $\AA$ with increasing relative humidity from 0% RH to 99% RH. For NR, the thickness d_{PMETAC} is obtained as the distance from the substrate where the SLD of the polymer layer is half of its plateau value.

The swelling is found to be virtually identical for ellipsometry and NR measurements except for the measurements taken at 99% RH, where the thickness is very sensitive to minor yet inevitable humidity deviations from the nominal value. Figure 5.2 shows that the humidity-dependence of the optical constants of ellipsometry and NR measurements shows very similar trends. This underlines that the models used for the sample description are consistent for both techniques.

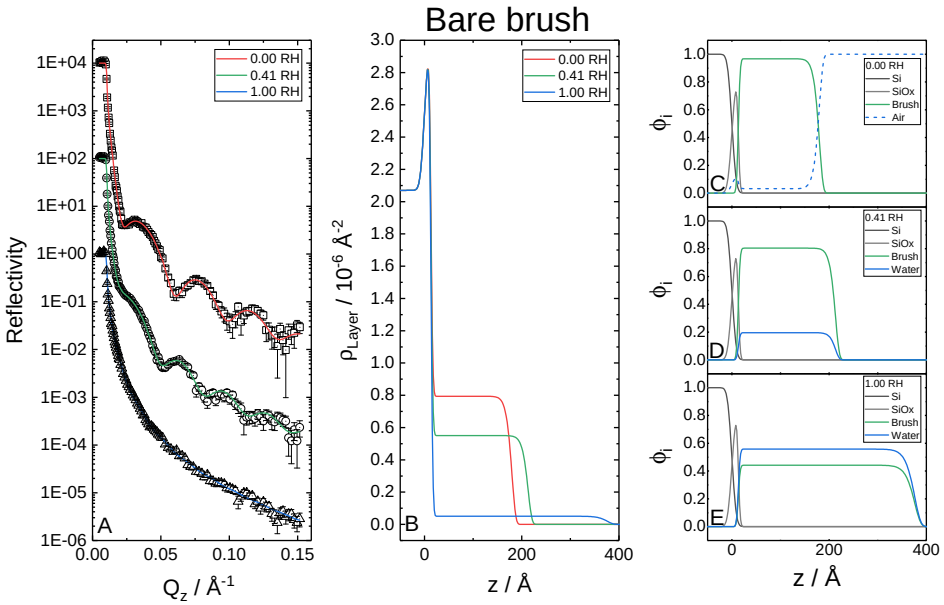

Figure 5.3: (A) Reflectivity data of three measurements and the corresponding fits at 0% RH, 41% RH, and 100% RH of a bare brush. (B) Corresponding SLD profiles. (C) Volume fraction profile at 0% RH. (D) Volume fraction profile at 41% RH. (E) Volume fraction profile at 100% RH.

NR data, fits, SLD profiles, and volume fraction profiles at three selected humidities are reported in Figure 5.3 (The entire data set is shown in the Appendix). The scattering length density ρ_{PMETAC} of the brush monomer is obtained as 0.82×10^{-6} $\AA^{-2}$. This value is used as a reference for the data analysis of the composite material and agrees well with the theoretical estimate of $\rho = 0.88 \times 10^{-6} \AA^{-2}$ based on a recent report on the METAC monomer volume to be $V_{ME} = 262$ $\AA^3$.[7] The analysis also shows that the dry brush has an almost negligible void fraction of 3 %.

Figure 5.3A shows reflectivity data of measurements at three selected relative humidities. With increasing humidity, minima in the reflectivity data move closer together, corresponding to an increase in brush thickness. At the same time, the scattering contrast decreases as shown in the corresponding SLD profiles in Figure 5.3B. These two effects originate from the uptake of water ($\rho_{H_2O} = -0.56 \times 10^{-6}$ $\AA^{-2}$) and the associated swelling of the polymer film. The data set can be described by homogeneous layers with comparatively sharp outer surfaces (Figure 5.3 C-E), corresponding to high values of the stretching exponents in Equation 3.29, $n > 22$. The water fraction increases from 20 % at 41% RH to 56 % at 99% RH. The brush retains a compact conformation over the entire humidity range, in line with the low outer roughness of 7 ± 1 $\AA$ for PMETAC brushes under ambient conditions determined by AFM.[146]

5.2.2 Brush/PEM Composite

To understand the influence of brush/PEM interactions on the swelling behavior of the composite, the characterization of their internal composition is essential. In order to investigate the influence of the deposited layer numbers on the internal structure and the swelling behavior of the resulting composites, two composites were selected for NR experiments with 5-layer and 17-layer PEMs, in the following referred to as thin and thick samples, respectively. Before being coated with PEM, the supporting brushes had similar thicknesses of about 240 $\AA$ at 0% RH in both cases.

Figure 5.4 and 5.5 show three example NR data at selected humidities, the best fits, the corresponding SLD profiles and the volume fraction profiles for both composites (Entire data sets are shown in the Appendix). SLDs obtained for the PEM of the thin and the thick samples are $\rho_{PEM} = 3.96 \times 10^{-6} \AA^{-2}$ and $3.85 \times 10^{-6} \AA^{-2}$, respectively. This remarkable agreement between the two independently fitted samples indicates the robustness of the data.

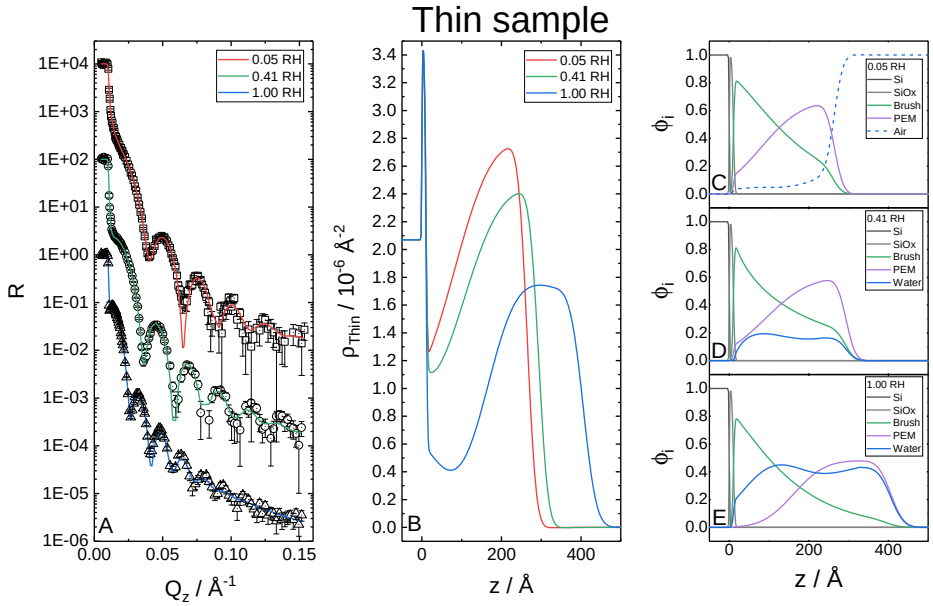

Figure 5.4: (A) Reflectivity data of three measurements and the corresponding fits at 5% RH, 41% RH, and 100% RH of the thin sample brush. (B) Corresponding SLD profiles. (C) Volume fraction profile at 5% RH. (D) Volume fraction profile at 41% RH. (E) Volume fraction profile at 100% RH.

The obtained humidity-independent parameters are shown in Table 5.1. The equivalent thickness of the brush, D_{brush}, for the thin and thick samples is similar to $D_{brush} = 129$ $\AA$ (see Equation 3.32). The equivalent thickness of the PEM D_{PEM} is about 3.5 times

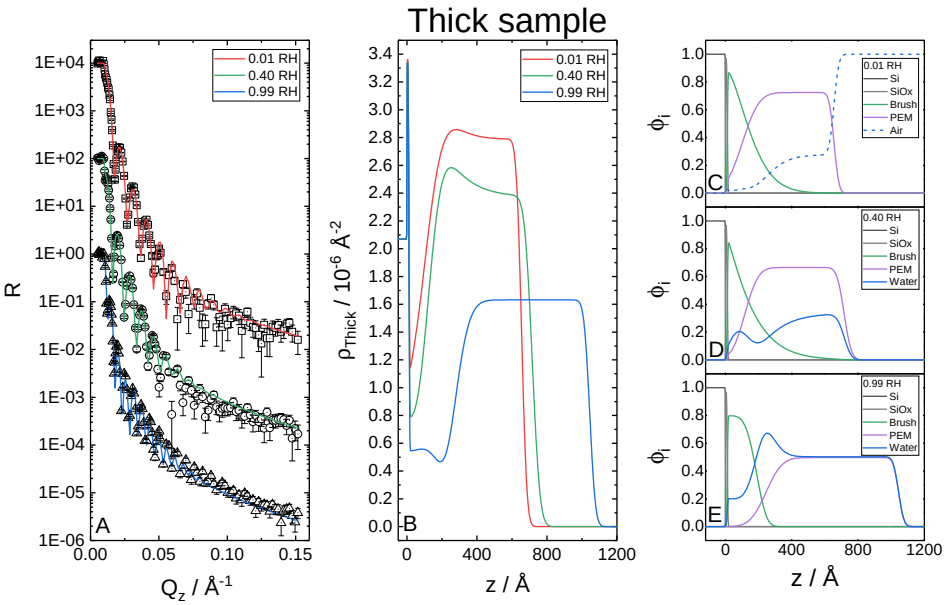

Figure 5.5: (A) Reflectivity data of three measurements and the corresponding fits at 1% *RH*, 40% *RH*, and 99% *RH* of the thick sample. (B) Corresponding SLD profiles. (C) Volume fraction profile at 1% *RH*. (D) Volume fraction profile at 40% *RH*. (E) Volume fraction profile at 99% *RH*.

higher for the thick sample, but the thickness per polyelectrolyte layer of 23.4 *Å* is the same for both samples, meaning a constant layer increment per deposition in both samples.

The corresponding volume fraction profiles are shown in Figures 5.4 C-E and 5.5 C-E. In presence of both thin and thick PEM, the polyelectrolytes have a pronounced overlap with the brush region, even reaching down to the silicon surface with the tail of their distribution. The brush assumes a stretched conformation for both composites in the dry state. In the thin sample, the periphery of the brush reaches the composite-air interfaces, meaning that the entire PEM compartment has infiltrated the PMETAC brush. In contrast, the brush underneath the thick sample does not penetrate the entire multilayer, so a considerable fraction of the PEM compartment remains pure i.e., PMETAC-free.

Both composites have a void volume filled with air under dry conditions. The thin sample has a void fraction below 5 % near the substrate. The PEM region exhibits a significantly higher void fraction, most pronounced for the thick sample, where it reaches to 27 %. The difference can be related to the fact that there is an essentially brush-free PEM region featuring the intrinsic properties of pure PEMs in the thick sample.

With increasing relative humidity, the entire system swells and the internal configuration rearranges. The brush inside the thin sample takes up to 40 % water and keeps

Sample	SLD(Brush) $[10^{-6}Å^{-2}]$	SLD(PEM) $[10^{-6}Å^{-2}]$	D(Brush) $[Å]$	D(PEM) $[Å]$	D(PEM)/layer no. $[Å]$
Bare brush	0.82		158		
Thin sample	0.82	3.96	119	117	23.4
Thick sample	0.82	3.85	138	397	23.4

Table 5.1: Conserved parameters for each data set during the fitting procedure. These values are humidity-independent for each data set.

a stretched conformation. In contrast, the brush inside the thick sample undergoes a change from a stretched to a significantly less extended conformation above 60% RH, as encoded in the increase in the stretching exponent with increasing humidity (Figure 5.6). This behavior is substantially different from the sharp interface of the bare brush, with $n > 22$. It shows that the conformation of the brush is strongly influenced by the surrounding medium, here air or PEM. The PEM in both composites increases in thickness, and its center of mass gets displaced away from the surface with increasing humidity. The overall shape of the PEM is preserved during swelling.

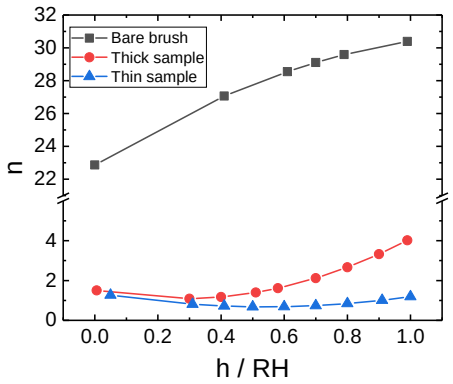

Figure 5.6: Exponent of the analytical function of the brush for the bare brush and the thin and the thick composites.

As shown in Figures 5.4 and 5.5, the water distribution is heterogeneous along the composite profile and changes upon swelling. In the thin sample, the volume fractions of absorbed water inside the brush close to the substrate and inside the outermost part of the PEM compartment are similar and reach 40 % at high humidity. In the transition region between the brush and PEM, a minimum in the water content is observed over the entire humidity range. In the case of the thick sample, the brush takes up a smaller amount of water than in the thin sample, but the PEMs in the thin and thick samples show roughly the same swelling behavior. Analogous to the other composite, the water content is minimal in the brush/PEM transition region below 60% RH. However, this minimum vanishes at higher humidities, and a maximum water content is found.

Quantifying the humidity-dependent relative water content in each component of the composite is nontrivial, because brush, PEM, and water coexist in a wide z range so that one cannot easily attribute the water to one of the organic components. In the following, an alternative route was taken based on the overlap integrals $I_{i,H2O}(h)$ between water and each of the organic components. These integrals provide a meaningful measure of the colocalization of water with the brush or PEM and are given by

$$I_{i,H_2O}(h) = \frac{1}{D_i} \int_{-\infty}^{+\infty} \phi_i(z,h) \cdot \phi_{H_2O}(z,h)\ dz \tag{5.1}$$

where i refers to either PMETAC or PEM, D_i is the equivalent thickness of the respective component, and ϕ_i the corresponding volume fraction profile. The separation with increasing h can be quantified by the brush/PEM overlap integral $I_{brush,PEM}(h)$ with respect to the dry state by

$$I_{Brush,PEM}(h) = \frac{\int_{-\infty}^{+\infty} \phi_{PMETAC}(z,h) \cdot \phi_{PEM}(z,h)\ dz}{\int_{-\infty}^{+\infty} \phi_{PMETAC}(z, h \approx 1\%\ RH) \cdot \phi_{PEM}(z, h \approx 1\%\ RH)\ dz} \tag{5.2}$$

During composite swelling, $I_{i,H_2O}(h)$ increases while $I_{brush,PEM}(h)$ decreases monotonically. With increasing h, both brush and PEM take up water and their separation increases. Figure 5.7A shows that the brush/PEM overlap inside the thin sample is reduced down to 40 % of its initial value under dry conditions and the hydration of both compartments increases up to 40 % at the same time. The brush of the thin sample at the highest hydration is associated with only about half as much water ($I_{brush,H_2O}(99\%\ RH) \approx 40\ \%$) as the bare brush, for which $I_{brush/H_2O}(99\%\ RH) \approx 70\ \%$. This effect is even more pronounced for the thick sample, for which $I_{Brush/H_2O}(99\%\ RH)$ is only $\approx 30\ \%$. For the PEMs the situation is reversed ($I_{PEM/H_2O}(99\%\ RH) = 39\ \%$ for the thin sample and $I_{PEM/H_2O}(99\%\ RH) \approx 51\ \%$ for the thick sample), and both take up more water than PEMs on a solid substrate (only up to 33 % at 99% RH). This can be correlated to swelling coefficient S in Figure 5.1, which for a two-component system containing only PEM and water strictly coincides with the corresponding overlap integral I_{PEM/H_2O}. The separation of brush and PEM upon hydration is much more pronounced for the thick sample, with the overlap going down to 10 % with respect to the dry state (Figure 5.7B). As suggested by the overlap integrals and seen in Figure 5.4C-E and 5.5C-E, the transition region between brush and PEM takes up water disproportionally with increasing humidity for both samples.

Both composites are measured under dry conditions again after a full swelling cycle. Figure 5.8 shows the reflectivity data before and after the swelling. The reflectivity data of both samples shift slightly to lower Q_z values, which indicates a slightly higher thickness after the swelling. At the same time, the intensity ratio between maxima and minima decreases. That arises from a lower contrast within the sample and thus from a higher intermixing into each other after the swelling.

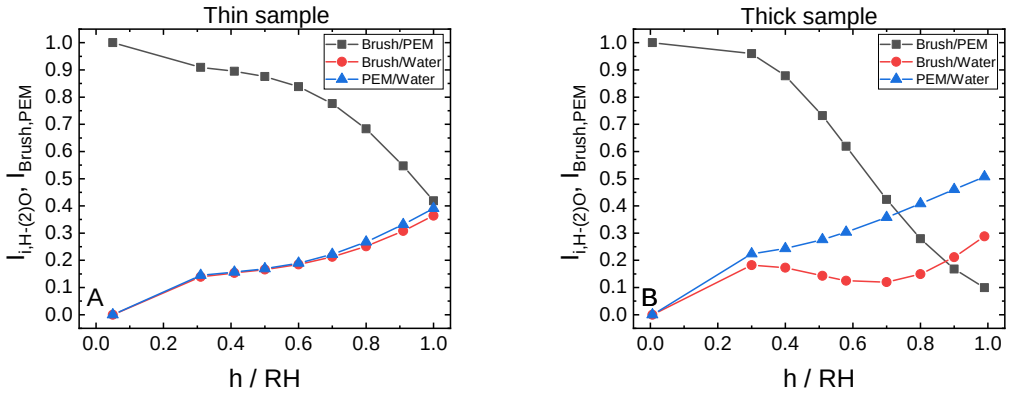

Figure 5.7: Overlap integrals of the thin sample (A) and thick sample (B). With increasing relative humidity $I_{Brush,PEM}(h)$ decreases and $I_{i,H_2O}(h)$ increases.

5.3 Discussion

The results presented in the previous section show that measurements of the overall swelling alone do not reveal all relevant aspects of the response of brush/PEM composites to hydration. Instead, additional information on the humidity-dependent internal composition, as accessible by NR, is required.

NR reveals a strong overlap of the brush and PEM. The brush is in an extended conformation, as encoded in an elevated SLD near the solid substrate with respect to the pure brush. Zhang *et al.*[24] observed a strong collapse of the cationic brush (MePVP) caused by exposure to a PSS solution studied by ellipsometry. Laurent *et al.*[93] showed that the PEM uptake increases with increasing grafting density of a cationic brush (PTMAEMAI). The latter emphasizes a strong overlap of brush and PEM as found in the present studies. The considerable overlap due to entropy-driven complexation between PMETAC and PSS can be explained by the high counterion density in the brush. Counterions can be distributed over a larger volume when the charged brush overlaps with the net-neutral PEM region incorporating only a few ions. Furthermore, the fact that the composites' internal composition is sensitive to hydration indicates that the negatively charged polyelectrolyte chains are only loosely integrated into the positively charged brush rather than firmly complexed. All charges of the brush cannot be compensated for by PSS due to steric reasons and a certain number of counterions are assumed to remain within the brush, which allows its swelling. This suggests that complexation between the PMETAC chains and the negatively charged PSS chains is less effective than between the polyelectrolyte pairs forming the PEM.

The brush's conformational change and water uptake are more strongly affected by the presence of PEMs than the behavior of the PEMs is affected by the supporting brush. This observation can be rationalized by the different properties of each compartment. The brush itself carries a high net charge density and is therefore more sensitive to the presence of oppositely charged polyelectrolyte chains. The PEMs, whose intrinsic feature

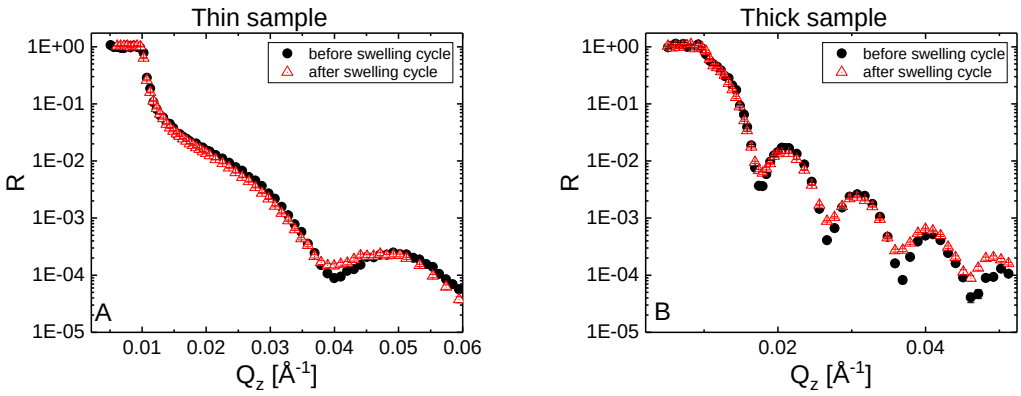

Figure 5.8: Reflectivity data before (black closed symbols) and after swelling (red open symbols) of the thin sample (top) and thick sample (bottom) under dry conditions. After a full swelling cycle, both samples achieve almost the same conformation. A small reorganization is observed, but the main features are preserved.

is the complexation between oppositely charged polyelectrolytes, are less sensitive to that. Moreover, the amount of PEM in the thick sample is much larger than the brush amount, so the mutual interaction affects the entire brush region but only a part of the PEM region.

Thus, the brush has a minor effect on the PEM. The growth of the PEM is not affected, and a constant increment of 23.4 Å per layer pair is observed, the same as on a silicon wafer. The void fraction of 27 % is higher than for PEMs on silicon (5 %), as reported in Chapter 4, showing that the PEMs in composites are more loosely packed. Although different methods have been used in all studies, the remarkable difference in void fraction can always be linked to a higher concentration of counterions released from the brush during PEM growth. The brush is more strongly affected by PEM capping. The bare brush has a low void fraction of 3 % due to a high grafting density which does not change with the adsorption of PEM. This is explained by the simultaneous stretching of the brush upon polyelectrolyte penetration.

After the description of mutual effects of brush and PEM, attention is now drawn to the water uptake of the brush/PEM transition region. At low relative humidity, water uptake is minimal in the brush/PEM transition region. At higher humidity (above approximately 60% RH), the situation is reversed, and water uptake is most pronounced in the transition region so that a maximum in the water volume fraction emerges at the highest humidities (Figure 5.5E). At the same time, the two organic components gradually separate (i.e., demix) as quantified in terms of decaying overlap integrals (Figure 5.7). This behavior indicates that the molecular interactions are altered when water, as the third component, becomes more available at higher humidity. Under humid conditions, both organic components appear to prefer interacting with water rather than with one other. This leads to a depletion of polyelectrolytes from a former densely packed region,

and water can especially absorb into this region.

For technical applications, the long-time stability is an important factor. The reversibility of the swelling after the first swelling cycle (see Figure 5.8) makes these composites promising for applications such as chemical sensors and absorbers of volatile substances.

5.4 Conclusions

The internal composition of composite materials consisting of polyelectrolyte brushes coated with PEMs is resolved in a wide range of relative humidities using NR. It is also demonstrated that the number of deposited layers has an influence on the swelling behavior of a brush inside a composite. A simultaneous fit of the reflectivity data obtained for all humidities revealed that the brush and the PEM interdigitate strongly but increasingly separate upon swelling in humid air. Thereby, water accumulates in the transition region between the brush and PEM layers. Composites, such as the ones structurally characterized here, might be used as smart sensors with the ability to accumulate volatile molecules in the brush/PEM transition region at high humidity but push them toward one of the components at reduced humidity, where they can be physicochemically detected. Humidity-induced structural changes are found to be virtually reversible, which opens the possibility to release previously embedded molecules under defined conditions.

6 Polyelectrolytes and Halloysite Nanotubes

Experiments were carried out together with my student coworker Philipp Ritzert.

Abstract

This chapter extends the concepts of surface coating of the last two chapters by introducing Halloysite nanotubes (HNTs). HNTs are biocompatible, natural, tubular shaped alumosilicates particles. Due to different surface charges of the inner and outer surface, it is possible to selectively modify both surfaces. Furthermore, HNTs can be incorporated into PEMs since they carry an overall net charge. Alignment of HNTs can introduce anisotropy into the coating. In this thesis, different HNTs were characterized by TEM concerning their usability for anisotropic coatings. TEM measurements prove that HNTs, obtained from a Chinese source, are well defined with a sufficient high aspect ratio for alignment on a surface. In contrast, HNTs obtained from an American source are shorter and are not well defined in shape and length. Afterwards, HNTs were sprayed onto silicon wafers coated with different polyelectrolytes. The interaction between HNTs and PEI coated wafers is sufficient to obtain an alignment of HNTs on the surface. It is shown that a low liquid flow rate (0.2 mL/min) and a high gas flow rate (40 L/min) lead to a strong orientation of HNTs on the surface. The coverage is adjusted by the spraying time and concentration of the used suspension. The nematic order parameter S_n quantifies the orientation. Here, strongly aligned samples led to a nematic order parameter up to 0.81. Additionally, bilayers of HNTs and PEI were prepared which led to a fully covered surface. Therefore, HNTs are suitable for oriented surface coatings and can possibly be used for future applications.

6.1 Introduction

Thin surface coatings are a suitable approach to modify surface properties while not affecting the bulk properties of the underlying substrate. Among different coatings containing only organic polymers, e.g. polyelectrolyte multilayers[1,2] and polymer brushes,[80] the incorporation of inorganic particles into the polymer matrix came into the focus of interest. Clays, a class of natural minerals, combined with polymers are discussed in several papers.[95–98] Incorporated clays introduce further properties to thin coatings, e.g. mechanical strength,[147] optical properties,[148] or thermal stability.[149] Nevertheless, it is

often aimed that the polymer properties are preserved after incorporation of particles. For example, composites of montmorillonite clay nanosheets and PNIPAM show that the temperature response of PNIPAM retains after the incorporation of montmorillonite clay nanosheets while a decrease in permeability is introduced.[100] These multicompartment systems can be tailored in the nm-range depending on the preparation protocol. The used sheets, however, are isotropic in planar dimensions and thus the modulation of the properties is isotropic in lateral direction. Anisotropy occurs when specific properties are directionally dependent. Introducing anisotropic properties by using elongated particles, e.g., carbon nanotubes or gold nanorods, can lead to new properties.[76] Correa-Duarte *et al.* reported on carbon nanotubes coated with magnetic nanoparticles which can be aligned on a surface by a low magnetic field and can be used as building blocks for composites.[150] Gold nanorods are interesting for medical applications in the field of imaging. Huang *et al.* showed that an alignment shows a surface enhanced Raman scattering.[151] However, carbon nanotubes and gold nanorods[152] show cell toxicity and cannot be used without further modification.[77,152] Additionally, both are synthetic products and can be expensive and complex in synthesis depending on preparation. These disadvantages are incentives to identify new materials.

HNTs are a natural clay and can be obtained from mines.[75] They are cheap and biocompatible. HNTs are chemically similar to kaolin, consisting of silica and alumina sheets rolled into tubes. The lumen has a diameter of 10 to 20 nm, the external diameter varies from 50 to 100 nm and the length is between 0.5 to 2 μm.[75] This results in an aspect ratio of about $5 - 40$. Therefore, HNT introduce anisotropic properties when they are aligned on a surface.[80] The outer surface is predominated by silica and carries a negative surface charge while the inner surface is predominated by alumina and carries positive surface charge at intermediate pH. Due to different surface charges, it is possible to load the lumen with negative charged polymers,[80] surfactants,[81] alkanoates,[82] or drugs.[83] Yah *et al.* showed a selective PMMA modification of the lumen via ATRP.[85] They showed that the catechol group binds selectively to the alumina surface and a brush growth in the lumen. Furthermore, the silicon surface can selectively be modified with APTS or coated with thin PEMs which allows a controlled release of drug macromolecules from the lumen.[11,153] With this, HNTs are promising a multifunctional building block for bottom-up superstructures. The bottom-up approach allows to build up well tailored structures based on small repetitive units.[88,89]

This chapter focuses on the orientation of HNTs on flat surfaces by grazing incidence spraying (GIS).[101–104] Spray coating is a fast method to coat large areas and is well established in research and industry. With this method orientation of silver nanowires (aspect ratio about 90) was successfully reported.[104] A high aspect ratio benefits an orientation. From a sustainable and biocompatible point of view, however, silver nanowires are not suitable.[154] Although HNTs have a lower aspect ratio, Zhao *et al.*[80] showed that HNTs, loaded with PSS, align at the rim of an evaporating suspension droplet. Lumen loading promotes the colloidal stability of the suspension and the electrostatic repulsion between the single particles.[81,82] In this work, two different polyelectrolyte coatings were used to increase the adhesion of HNTs to the substrate and between different layers of HNTs. Therefore, silicon wafers were coated either with PEI or PSS/PDADMAC PEM prior to

the spray coating. The HNTs were characterized by transmission electron microscopy (TEM). Afterwards, spraying conditions were optimized to obtain monolayers and bilayers of HNTs. HNTs were successfully aligned on the surface over several micrometers and the coating were characterized with atomic force microscopy (AFM) and optical polarization microscopy. The nematic order parameter S_n was determined. It quantifies that the HNTs are strongly ordered at the surface. The successful alignment can be the basis to build up multilayer with a superstructure and therefore, to implement completely new surface properties. With that, aligned HNTs can be a prospective approach for anisotropic coatings or to mimic natural structures.[105]

6.2 Results

6.2.1 Halloysite Nanotubes and their Suspensions

HNTs are natural materials and thus they differ in shape and size distribution depending on the mine. Here, two different types of HNTs were characterized, obtained from a Chinese and from an American mine. TEM images of the different HNTs are shown in Figure 6.1. HNTs from China are well defined in shape and length. On average Chinese HNTs are longer and thus have a higher aspect ratio. Both samples clearly show hollow appearance. American HNTs have a thicker and more irregular wall packing. Suspensions are obtained by mixing HNTs with water. The electrophoretic mobility of the used HNTs is $3.8 - 3.9$ $\mu mcm/Vs$ independently of the mine (see Table 6.1). The zeta potential cannot calculated since the Smoluchowski equation is only valid for hard, non-porous, and spherical particles. The suspensions are semi-stable and the formation of a precipitate is observed within hours after preparation.

The stability of HNTs suspension is influenced by electrostatic repulsion of the dispersed particles. Zhao *et al.* reported on an increase of the surface charge by loading HNTs with PSS.[80] The same approach was used for further experiments. TEM images (see Figure 6.2) show no difference between loaded and pristine HNTs. The shape is unaffected and PSS is not visible due to low contrast. Additionally, the electrophoretic mobility does not change with PSS loading (see Table 6.1). Although no differences were observed, spraying experiments were carried out with PSS loaded Chinese Halloysites to compare the findings with the results reported by Zhao *et al.*[80]

Sample	Electrophoretic mobility [$\mu mcm/Vs$]	pH
HNT(American, pristine)	-3.8 ± 0.6	7.57 ± 0.01
HNT(Chinese, pristine)	-3.9 ± 0.7	7.27 ± 0.01
HNT(Chinese, PSS)	-3.9 ± 0.5	7.22 ± 0.01

Table 6.1: Electrophoretic mobility and pH of pristine and PSS loaded HNTs suspensions with Milli-Q water as solvent.

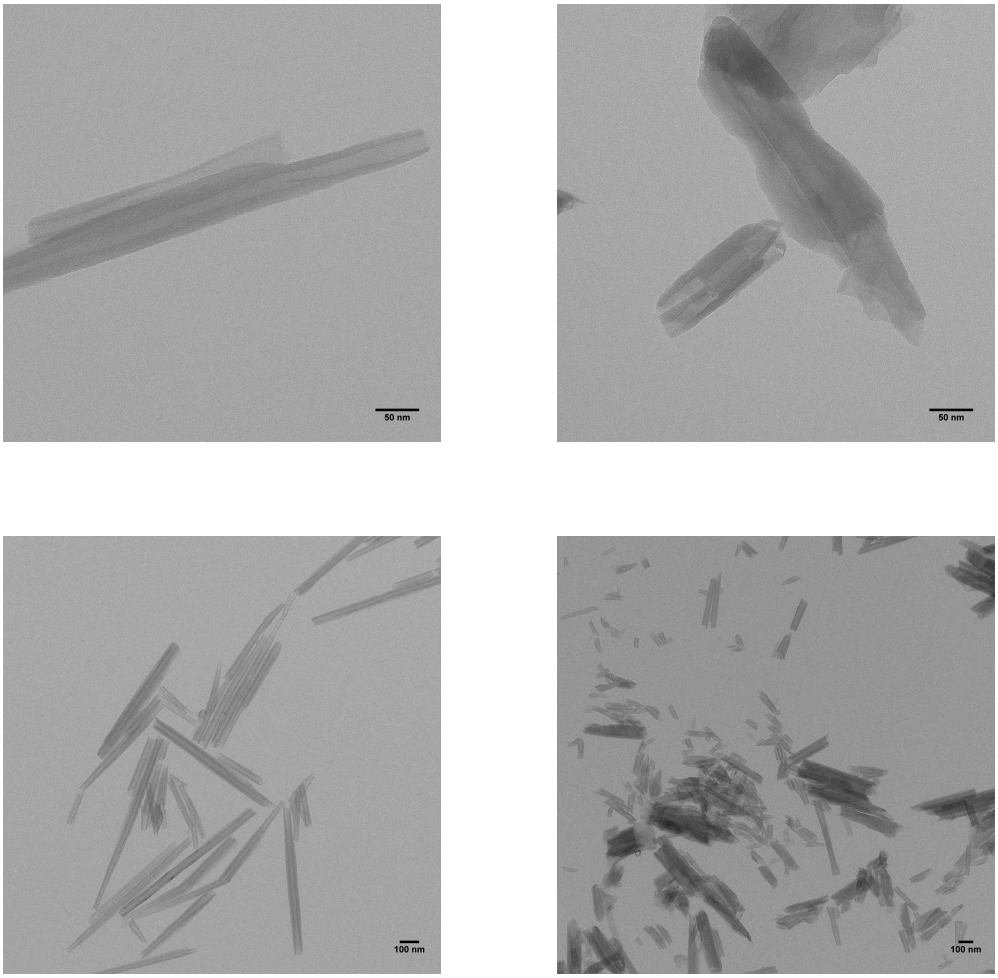

Figure 6.1: TEM images of HNTs mined from a Chinese mine (left) and an American mine (right).

6.2.2 Orientation of HNTs on Solid Substrates

The alignment of HNTs depends on the interactions between HNTs and the substrate as well as on the conditions during spraying. Two different substrates were investigated: Silicon wafers spin coated with a PEI layer and silicon substrates dip coated with two double layers of PSS/PDADMAC. Figure 6.3 shows AFM images of different substrates which are covered with HNTs, sprayed under same conditions. The coverage of PEI coated substrates is lower than of PSS/PDADMAC PEM coated substrates. During further procedure, it was shown that adhesion between PEMs and HNTs is too strong for alignment on the surface because HNTs strongly stick to the surface and an alignment is not observed. Therefore, experiments were carried out on PEI coated substrates.

Subsequently, the influence of different spraying parameters on the orientation of HNTs was investigated, namely spraying time (t), liquid flow rate (LF), gas flow rate (GF),

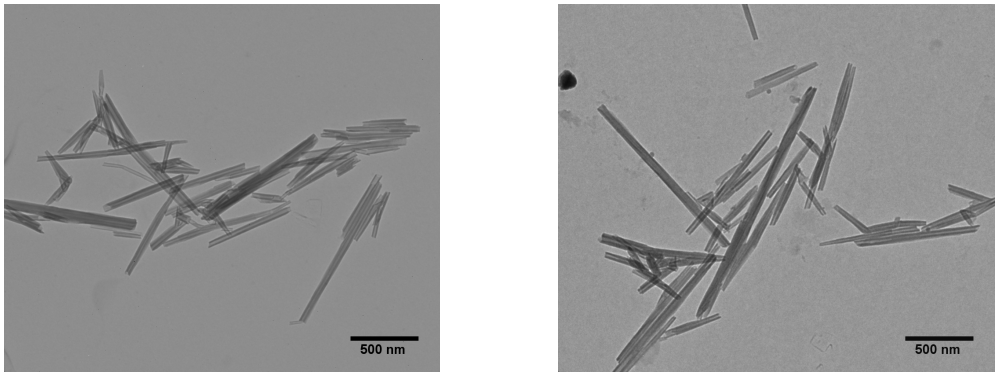

Figure 6.2: TEM images of pristine HNTs (left) and PSS loaded HNTs (right).

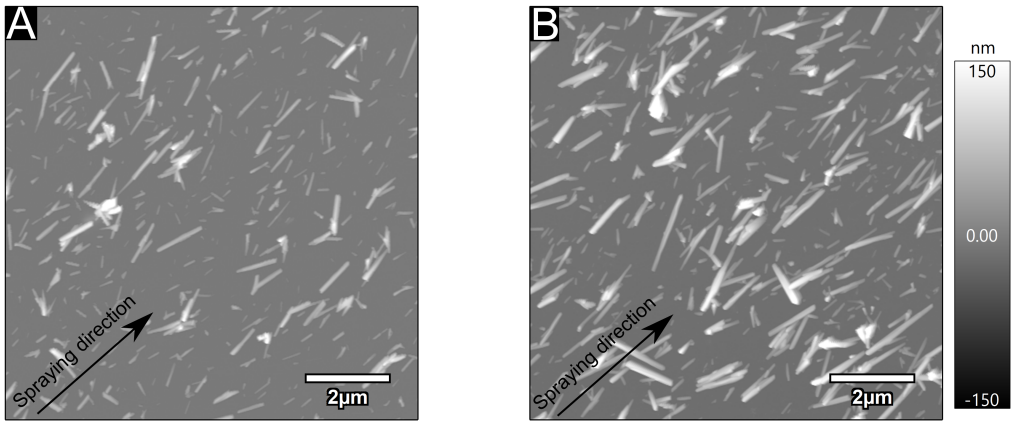

Figure 6.3: AFM images of HNTs spray coated on PEI (A) and $(PSS/PDADMAC)_2$ (B) with same spraying parameters (c: 0.1 g/L; LF: 5 mL/min; GF: 30 L/min; t: 200 s).

and concentration of the suspension (c). Figure 6.4 shows that the coverage increases by increasing the spraying time. A complete coverage of the substrate is not achieved. High coverage is already obtained after 200 s.

Figure 6.5 shows samples spray coated with different liquid flow rates. A sufficient low liquid flow rate is necessary for strongly oriented coatings. A liquid flow rate of 0.2 mL/min and lower does not lead to a liquid film on the surface and thus HNTs are randomly distributed on the surface (see Figure 6.5A). Figure 6.5B shows a orientation preferred in spraying direction from left to right. Figure 6.5C shows a worse orientation than Figure 6.5B. A liquid flow rate of 1 mL/min and higher does not lead to strong alignment. Figure 6.6 shows the influence of the gas flow rate. A higher gas flow rate leads to a higher coverage and stronger orientation. The maximum gas flow rate of the setup was 40 L/min and was used for strong orientation.

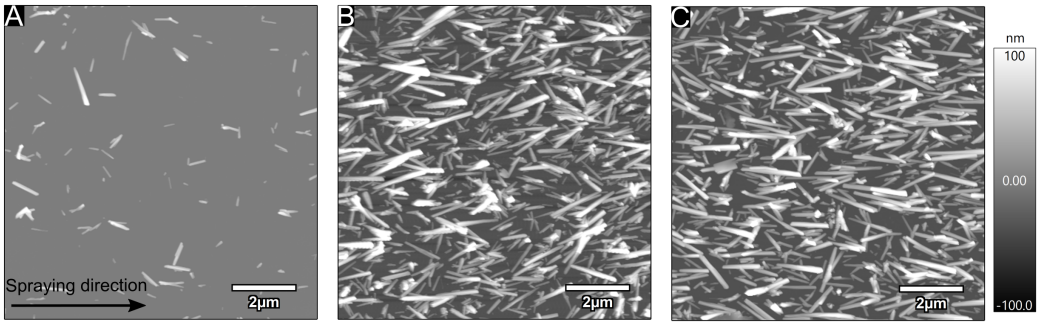

Figure 6.4: AFM images show the influence of the spraying time of three different samples: 10 s (A), 200 s (B), and 400 s (C) (c: 0.1 g/L; LF: 0.5 mL/min; GF: 30 L/min).

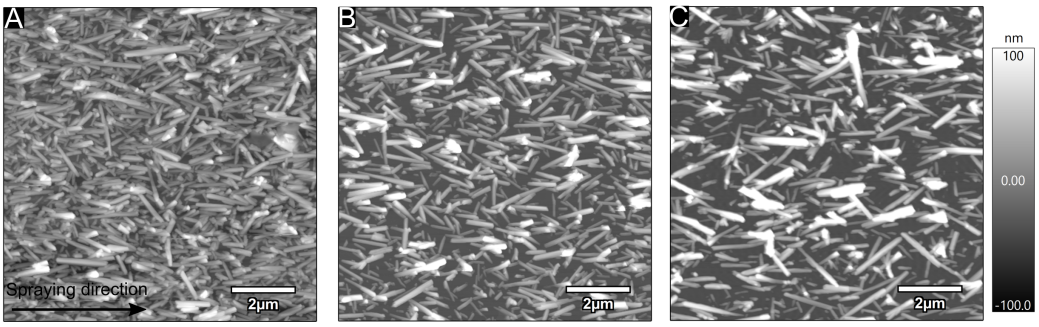

Figure 6.5: AFM images show the influence of three different liquid flow rate: 0.2 L/min (A), 0.5 L/min (B), and 1 L/min (C) (c: 0.1 g/L; GF: 40 L/min; time: 200 s).

Figure 6.7 shows the impact of the HNT concentration of the used suspension. Higher concentrations lead to higher coverage. The concentration could not be increased above 1 g/L with the used setup because the nozzle was blocked during spraying and the sedimentation velocity of the suspension increased. Figure 6.8 shows modified AFM images to highlight the angular distribution of HNTs at different points on the substrate. The orientation of the coating can be quantified by the nematic order parameter S_n (see Equation 2.5).[101] Random distribution leads to $S_n = 0$, while perfect alignment leads to $S_n = 1$. The resulting nematic order parameter S_n is increased up to 0.81. Strongest orientation is obtained beneath the impact point in the middle of the substrate. The order parameter decreases moving further away from this point.

The used spraying setup can produce more than one layer of HNTs. To build up a second layer, the first layer was dried and coated with PEI. Afterwards, the sample was coated with HNTs under same conditions again. Figure 6.9A shows a bilayer of HNT and

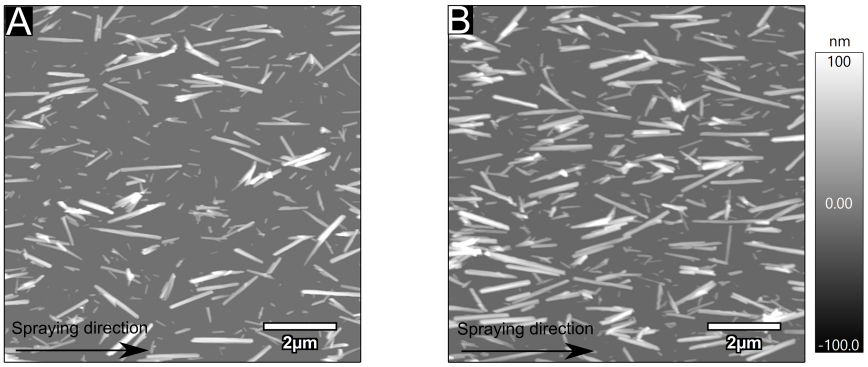

Figure 6.6: AFM images show the influence of two different gas flow rates of 20 L/min (A) and 40 L/min (B) (c: 0.5 g/L; LF: 0.5 mL/min; time: 200 s).

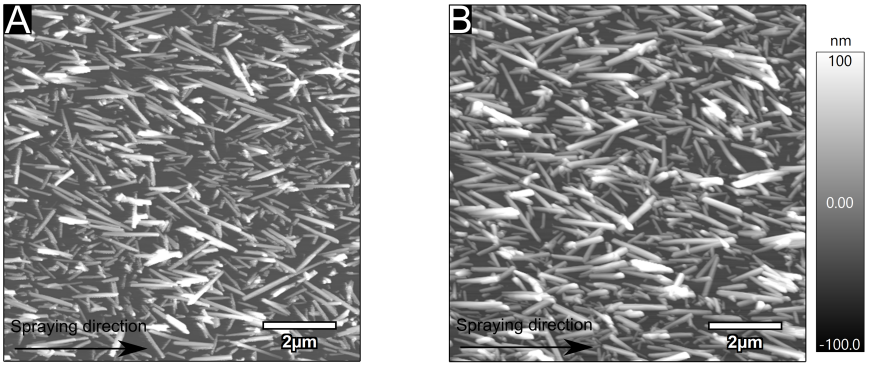

Figure 6.7: AFM images show the influence of two different concentration of 0.1 g/L (A) and 0.5 g/L (B) (LF: 0.5 mL/min; GF: 40 L/min; time: 200 s).

Figure 6.9B the corresponding colorized part of this image according to the orientation of HNTs. The substrate cannot be detected anymore and HNTs with different heights show that more than one layer is produced. A preferred orientation as well as the multiple layers of HNTs are visible. The colorized image underline preferential orientation in spraying direction. This mechanism is similar to the build-up of PEMs but the thickness per HNT layer is much larger.

AFM measurements were limited to scan areas of $20 \times 20\ \mu m^2$. Therefore, polarization microscopy was carried out to study the distribution over lager areas. Figure 6.10A-C show three images with different angles of the sample with respect to the polarizer and three corresponding images of an uncoated silicon wafer (Figure 6.10D-F). The analyzer was set to 90°. HNTs are well distributed over the entire area and a preferential direction is visible by eye although the diameter of HNTs are smaller than the resolution limit. Figure 6.11 shows the mean grey value as a function of the angle between polarizer and

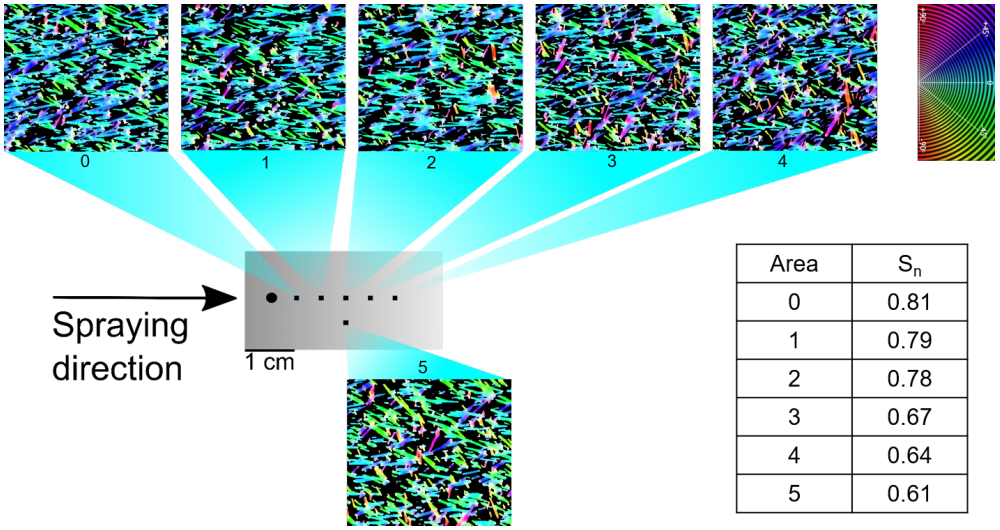

Area	S_n
0	0.81
1	0.79
2	0.78
3	0.67
4	0.64
5	0.61

Figure 6.8: Evaluation of the nematic order parameter S_n for different areas of the sample (c: 0.1 g/L LF: 0.5 mL/min GF: 40 L/min time: 200 s). Measured areas are shown larger for better visibility.

sample. A maximum is reached at 45° and a minimum is obtained either by parallel or perpendicular orientation to the polarizer.

6.3 Discussion

Halloysite nanotubes differ greatly in size and shape depending on the mine. Additionally, treatments after mining, e.g., milling, sieving, sonification, or chemical treatment, affect shape and chemical composition. Unfortunately, these treatments are mostly company secrets and are not accessible for HNTs used in this study. HNTs obtained from two different mines differs in shape and size distribution but the electrophoretic mobility of the particles stays constant. Depending on the purpose, it is possible to choose desired HNTs. Spraying experiments were carried out with Chinese Halloysites because a high aspect ratio favors a better alignment on the surface.

HNTs are semi-stable in suspension. Sedimentation is observed after several hours. HNTs have two different axes, namely the length and the diameter. Among others, colloidal stability depends on the dimensions of the dispersed particles. In general, colloidal stable domains are in the range of some nm up to 1 micron. They stay dispersed in the surrounding medium because the repulsion of the single domains avoids sedimentation and agglomeration. This can be achieved either by electrostatic or steric stabilization. The diameter of HNTs is some tens of nm and thus in the range of colloidal domains. In contrast, the length of HNTs varies considerably between some hundreds of nanometer up to several microns. Therefore, longer HNTs sediment while shorter HNTs are colloidal stable. This can be used for size separation.

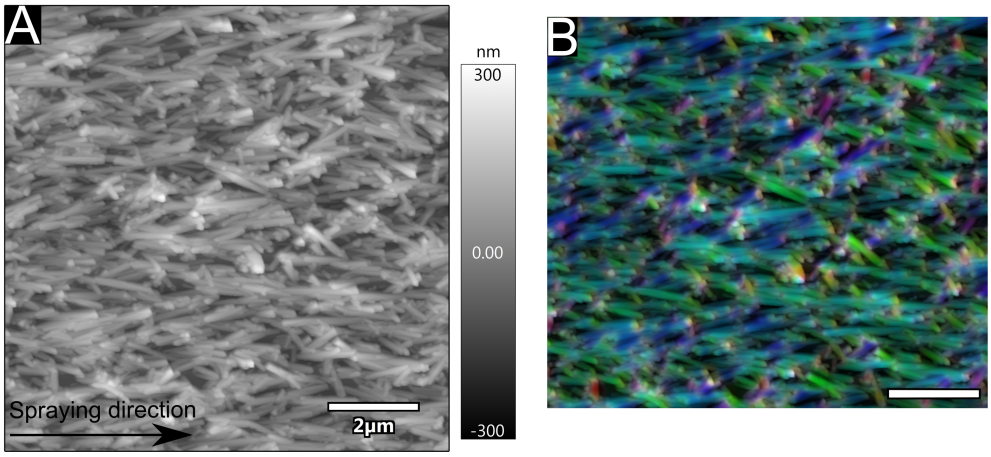

Figure 6.9: AFM image of $(PEI/HNT)_2$) (A) and the respective evaluated part of this image colorized according to the orientation (B) (c: 0.1 g/L; LF: 0.2 mL/min; GF: 40 L/min; time: 200 s).

HNTs were loaded with PSS which should lead to a better colloidal stability.[81,80] This was not confirmed in this study. In general, the colloidal stability of HNTs can be tuned by affecting the electrostatic repulsion and van-der-Waals attraction. Thus, higher charged particles should lead to a more stable suspension. The overall particle charge is a superposition of the inner and outer surface charge. Due to the positively charged inner and negatively charged outer surfaces of the HNT, it is possible to load them with negatively charged PEs. Additionally, an adsorption of negatively charged PEs on the outer surface should lead to a higher net charge and a further repulsion. The dominant adsorption process is not yet clear. An adsorption on the inner and/or outer surface is possible. The adsorption on the outer surface was shown for silica particles and negatively charged long chain olefins.[155] HNTs were size selected to get rid of agglomerates. After a sedimentation time of 1 h large agglomerates sediment and the supernatant was collected and centrifuged (see Section 3.2.6). Now, short HNTs stay dispersed while longer HNTs sediment. The sediment is collected and redispersed by mixing with water and a short sonification cycle.

Spraying experiments were carried out with loaded HNTs to ensure that suspensions stay stable during the spraying, to increase the electrostatic attraction to the positively charged substrate, and to be able to compare the results with Zhao *et al.*[80] Additionally, the particles should stronger repel each other so that they do not agglomerate on the surface.

Interaction between the surface and HNTs as well as spraying parameters are of crucial importance. On the one hand, a strong HNT-substrate interaction leads to a sticking of the particles without a preferential orientation. On the other hand, a weak interaction leads to rinsing particles off the substrate. The interaction between PSS loaded HNTs and

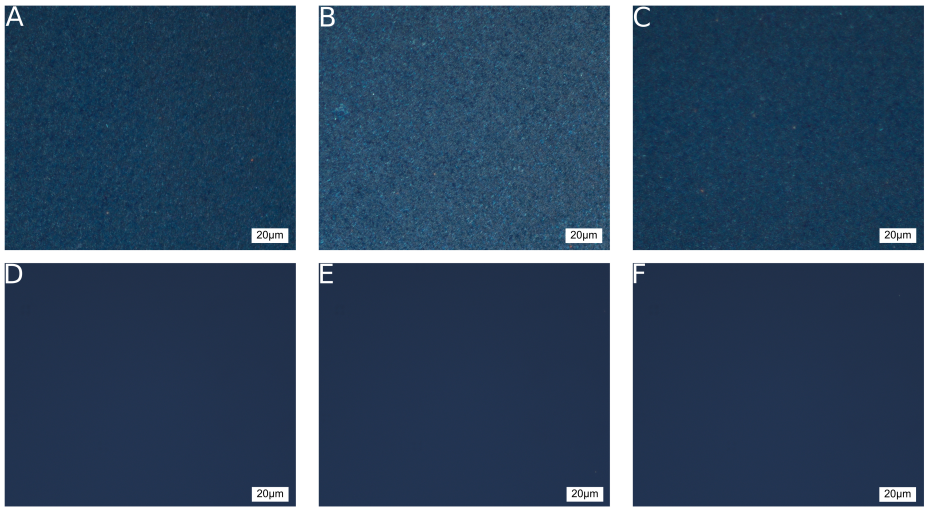

Figure 6.10: Polarization microscopy images. From left to right the angle of the sample with respect to the polarizer is 0° (A), 45° (B), and 90° (C) (c: 0.2 g/L; LF: 0.5 mL/min; GF: 40 L/min; time: 200s). D-F: Respective images of an uncoated silicon wafer.

PEI is lower than the interaction between PSS loaded HNTs and a PEM with PDADMAC as the outermost layer. Nevertheless, the interaction with PEI is sufficient for orientation of HNTs. The electrostatic interaction is stronger between PDADMAC and HNTs than between PEI and HNTs because PDADMAC is a permanently positive charged polyelectrolyte while PEI is not fully charged at intermediate pH. For further experiments PEI was used as a substrate because it was shown that the orientation occurs due to an interplay between the liquid flow on the surface and the HNTs adsorption at the surface. Therefore, a strong interaction does not favor an orientation because particles stick to the surface immediately after impact and do not align.

Besides the interaction with the substrate, the alignment is strongly dependent on the spraying parameters. A spraying time of 200 s is sufficient to obtain high coverage. Longer spraying time does not lead to higher coverage because HNTs do not build-up multilayer due to electrostatic repulsion. While increasing the liquid flow rate, the orientation decreases and more agglomerates are visible. Misalignment could be a result of high pressure and shear forces at the tip of the nozzle and thus higher turbulence while droplets move to the surface. In contrast, an insufficient liquid flow rate is not able to develop a liquid film on the surface and thus, a random distribution is observed. Higher gas flow rate leads to a higher coverage and stronger alignment. This may occur due to a faster evaporation of the liquid and higher velocity of the liquid film on the surface. Hence, more particles remain on the surface. An increase of the concentration leads to a higher coverage on the surface. This is a result of a larger amount of HNTs per sprayed volume. Based on these findings, a strong alignment occurs by using sufficient

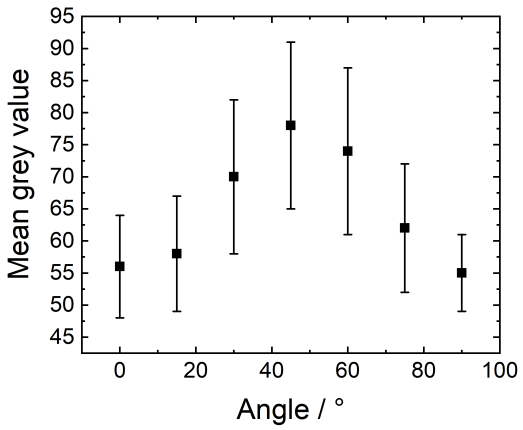

Figure 6.11: Mean grey value of polarization microscopy images as a function of angle in respect to the polarizer in crossed polarizer setup. (c: 0.2 g/L; LF: 0.5 mL/min; GF: 40 L/min; time: 200 s.)

long spraying time, low liquid flow rate, high gas flow rate, and a concentration as high as possible. The velocity and amount of liquid decreases with increasing distance to the impact point. This causes a decrease of the nematic order parameter. HNTs may stick less aligned to the surface with larger distance from the impact point because a directed flow is not ensured and the liquid is partly evaporated. Polarization microscopy was used to prove the homogeneity of these coatings. The images show that homogeneous orientation is preserved over more than 150 μm. Furthermore, bilayers can be produced with an interlayer of oppositely charged PEI.

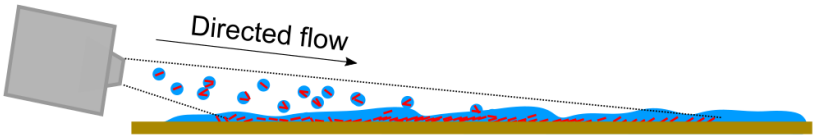

Figure 6.12: Scheme of shear alignment. The suspension is vaporized during spraying and a liquid flow occurs on the surface leading to an orientation of the adsorbed HNTs.

Blell *et al.* suggested that orientation occurs due to shear alignment on the surface.[103] The same principal is suggest for this study. Figure 6.12 shows the mechanism during spraying. The liquid is vaporized at the nozzle and the droplets move to the surface. After impact, a thin liquid film is produced. The liquid is moved away from the impact point on the surface and the particles align due to the liquid flow on the surface.

6.4 Conclusion

HNTs are a versatile, natural material. HNTs are negatively charged at intermediate pH and partially stabilized in colloidal suspensions. The different surface properties allow a selective modification of the inner and outer surface. HNTs, suspended in water, can be sprayed on positively charged surfaces. PEI coated silicon wafer show stronger aligned HNTs than wafers coated with PSS/PDADMAC PEMs. The orientation is influenced by different spraying parameters. A spraying time of 200 s is sufficient for highly covered substrates. A low liquid and a high gas flow rate favor alignment. Increasing concentration of the suspension leads to higher coverage but is limited due to blocking of the nozzle. Furthermore, bilayers of PEI and HNTs are produced by consecutive adsorption.

It is possible to align HNTs on a surface and to influence the ordering and coverage. Therefore, HNTs are promising building blocks to introduce anisotropy to thin surface coatings. They can be used as a substrate, e.g. for directional cell growth or for hierarchical structures including mutual interaction with other HNTs and/or other components.

7 Conclusion and Outlook

This thesis gives an insight into thin coating consisting of different components. It focuses on the internal composition of polyelectrolyte multilayers and their combination with polyelectrolyte brushes. Furthermore, HNTs combined with polyelectrolytes are used to obtain anisotropic coatings.

Responsive Polyelectrolyte Coatings The first part of this thesis deals with different polyelectrolyte coatings. Polyelectrolyte multilayers (PEMs) are a well-understood and easy approach to coat charged surfaces. Different combinations of polyelectrolytes and preparation protocols open a large variety of coatings. Additionally, most PEMs are responsive to outer stimuli, e.g., humidity, temperature, and/or salt concentration. PSS/PDADMAC PEMs form a polymer network with included voids rather than a compact polymer layer. Therefore, the question arises how tight PEMs are packed and how the voids get filled with water by increasing humidity. Chapter 4 shows that ellipsometry is a suitable method to investigate those thin coatings. Increasing humidity leads to PEM swelling and replacement of air by water inside the voids. It is possible to calculate the amount of voids and to get knowledge about how air is replaced by water with increasing relative humidity. Data were evaluated with a self-written Python program based on the *extended void model*. This study reveals a gradual replacement of air with water in the voids up to 30% RH. Above 30% RH the voids are completely filled with water and further water uptake leads only to further swelling of the entire PEM.

Combinations of PEMs and polyelectrolyte brushes even extend possibilities of smart coatings due to their different architectures. Covalently bound brushes to a solid surface can be used as a substrate for PEMs. The internal composition of PEM coated brushes was studied in Chapter 5. Polymer brushes and PEMs have similar refractive indices. Therefore, ellipsometry is not suitable to investigate the internal structure and can only give information about the swelling behavior of the entire composite. Neutron reflectometry opens the possibility to generate a contrast between different parts of the composite. The measurements show that brushes and PEMs interdigitate strongly. The composite retains its responsiveness to the environmental humidity as the single components. A self-written fitting procedure, based on the procedure developed by Schneck *et al.*, was used to simultaneously interpret the data including mass conservation over the entire humidity range. Increasing the relative humidity leads to swelling of the composite and separation of the single components. Water accumulates in the transition region. The swelling process is almost reversible.

Coatings Based on Halloysite Nanotubes Chapter 6 deals with Halloysite nanotubes (HNTs). Especially, the focus was drawn on the orientation of HNTs on a surface to

obtain anisotropic coatings. HNTs are semi-stable in suspension but offer a sufficient stability to carry out spraying experiments. HNTs were sprayed on a silicon wafer precoated with polyelectrolytes. It was shown that HNTs adsorb on PEI coated substrates as well as on PSS/PDADMAC PEMs. The interaction with the substrate is of crucial importance for alignment. The interaction of HNTs and PEI showed a good balance between adsorption and desorption for the alignment on the surface. Furthermore, the influence of different parameters was investigated during spray deposition, namely spraying time, concentration, liquid flow rate, and gas flow rate. Atomic force microscopy and polarized microscopy were used to study the orientation of HNTs. It was shown that low liquid and high gas flow lead to strong orientation. Increasing the spraying time and concentration lead to a higher coverage. Additionally, it was shown that bilayers of HNTs are produced when using an interlayer of PEI.

This work gave an insight into the composition of PEMs and composites of PEMs and brushes. The results show that they are promising candidates for thin, responsive coatings. The *extended void model* is transferable to all other PEMs and opens the possibility to determine the PEM's composition. With that, it is possible to precisely tailor PEMs for specific applications. As open questions remain the distribution and shape of the voids. Since PEMs are very flexible and swell with increasing humidity, a determination of pore sizes with adsorption measurements is not possible. Therefore, other techniques are necessary like a local sensitive tomography method with a smaller scan volume than commercially available. Knowledge about shape and size opens the possibility to tailor PEMs as carrier system with suited pockets for sensitive molecules.

PEMs, brushes, and a combination of both could be part of different future applications. On the one hand, they can be used to avoid or favor adsorption of specific molecules, e.g., on hulls, contact lenses, pills, buildings or cars. PEMs can be used as a mediator for medical applications to avoid unwanted side effects or as a matrix for sensors. On the other hand, an incorporation and controlled release of small molecules could be a future field of application. For technical applications, the longtime stability is one of the major aspect which was not part of the study. Here, the focus was drawn to understand the internal composition and show fundamental proof of principal. Nevertheless, tailoring a coatings for technical applications should also include stability tests. Thus, these composites can act as a suitable matrix to embed molecules. Additionally, the composites can be used as carrier and protective systems for sensitive molecules. The release of small guest molecules can then be triggered by swelling and deswelling.

Furthermore, the alignment of HNTs on a surface was shown. An oriented embedding into a polymer matrix opens the possibility to introduce anisotropy and versatile containers into thin coatings. Anisotropic layers open the possibility for different applications. An oriented cell growth, new optical properties, or weight reduction of existing coatings are possible applications. Furthermore, aligned HNTs can be used as nanocontainers for active molecules which can be released under controlled conditions. This can be used to prevent corrosion or cell degradation. The possibility to produce multilayers could be another approach. On the one hand, different layers can be oriented in same direction. With that, layers can be produced with thickness dependent anisotropy. On the other

hand, different orientation of consecutive layers can lead to chiral properties or an increased mechanical robustness of the coating. Those structures are already reported for natural materials. Therefore, mimic natural structures can be a field for further experiments based on HNTs coatings. So far, the spray mechanism and the reason of orientation are still an open question. First hints leads to the conclusion that the alignment takes place due to shear alignment on the surface. Further investigations of the entire procedure are necessary. Starting with the study of size and velocity of the droplets, e.g. with the help of a phase Doppler interferometer. Furthermore, the liquid flow on the surface could help to clarify the mechanism of particle alignment. In situ tracking of particles could be a possibility to investigate HNTs coated with a fluorescent dye by a microscope beneath glass substrates.

All in all, this work shows that surface coating are still an interesting field of research with different possibilities for future applications. The knowledge of precise tailoring and of the internal structure is of crucial importance and allows the design of coatings for specific applications like sensors, carrier systems or protective coatings.

Bibliography

[1] Decher, G.; Hong, J.; Schmitt, J. Buildup of Ultrathin Multilayer Films by a Self-Assembly Process: III. Consecutively Alternating Adsorption of Anionic and Cationic Polyelectrolytes on Charged Surfaces. *Thin Solid Films* **1992**, *210 - 211*, 831 – 835.

[2] Decher, G. Fuzzy Nanoassemblies: Toward Layered Polymeric Multicomposites. *Science* **1997**, *277*, 1232 – 1237.

[3] Dubas, S. T.; Iamsamai, C.; Potiyaraj, P. Optical Alcohol Sensor Based on Dye-Chitosan Polyelectrolyte Multilayers. *Sensors and Actuators B: Chemical* **2006**, *113*, 370 – 375.

[4] Zhu, X.; Jańczewski, D.; Lee, S. S. C.; Teo, S. L.-M.; Vancso, G. J. Cross-Linked Polyelectrolyte Multilayers for Marine Antifouling Applications. *ACS Applied Materials & Interfaces* **2013**, *5*, 5961 – 5968.

[5] Hiller, J.; Mendelsohn, J. D.; Rubner, M. F. Reversibly Erasable Nanoporous Anti-Reflection Coatings from Polyelectrolyte Multilayers. *Nature Materials* **2002**, *1*, 59 – 63.

[6] Schrinner, M.; Proch, S.; Mei, Y.; Kempe, R.; Miyajima, N.; Ballauff, M. Stable Bimetallic Gold-Platinum Nanoparticles Immobilized on Spherical Polyelectrolyte Brushes: Synthesis, Characterization, and Application for the Oxidation of Alcohols. *Advanced Materials* **2008**, *20*, 1928 – 1933.

[7] Andrieu-Brunsen, A.; Micoureau, S.; Tagliazucchi, M.; Szleifer, I.; Azzaroni, O.; Soler-Illia, G. J. Mesoporous Hybrid Thin Film Membranes with PMETAC@ Silica Architectures: Controlling Ionic Gating through the Tuning of Polyelectrolyte Density. *Chemistry of Materials* **2015**, *27*, 808 – 821.

[8] Azzaroni, O.; Brown, A.; Huck, W. Tunable Wettability by Clicking Counterions into Polyelectrolyte Brushes. *Advanced Materials* **2006**, *19*, 151 – 154.

[9] Jain, P.; Dai, J.; Grajales, S.; Saha, S.; Baker, G. L.; Bruening, M. L. Completely Aqueous Procedure for the Growth of Polymer Brushes on Polymeric Substrates. *Langmuir* **2007**, *23*, 11360 – 11365.

[10] Micciulla, S.; Soltwedel, O.; Löhmann, O.; von Klitzing, R. Temperature Responsive Behavior of Polymer Brush/Polyelectrolyte Multilayer Composites. *Soft Matter* **2016**, *12*, 1176 – 1183.

[11] Veerabadran, N. G.; Mongayt, D.; Torchilin, V.; Price, R. R.; Lvov, Y. M. Organized Shells on Clay Nanotubes for Controlled Release of Macromolecules. *Macromolecular Rapid Communications* **2009**, *30*, 99 – 103.

[12] van der Gucht, J.; Spruijt, E.; Lemmers, M.; Stuart, M. A. C. Polyelectrolyte Complexes: Bulk Phases and Colloidal Systems. *Journal of Colloid and Interface Science* **2011**, *361*, 407 – 422.

[13] Das, B. P.; Tsianou, M. From Polyelectrolyte Complexes to Polyelectrolyte Multilayers: Electrostatic Assembly, Nanostructure, Dynamics, and Functional Properties. *Advances in Colloid and Interface Science* **2017**, *244*, 71 – 89.

[14] Ou, Z.; Muthukumar, M. Entropy and Enthalpy of Polyelectrolyte Complexation: Langevin Dynamics Simulations. *The Journal of Chemical Physics* **2006**, *124*, 154902.

[15] Salomäki, M.; Tervasmäki, P.; Areva, S.; Kankare, J. The Hofmeister Anion Effect and the Growth of Polyelectrolyte Multilayers. *Langmuir* **2004**, *20*, 3679 – 3683.

[16] Leontidis, E. Hofmeister Anion Effects on Surfactant Self-assembly and the Formation of Mesoporous Solids. *Current Opinion in Colloid & Interface Science* **2002**, *7*, 81 – 91.

[17] Dubas, S. T.; Schlenoff, J. B. Factors Controlling the Growth of Polyelectrolyte Multilayers. *Macromolecules* **1999**, *32*, 8153 – 8160.

[18] Stubenrauch, C.; Albouy, P.-A.; von Klitzing, R.; Langevin, D. Polymer/Surfactant Complexes at the Water/Air Interface: A Surface Tension and X-ray Reflectivity Study. *Langmuir* **2000**, *16*, 3206 – 3213.

[19] Dautzenberg, H.; Görnitz, E.; Jaeger, W. Synthesis and Characterization of Poly(diallyldimethylammonium chloride) in a Broad Range of Molecular Weight. *Macromolecular Chemistry and Physics* **1998**, *199*, 1561 – 1571.

[20] Micciulla, S.; Dodoo, S.; Chevigny, C.; Laschewsky, A.; von Klitzing, R. Short *versus* Long Chain Polyelectrolyte Multilayers: A Direct Comparison of Self-Assembly and Structural Properties. *Physical Chemistry Chemical Physics* **2014**, *16*, 21988.

[21] Volodkin, D. V.; Petrov, A. I.; Prevot, M.; Sukhorukov, G. B. Matrix Polyelectrolyte Microcapsules: New System for Macromolecule Encapsulation. *Langmuir* **2004**, *20*, 3398 – 3406.

[22] Zhu, Y.; Shi, J.; Shen, W.; Dong, X.; Feng, J.; Ruan, M.; Li, Y. Stimuli-Responsive Controlled Drug Release from a Hollow Mesoporous Silica Sphere/Polyelectrolyte Multilayer Core-Shell Structure. *Angewandte Chemie* **2005**, *117*, 5213 – 5217.

[23] Adamczyk, Z.; Zembala, M.; Kolasińska, M.; Warszyński, P. Characterization of Polyelectrolyte Multilayers on Mica and Oxidized Titanium by Streaming Potential

and Wetting Angle Measurements. *Colloids and Surfaces A: Physicochemical and Engineering Aspects* **2007**, *302*, 455 – 460.

[24] Zhang, H.; Rühe, J. Interaction of Strong Polyelectrolytes with Surface-Attached Polyelectrolyte Brushes-Polymer Brushes as Substrates for the Layer-by-Layer Deposition of Polyelectrolytes. *Macromolecules* **2003**, *36*, 6593 – 6598.

[25] Chiarelli, P. A.; Johal, M. S.; Casson, J. L.; Roberts, J. B.; Robinson, J. M.; Wang, H.-L. Controlled Fabrication of Polyelectrolyte Multilayer Thin Films Using Spin-Assembly. *Advanced Materials* **2001**, *13*, 1167 – 1171.

[26] Schlenoff, J. B.; Dubas, S. T.; Farhat, T. Sprayed Polyelectrolyte Multilayers. *Langmuir* **2000**, *16*, 9968 – 9969.

[27] Kovacevic, D.; van der Burgh, S.; de Keizer, A.; Cohen Stuart, M. A. Kinetics of Formation and Dissolution of Weak Polyelectrolyte Multilayers: Role of Salt and Free Polyions. *Langmuir* **2002**, *18*, 5607 – 5612.

[28] von Klitzing, R. Internal Structure of Polyelectrolyte Multilayer Assemblies. *Physical Chemistry Chemical Physics* **2006**, *8*, 5012 – 5033.

[29] Borges, J.; Mano, J. F. Molecular Interactions Driving the Layer-by-Layer Assembly of Multilayers. *Chemical Reviews* **2014**, *114*, 8883 – 8942.

[30] Porcel, C.; Lavalle, P.; Ball, V.; Decher, G.; Senger, B.; Voegel, J.-C.; Schaaf, P. From Exponential to Linear Growth in Polyelectrolyte Multilayers. *Langmuir* **2006**, *22*, 4376 – 4383.

[31] Ladam, G.; Schaad, P.; Voegel, J. C.; Schaaf, P.; Decher, G.; Cuisinier, F. In Situ Determination of the Structural Properties of Initially Deposited Polyelectrolyte Multilayers. *Langmuir* **2000**, *16*, 1249 – 1255.

[32] Ghostine, R. A.; Markarian, M. Z.; Schlenoff, J. B. Asymmetric Growth in Polyelectrolyte Multilayers. *Journal of the American Chemical Society* **2013**, *135*, 7636 – 7646.

[33] Schmitt, J.; Gruenewald, T.; Decher, G.; Pershan, P. S.; Kjaer, K.; Loesche, M. Internal Structure of Layer-by-Layer Adsorbed Polyelectrolyte Films: A Neutron and X-Ray Reflectivity Study. *Macromolecules* **1993**, *26*, 7058 – 7063.

[34] Steitz, R.; Leiner, V.; Tauer, K.; Khrenov, V.; von Klitzing, R. Temperature-Induced Changes in Polyelectrolyte Films at the Solid-Liquid Interface. *Applied Physics A* **2002**, *74*, 519 – 521.

[35] Jaber, J. A.; Schlenoff, J. B. Polyelectrolyte Multilayers with Reversible Thermal Responsivity. *Macromolecules* **2005**, *38*, 1300 – 1306.

[36] Kügler, R.; Schmitt, J.; Knoll, W. The Swelling Behavior of Polyelectrolyte Multilayers in Air of Different Relative Humidity and in Water. *Macromolecular Chemistry and Physics* **2002**, *203*, 413 – 419.

[37] Wong, J.; Rehfeldt, F.; Hanni, P.; Tanaka, M.; von Klitzing, R. Swelling Behavior of Polyelectrolyte Multilayers in Saturated Water Vapor. *Macromolecules* **2004**, *37*, 7285–7289.

[38] De, S.; Cramer, C.; Schönhoff, M. Humidity Dependence of the Ionic Conductivity of Polyelectrolyte Complexes. *Macromolecules* **2011**, *44*, 8936 – 8943.

[39] Sukhishvili, S. A.; Granick, S. Layered, Erasable, Ultrathin Polymer Films. *Journal of the American Chemical Society* **2000**, *122*, 9550 – 9551.

[40] Dodoo, S.; Steitz, R.; Laschewsky, A.; von Klitzing, R. Effect of Ionic Strength and Type of Ions on the Structure of Water Swollen Polyelectrolyte Multilayers. *Physical Chemistry Chemical Physics* **2011**, *13*, 10318 – 10325.

[41] Borges, J.; Rodrigues, L. C.; Reis, R. L.; Mano, J. F. Layer-by-Layer Assembly of Light-Responsive Polymeric Multilayer Systems. *Advanced Functional Materials* **2014**, *24*, 5624 – 5648.

[42] Zhao, X.; Ma, K.; Jiao, T.; Xing, R.; Ma, X.; Hu, J.; Huang, H.; Zhang, L.; Yan, X. Fabrication of Hierarchical Layer-by-Layer Assembled Diamondbased Core-Shell Nanocomposites as Highly Efficient Dye Absorbents for Wastewater Treatment. *Scientific Reports* **2017**, *7*.

[43] Li, B. L.; Setyawati, M. I.; Chen, L.; Xie, J.; Ariga, K.; Lim, C.-T.; Garaj, S.; Leong, D. T. Directing Assembly and Disassembly of 2D MoS_2 Nanosheets with DNA for Drug Delivery. *ACS Applied Materials & Interfaces* **2017**, *9*, 15286 – 15296.

[44] Ruttala, H. B.; Ramasamy, T.; Shin, B. S.; Choi, H.-G.; Yong, C. S.; Kim, J. O. Layer-by-layer Assembly of Hierarchical Nanoarchitectures to Enhance the Systemic Performance of Nanoparticle Albumin-Bound Paclitaxel. *International Journal of Pharmaceutics* **2017**, *519*, 11 – 21.

[45] Hossfeld, S.; Nolte, A.; Hartmann, H.; Recke, M.; Schaller, M.; Walker, T.; Kjems, J.; Schlosshauer, B.; Stoll, D.; Wendel, H.-P.; Krastev, R. Bioactive Coronary Stent Coating Based on Layer-by-Layer Technology for SiRNA Release. *Acta Biomaterialia* **2013**, *9*, 6741 – 6752.

[46] Salloum, D. S.; Olenych, S. G.; Keller, T. C. S.; Schlenoff, J. B. Vascular Smooth Muscle Cells on Polyelectrolyte Multilayers: Hydrophobicity-Directed Adhesion and Growth. *Biomacromolecules* **2005**, *6*, 161 – 167.

[47] Köhler, R.; Steitz, R.; von Klitzing, R. About Different Types of Water in Swollen Polyelectrolyte Multilayers. *Advances in Colloid and Interface Science* **2014**, *207*, 325 – 331.

[48] Köhler, R.; Dönch, I.; Ott, P.; Laschewsky, A.; Fery, A.; Krastev, R. Neutron Reflectometry Study of Swelling of Polyelectrolyte Multilayers in Water Vapors: Influence of Charge Density of the Polycation. *Langmuir* **2009**, *25*, 11576 – 11585, PMID: 19788217.

[49] Zerball, M.; Laschewsky, A.; von Klitzing, R. Swelling of Polyelectrolyte Multilayers: The Relation Between, Surface and Bulk Characteristics. *The Journal of Physical Chemistry B* **2015**, *119*, 11879 – 11886.

[50] Garnett, J. Colours in Metal Glasses and in Metallic Films. *Philosophical Transactions of the Royal Society of London* **1904**, *203*, 385–420.

[51] Garnett, J. Colours in Metal Glasses, in Metallic Films and in Metallic Solutions. II. *Philosophical Transactions of the Royal Society of London* **1905**, *205*, 237 – 288.

[52] Tanchak, O. M.; Yager, K. G.; Fritzsche, H.; Harroun, T.; Katsaras, J.; Barrett, C. J. Water Distribution in Multilayers of Weak Polyelectrolytes. *Langmuir* **2006**, *22*, 5137 – 5143.

[53] Dodoo, S.; Balzer, B. N.; Hugel, T.; Laschewsky, A.; Klitzing, R. v. Effect of Ionic Strength and Layer Number on Swelling of Polyelectrolyte Multilayers in Water Vapour. *Soft Materials* **2013**, *11*, 157 – 164.

[54] Nazaran, P.; Bosio, V.; Jaeger, W.; Anghel, D. F.; von Klitzing, R. Lateral Mobility of Polyelectrolyte Chains in Multilayers. *Journal of Physical Chemistry B* **2007**, *111*, 8572 – 8581.

[55] Iturri Ramos, J. J.; Stahl, S.; Richter, R. P.; Moya, S. E. Water Content and Buildup of Poly(diallyldimethylammonium chloride)/Poly(sodium 4-styrenesulfonate) and Poly(allylamine hydrochloride)/Poly(sodium 4-styrenesulfonate) Polyelectrolyte Multilayers Studied by an in Situ Combination of a Quartz Crystal Microbalance with Dissipation Monitoring and Spectroscopic Ellipsometry. *Macromolecules* **2010**, *43*, 9063 – 9070.

[56] Jin, Y.; He, Z.; Guo, Q.; Wang, J. Control of Ice Propagation by Using Polyelectrolyte Multilayer Coatings. *Angewandte Chemie International Edition* **2017**, *56*, 11436 – 11439.

[57] Li, W.; Gai, M.; Frueh, J.; Kudryavtseva, V. L.; Sukhorukov, G. B. Polyelectrolyte Multilayer Microchamber-Arrays for in-Situ Cargo Release: Low Frequency vs. Medical Frequency Range Ultrasound. *Colloids and Surfaces A: Physicochemical and Engineering Aspects* **2018**, *547*, 19 – 27.

[58] Zhao, B.; Brittain, W. Polymer Brushes: Surface-Immobilized Macromolecules. *Progress in Polymer Science* **2000**, *25*, 677 – 710.

[59] Koutsos, V.; van der Vegte, E. W.; Hadziioannou, G. Direct View of Structural Regimes of End-Grafted Polymer Monolayers: A Scanning Force Microscopy Study. *Macromolecules* **1999**, *32*, 1233 – 1236.

[60] Ejaz, M.; Yamamoto, S.; Ohno, K.; Tsujii, Y.; Fukuda, T. Controlled Graft Polymerization of Methyl Methacrylate on Silicon Substrate by the Combined Use of the Langmuir-Blodgett and Atom Transfer Radical Polymerization Techniques. *Macromolecules* **1998**, *31*, 5934–5936.

[61] Barbey, R.; Lavanant, L.; Paripovic, D.; Schüwer, N.; Sugnaux, C.; Tugulu, S.; Klok, H.-A. Polymer Brushes via Surface-Initiated Controlled Radical Polymerization: Synthesis, Characterization, Properties, and Applications. *Chemical Reviews* **2009**, *109*, 5437 – 5527.

[62] Biesalski, M.; Rühe, J. Scaling Laws for the Swelling of Neutral and Charged Polymer Brushes in Good Solvents. *Macromolecules* **2002**, *35*, 499 – 507.

[63] Sanjuan, S.; Tran, Y. Stimuli-Responsive Interfaces Using Random Polyampholyte Brushes. *Macromolecules* **2008**, *41*, 8721 – 8728.

[64] Wu, T.; Efimenko, K.; Genzer, J. Combinatorial Study of the Mushroom-to-Brush Crossover in Surface Anchored Polyacrylamide. *Journal of the American Chemical Society* **2002**, *124*, 9394 – 9395.

[65] Christau, S.; Möller, T.; Yenice, Z.; Genzer, J.; von Klitzing, R. Brush/Gold Nanoparticle Hybrids: Effect of Grafting Density on the Particle Uptake and Distribution within Weak Polyelectrolyte Brushes. *Langmuir* **2014**, *30*, 13033 – 13041.

[66] Kim, M.; Schmitt, S. K.; Choi, J. W.; Krutty, J. D.; Gopalan, P. From Self-Assembled Monolayers to Coatings: Advances in the Synthesis and Nanobio Applications of Polymer Brushes. *Polymers* **2015**, *7*, 1346 – 1378.

[67] Ignatova, M.; Voccia, S.; Gilbert, B.; Markova, N.; Mercuri, P. S.; Galleni, M.; Sciannamea, V.; Lenoir, S.; Cossement, D.; Gouttebaron, R.; Jérôme, R.; Jérôme, C. Synthesis of Copolymer Brushes Endowed with Adhesion to Stainless Steel Surfaces and Antibacterial Properties by Controlled Nitroxide-Mediated Radical Polymerization. *Langmuir* **2004**, *20*, 10718–10726.

[68] Otsu, T.; Ogawa, T.; Yamamoto, T. Solid-phase block copolymer synthesis by the iniferter technique. *Macromolecules* **1986**, *19*, 2087–2089.

[69] Wang, J.-S.; Matyjaszewski, K. Controlled/"Living" Radical Polymerization. Atom Transfer Radical Polymerization in the Presence of Transition-Metal Complexes. *Journal of the American Chemical Society* **1995**, *117*, 5614 – 5615.

[70] Cheng, N.; Azzaroni, O.; Moya, S.; Huck, W. T. S. The Effect of [CuI]/[CuII] Ratio on the Kinetics and Conformation of Polyelectrolyte Brushes by Atom Transfer Radical Polymerization. *Macromolecular Rapid Communications* **2006**, *27*, 1632 – 1636.

[71] Moya, S. E.; Brown, A. A.; Azzaroni, O.; Huck, W. T. S. Following Polymer Brush Growth Using the Quartz Crystal Microbalance Technique. *Macromolecular Rapid Communications* **2005**, *26*, 1117 – 1121.

[72] Ballauff, M.; Borisov, O. Polyelectrolyte Brushes. *Current Opinion in Colloid &Interface Science* **2006**, *11*, 316 – 323.

[73] Lego, B.; Skene, W. G.; Giasson, S. Swelling Study of Responsive Polyelectrolyte Brushes Grafted from Mica Substrates: Effect of pH, Salt, and Grafting Density. *Macromolecules* **2010**, *43*, 4384 – 4393.

[74] Brown, A. A.; Azzaroni, O.; Fidalgo, L. M.; Huck, W. T. S. Polymer Brush Resist for Responsive Wettability. *Soft Matter* **2009**, *5*, 2738 – 2745.

[75] Lvov, Y.; Abdullayev, E. Functional Polymer-Clay Nanotube Composites with Sustained Release of Chemical Agents. *Progress in Polymer Science* **2013**, *38*, 1690 – 1719.

[76] Podsiadlo, P.; Shim, B. S.; Kotov, N. A. Polymer/Clay and Polymer/Carbon Nanotube Hybrid Organic-Inorganic Multilayered Composites Made by Sequential Layering of Nanometer Scale Films. *Coordination Chemistry Reviews* **2009**, *253*, 2835 – 2851.

[77] Firme, C. P.; Bandaru, P. R. Toxicity Issues in the Application of Carbon Nanotubes to Biological Systems. *Nanomedicine: Nanotechnology, Biology and Medicine* **2010**, *6*, 245 – 256.

[78] Baughman, R. H.; Zakhidov, A. A.; de Heer, W. A. Carbon Nanotubes–the Route Toward Applications. *Science* **2002**, *297*, 787 – 792.

[79] Vergaro, V.; Abdullayev, E.; Lvov, Y. M.; Zeitoun, A.; Cingolani, R.; Rinaldi, R.; Leporatti, S. Cytocompatibility and Uptake of Halloysite Clay Nanotubes. *Biomacromolecules* **2010**, *11*, 820 – 826.

[80] Zhao, Y.; Cavallaro, G.; Lvov, Y. Orientation of Charged Clay Nanotubes in Evaporating Droplet Meniscus. *Journal of Colloid and Interface Science* **2015**, *440*, 68 – 77.

[81] Cavallaro, G.; Lazzara, G.; Milioto, S. Exploiting the Colloidal Stability and Solubilization Ability of Clay Nanotubes/Ionic Surfactant Hybrid Nanomaterials. *The Journal of Physical Chemistry C* **2012**, *116*, 21932 – 21938.

[82] Cavallaro, G.; Lazzara, G.; Milioto, S.; Parisi, F.; Sanzillo, V. Modified Halloysite Nanotubes: Nanoarchitectures for Enhancing the Capture of Oils from Vapor and Liquid Phases. *ACS Applied Materials &Interfaces* **2014**, *6*, 606 – 612.

[83] Lvov, Y.; Wang, W.; Zhang, L.; Fakhrullin, R. Halloysite Clay Nanotubes for Loading and Sustained Release of Functional Compounds. *Advanced Materials* **2016**, *28*, 1227 – 1250.

[84] Yah, W. O.; Takahara, A.; Lvov, Y. M. Selective Modification of Halloysite Lumen with Octadecylphosphonic Acid: New Inorganic Tubular Micelle. *Journal of the American Chemical Society* **2012**, *134*, 1853 – 1859.

[85] Yah, W. O.; Xu, H.; Soejima, H.; Ma, W.; Lvov, Y.; Takahara, A. Biomimetic Dopamine Derivative for Selective Polymer Modification of Halloysite Nanotube Lumen. *Journal of the American Chemical Society* **2012**, *134*, 12134 – 12137.

[86] Joshi, A.; Abdullayev, E.; Vasiliev, A.; Volkova, O.; Lvov, Y. Interfacial Modification of Clay Nanotubes for the Sustained Release of Corrosion Inhibitors. *Langmuir* **2013**, *29*, 7439 – 7448.

[87] Levis, S.; Deasy, P. Use of Coated Microtubular Halloysite for the Sustained Release of Diltiazem Hydrochloride and Propranolol Hydrochloride. *International Journal of Pharmaceutics* **2003**, *253*, 145 – 157.

[88] Lu, W.; Lieber, C. M. Nanoelectronics from the Bottom up. *Nature Materials* **2007**, *6*, 841.

[89] Ariga, K.; Yamauchi, Y.; Rydzek, G.; Ji, Q.; Yonamine, Y.; Wu, K. C.-W.; Hill, J. P. Layer-by-Layer Nanoarchitectonics: Invention, Innovation, and Evolution. *Chemistry Letters* **2014**, *43*, 36 – 68.

[90] de Vos, W. M.; de Keizer, A.; Stuart, M. A. C.; Kleijn, J. M. Thin Polymer Films as Sacrificial Layers for Easier Cleaning. *Colloids and Surfaces A: Physicochemical and Engineering Aspects* **2010**, *358*, 6 – 12.

[91] Moya, S. E.; Iturri Ramos, J. J.; Llarena, I. Templation, Water Content, and Zeta Potential of Polyelectrolyte Nanoassemblies: a Comparison Between Polyelectrolyte Multilayers and Brushes. *Macromolecular Rapid Communications* **2012**, *33*, 1022 – 1035.

[92] Zhang, H.; Rühe, J. Weak Polyelectrolyte Brushes as Substrates for the Formation of Surface-Attached Polyelectrolyte-Polyelectrolyte Complexes and Polyelectrolyte Multilayers. *Macromolecules* **2005**, *38*, 10743 – 10749.

[93] Laurent, P.; Souharce, G.; Duchet-Rumeau, J.; Portinha, D.; Charlot, A. 'Pancake' vs. Brush-Like Regime of Quaternizable Polymer Grafts: An Efficient Tool for Nano-Templating Polyelectrolyte Self-Assembly. *Soft Matter* **2012**, *8*, 715 – 725.

[94] Matyjaszewski, K.; Tsarevsky, N. V. Nanostructured Functional Materials Prepared by Atom Transfer Radical Polymerization. *Nature chemistry* **2009**, *1*, 276 – 288.

[95] Usuki, A.; Kojima, Y.; Kawasumi, M.; Okada, A.; Fukushima, Y.; Kurauchi, T.; Kamigaito, O. Synthesis of Nylon 6-Clay Hybrid. *Journal of Materials Research* **1993**, *8*, 1179 – 1184.

[96] Alexandre, M.; Dubois, P. Polymer-Layered Silicate Nanocomposites: Preparation, Properties and Uses of a New Class of Materials. *Materials Science and Engineering: R: Reports* **2000**, *28*, 1 – 63.

[97] Hammond, P. Form and Function in Multilayer Assembly: New Applications at the Nanoscale. *Advanced Materials* **2004**, *16*, 1271 – 1293.

[98] Paul, D.; Robeson, L. Polymer Nanotechnology: Nanocomposites. *Polymer* **2008**, *49*, 3187 – 3204.

[99] Boyaciyan, D.; Krause, P.; von Klitzing, R. Making Strong Polyelectrolyte Brushes pH-Sensitive by Incorporation of Gold Nanoparticles. *Soft Matter* **2018**, *14*, 4029 – 4039.

[100] Zhuk, A.; Mirza, R.; Sukhishvili, S. Multiresponsive Clay-Containing Layer-by-Layer Films. *ACS Nano* **2011**, *5*, 8790 – 8799.

[101] Sekar, S.; Lemaire, V.; Hu, H.; Decher, G.; Pauly, M. Anisotropic Optical and Conductive Properties of Oriented 1D-Nanoparticle Thin Films Made by Spray-Assisted Self-Assembly. *Faraday Discussions* **2016**, *191*, 373 – 389.

[102] Hu, H.; Pauly, M.; Felix, O.; Decher, G. Spray-Assisted Alignment of Layer-by-Layer Assembled Silver Nanowires: A General Approach for the Preparation of Highly Anisotropic Nano-Composite Films. *Nanoscale* **2017**, *9*, 1307 – 1314.

[103] Blell, R.; Lin, X.; Lindström, T.; Ankerfors, M.; Pauly, M.; Felix, O.; Decher, G. Generating in-Plane Orientational Order in Multilayer Films Prepared by Spray-Assisted Layer-by-Layer Assembly. *ACS Nano* **2017**, *11*, 84 – 94.

[104] Probst, P. T.; Sekar, S.; König, T. A. F.; Formanek, P.; Decher, G.; Fery, A.; Pauly, M. Highly Oriented Nanowire Thin Films with Anisotropic Optical Properties Driven by the Simultaneous Influence of Surface Templating and Shear Forces. *ACS Applied Materials & Interfaces* **2018**, *10*, 3046 – 3057.

[105] Weaver, J. C.; Milliron, G. W.; Miserez, A.; Evans-Lutterodt, K.; Herrera, S.; Gallana, I.; Mershon, W. J.; Swanson, B.; Zavattieri, P.; DiMasi, E.; Kisailus, D. The Stomatopod Dactyl Club: A Formidable Damage-Tolerant Biological Hammer. *Science* **2012**, *336*, 1275 – 1280.

[106] Kolasińska, M.; Krastev, R.; Warszyński, P. Characteristics of Polyelectrolyte Multilayers: Effect of PEI Anchoring Layer and Posttreatment after Deposition. *Journal of Colloid and Interface Science* **2007**, *305*, 46 – 56.

[107] Hall, D. B.; Underhill, P.; Torkelson, J. M. Spin Coating of Thin and Ultrathin Polymer Films. *Polymer Engineering & Science* **1998**, *38*, 2039 – 2045.

[108] Izquierdo, A.; Ono, S. S.; Voegel, J.-C.; Schaaf, P.; Decher, G. Dipping versus Spraying: Exploring the Deposition Conditions for Speeding Up Layer-by-Layer Assembly. *Langmuir* **2005**, *21*, 7558 – 7567.

[109] Tolan, M. *X-Ray Scattering from Soft-Matter Thin Films: Materials Science and Basic Research (Springer Tracts in Modern Physics)*; Springer, 1999.

[110] Parratt, L. G. Surface Studies of Solids by Total Reflection of X-Rays. *Physical Review* **1954**, *95*, 359 – 369.

[111] Voets, I. K.; de Vos, W. M.; Hofs, B.; de Keizer, A.; Conhen Stuart, M. A.; Steitz, R.; Lott, D. Internal Structure of a Thin Film of Mixed Polymeric Micelles on a Solid/Liquid Interface. *The Journal of Physical Chemistry B* **2008**, *112*, 6937 – 6945.

[112] Braun, C. Parratt32: Fitting routine for reflectivity data. **1997**, HMI Berlin.

[113] Schneck, E.; Schollier, A.; Halperin, A.; Moulin, M.; Haertlein, M.; Sferrazza, M.; Fragneto, G. Neutron Reflectometry Elucidates Density Profiles of Deuterated Proteins Adsorbed onto Surfaces Displaying Poly(ethylene glycol) Brushes: Evidence for Primary Adsorption. *Langmuir* **2013**, *29*, 14178 – 14187.

[114] Schneck, E.; Berts, I.; Halperin, A.; Daillant, J.; Fragneto, G. Neutron Reflectometry from Poly (ethylene-glycol) Brushes Binding Anti-PEG Antibodies: Evidence of Ternary Adsorption. *Biomaterials* **2015**, *46*, 95 – 104.

[115] Rodriguez-Loureiro, I.; Scoppola, E.; Bertinetti, L.; Barbetta, A.; Fragneto, G.; Schneck, E. Neutron Reflectometry Yields Distance-Dependent Structures of Nanometric Polymer Brushes Interacting across Water. *Soft Matter* **2017**, *13*, 5767 – 5777.

[116] García, R.; Pérez, R. Dynamic Atomic Force Microscopy Methods. *Surface Science Reports* **2002**, *47*, 197 – 301.

[117] Rezakhaniha, R.; Agianniotis, A.; Schrauwen, J.; Griffa, A.; Sage, D.; Bouten, C.; van de Vosse, F.; Unser, M.; Stergiopulos, N. Experimental Investigation of Collagen Waviness and Orientation in the Arterial Adventitia Using Confocal Laser Scanning Microscopy. *Biomechanics and Modeling in Mechanobiology* **2012**, *11*, 461 – 473.

[118] Schneider, C. A.; Rasband, W. S.; Eliceiri, K. W. NIH Image to ImageJ: 25 Years of Image Analysis. *Nature Methods* **2012**, *9*, 671 – 675.

[119] Yen, J.-C.; Chang, F.-J.; Chang, S. A new Criterion for Automatic Multilevel Thresholding. *IEEE Transactions on Image Processing* **1995**, *4*, 370 – 378.

[120] Bosio, V.; Dubreuil, F.; Bogdanovic, G.; Fery, A. Interactions between Silica Surfaces Coated by Polyelectrolyte Multilayers in Aqueous Environment: Comparison between Precursor and Multilayer Regime. *Colloids and Surfaces A: Physicochemical and Engineering Aspects* **2004**, *243*, 147 – 155.

[121] Schönhoff, M. Self-Assembled Polyelectrolyte Multilayers. *Current Opinion in Colloid & Interface Science* **2003**, *8*, 86 – 95.

[122] Boudou, T.; Crouzier, T.; Ren, K.; Blin, G.; Picart, C. Multiple Functionalities of Polyelectrolyte Multilayer Films: New Biomedical Applications. *Advanced Materials* **2010**, *22*, 441 – 467.

[123] Guzmán, E.; Ritacco, H.; Ortega, F.; Svitova, T.; Radke, C. J.; Rubio, R. G. Adsorption Kinetics and Mechanical Properties of Ultrathin Polyelectrolyte Multilayers: Liquid-Supported versus Solid-Supported Films. *The Journal of Physical Chemistry B* **2009**, *113*, 7128 – 7137.

[124] Glinel, K.; Déjugnat, C.; Prevot, M.; Schöler, B.; Schönhoff, M.; von Klitzing, R. Responsive Polyelectrolyte Multilayers. *Colloids and Surfaces A: Physicochemical and Engineering Aspects* **2007**, *303*, 3 – 13.

[125] Schlenoff, J. B.; Ly, H.; Li, M. Charge and Mass Balance in Polyelectrolyte Multilayers. *Journal of the American Chemical Society* **1998**, *120*, 7626 – 7634.

[126] Salomäki, M.; Vinokurov, I. A.; Kankare, J. Effect of Temperature on the Buildup of Polyelectrolyte Multilayers. *Langmuir* **2005**, *21*, 11232 – 11240.

[127] Cornelsen, M.; Helm, C. A.; Block, S. Destabilization of Polyelectrolyte Multilayers Formed at Different Temperatures and Ion Concentrations. *Macromolecules* **2010**, *43*, 4300 – 4309.

[128] Glinel, K.; Moussa, A.; Jonas, A. M.; ; Laschewsky, A. Influence of Polyelectrolyte Charge Density on the Formation of Multilayers of Strong Polyelectrolytes at Low Ionic Strength. *Langmuir* **2002**, *18*, 1408 – 1412.

[129] Wong, J. E.; Zastrow, H.; Jaeger, W.; von Klitzing, R. Specific Ion versus Electrostatic Effects on the Construction of Polyelectrolyte Multilayers. *Langmuir* **2009**, *25*, 14061 – 14070.

[130] Volodkin, D.; von Klitzing, R. Competing Mechanisms in Polyelectrolyte Multilayer Formation and Swelling: Polycation-Polyanion Pairing vs. Polyelectrolyte-Ion Pairing. *Current Opinion in Colloid & Interface Science* **2014**, *19*, 25 – 31.

[131] Köhler, K.; Shchukin, D. G.; Möhwald, H.; Sukhorukov, G. B. Thermal Behavior of Polyelectrolyte Multilayer Microcapsules: 1. The Effect of Odd and Even Layer Number. *Journal of Physical Chemistry B* **2005**, *109*, 18250 – 18259.

[132] Köhler, K.; Möhwald, H.; Sukhorukov, G. B. Thermal Behavior of Polyelectrolyte Multilayer Microcapsules: 2. Insight into Molecular Mechanisms for the PDADMAC/PSS System. *Journal of Physical Chemistry B* **2006**, *110*, 24002 – 24010.

[133] Han, Y.; Bu, J.; Zhang, Y.; Tong, W.; Gao, C. Encapsulation of Photosensitizer into Multilayer Microcapsules by Combination of Spontaneous Deposition and Heat-Induced Shrinkage for Photodynamic Therapy. *Macromolecular Bioscience* **2012**, *12*, 1436 – 1442.

[134] Malcher, M.; Volodkin, D.; Heurtault, B.; André, P.; Schaaf, P.; Möhwald, H.; Voegel, J.-C.; Sokolowski, A.; Ball, V.; Boulmedais, F.; Frisch, B. Embedded Silver Ions-Containing Liposomes in Polyelectrolyte Multilayers: Cargos Films for Antibacterial Agents. *Langmuir* **2008**, *24*, 10209 – 10215.

[135] Velk, N.; Uhlig, K.; Vikulina, A.; Duschl, C.; Volodkin, D. Mobility of Lysozyme in Poly(l-lysine)/Hyaluronic Acid Multilayer Films. *Colloids and Surfaces B: Biointerfaces* **2016**, *147*, 343 – 350.

[136] Schlenoff, J. B.; Dubas, S. T. Mechanism of Polyelectrolyte Multilayer Growth: Charge Overcompensation and Distribution. *Macromolecules* **2001**, *34*, 592 – 598.

[137] Rehfeldt, F.; Tanaka, M.; Pagnoni, L.; Jordan, R. Static and Dynamic Swelling of Grafted Poly(2-alkyl-2-oxazoline)s. *Langmuir* **2002**, *18*, 4908 – 4914.

[138] `http://www.python.org`, Python Software Foundation. Python Language Reference, version 2.7.6. Available at http://www.python.org.

[139] Lösche, M.; Schmitt, J.; Decher, G.; Bouwman, W. G.; Kjaer, K. Detailed Structure of Molecularly Thin Polyelectrolyte Multilayer Films on Solid Substrates as Revealed by Neutron Reflectometry. *Macromolecules* **1998**, *31*, 8893 – 8906.

[140] Delajon, C.; Gutberlet, T.; Möhwald, H.; Krastev, R. Absorption of Light and Heavy Water Vapours in Polyelectrolyte Multilayer Films. *Colloids and Surfaces B: Biointerfaces* **2009**, *74*, 462 – 467.

[141] Bertrand, P.; Jonas, A.; Laschewsky, A.; Legras, R. Ultrathin Polymer Coatings by Complexation of Polyelectrolytes at Interfaces: Suitable Materials, Structure and Properties. *Macromolecular Rapid Communications* **2000**, *21*, 319 – 348.

[142] Jessel, N.; Atalar, F.; Lavalle, P.; Mutterer, J.; Decher, G.; Schaaf, P.; Voegel, J.-C.; Ogier, J. Bioactive Coatings Based on a Polyelectrolyte Multilayer Architecture Functionalized by Embedded Proteins. *Advanced Materials* **2003**, *15*, 692 – 695.

[143] Schmitt, J.; Decher, G.; Dressick, W. J.; Brandow, S. L.; Geer, R. E.; Shashidhar, R.; Calvert, J. M. Metal Nanoparticle/Polymer Superlattice Films: Fabrication and Control of Layer Structure. *Advanced Materials* **1997**, *9*, 61 – 65.

[144] Parakhonskiy, B.; Yashchenok, A.; Möhwald, H.; Volodkin, D.; Skirtach, A. Release from Polyelectrolyte Multilayer Capsules in Solution and on Polymeric Surfaces. *Advanced Materials Interfaces* **2017**, *4*, 1600273.

[145] Bruening, M. L.; Dotzauer, D. M.; Jain, P.; Ouyang, L.; Baker, G. L. Creation of Functional Membranes Using Polyelectrolyte Multilayers and Polymer Brushes. *Langmuir* **2008**, *24*, 7663 – 7673.

[146] Kesal, D.; Christau, S.; Krause, P.; Möller, T.; von Klitzing, R. Uptake of pH-Sensitive Gold Nanoparticles in Strong Polyelectrolyte Brushes. *Polymers* **2016**, *8*, 134.

[147] Kawasumi, M.; Hasegawa, N.; Kato, M.; Usuki, A.; Okada, A. Preparation and Mechanical Properties of Polypropylene-Clay Hybrids. *Macromolecules* **1997**, *30*, 6333 – 6338.

[148] Nolte, A. J.; Rubner, M. F.; Cohen, R. E. Creating Effective Refractive Index Gradients within Polyelectrolyte Multilayer Films: Molecularly Assembled Rugate Filters. *Langmuir* **2004**, *20*, 3304 – 3310.

[149] Gilman, J. W.; Jackson, C. L.; Morgan, A. B.; Harris, R.; Manias, E.; Giannelis, E. P.; Wuthenow, M.; Hilton, D.; Phillips, S. H. Flammability Properties of Polymer-Layered-Silicate Nanocomposites. Polypropylene and Polystyrene Nanocomposites. *Chemistry of Materials* **2000**, *12*, 1866 – 1873.

[150] Correa-Duarte, M. A.; Grzelczak, M.; Salgueiriño Maceira, V.; Giersig, M.; Liz-Marzán, L. M.; Farle, M.; Sierazdki, K.; Diaz, R. Alignment of Carbon Nanotubes under Low Magnetic Fields through Attachment of Magnetic Nanoparticles. *The Journal of Physical Chemistry B* **2005**, *109*, 19060 – 19063.

[151] Huang, X.; El-Sayed, I. H.; Qian, W.; El-Sayed, M. A. Cancer Cells Assemble and Align Gold Nanorods Conjugated to Antibodies to Produce Highly Enhanced, Sharp, and Polarized Surface Raman Spectra: A Potential Cancer Diagnostic Marker. *Nano Letters* **2007**, *7*, 1591 – 1597.

[152] Alkilany, A. M.; Murphy, C. J. Toxicity and Cellular Uptake of Gold Nanoparticles: What we have learned so far? *Journal of Nanoparticle Research* **2010**, *12*, 2313 – 2333.

[153] Yuan, P.; Southon, P. D.; Liu, Z.; Green, M. E. R.; Hook, J. M.; Antill, S. J.; Kepert, C. J. Functionalization of Halloysite Clay Nanotubes by Grafting with γ-Aminopropyltriethoxysilane. *The Journal of Physical Chemistry C* **2008**, *112*, 15742 – 15751.

[154] Kim, M. J.; Shin, S. Toxic Effects of Silver Nanoparticles and Nanowires on Erythrocyte Rheology. *Food and Chemical Toxicology* **2014**, *67*, 80 – 86.

[155] Sadeghpour, A.; Pirolt, F.; Glatter, O. Submicrometer-Sized Pickering Emulsions Stabilized by Silica Nanoparticles with Adsorbed Oleic Acid. *Langmuir* **2013**, *29*, 6004 – 6012.

Appendix

Supporting Information for Chapter 4

X-Ray Reflectivity Data

Eillpsometry data were compared with X-Ray reflectometry data to validate the model for ellipsometry measurements. Figure 7.1 shows X-Ray reflectivity data and the corresponding fits.

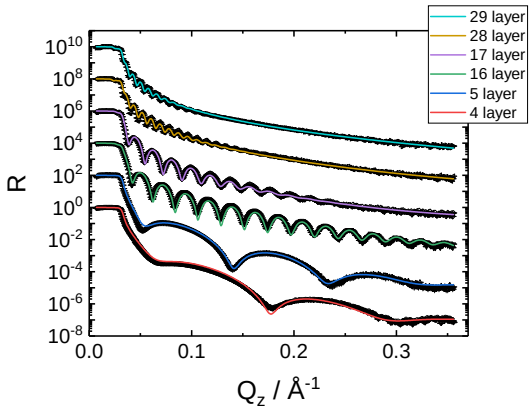

Figure 7.1: X-Ray reflectivity data (open symbols) and corresponding best fits (solid lines) as function of layer number.

Garnett Model

J. C. Maxwell Garnett reported on a correlation between the optical properties and the volume fraction in metal glasses and metallic films.[50,51] Later on it was shown that this can also be adopted to PEM-water systems.[37,137] It is possible to calculate iteratively the permittivity $\epsilon_{swollen}$ of the system with respect to the polymer volume fraction $(1-S)$:

$$\epsilon_{swollen} = \epsilon_{H2O}\left\{1 + \frac{3(1-S)}{\left(\frac{\epsilon_{dry}+2\epsilon_{H_2O}}{\epsilon_{dry}-\epsilon_{H_2O}}\right) - (1-S)}\right\} \tag{7.1}$$

Here, ϵ_{H_2O} is the permittivity of water (1.777) and ϵ_{dry} the permittivity of the dry polymer. To compare the data with measured values, the results were transformed to the refactive index by $n = \sqrt{\epsilon}$.

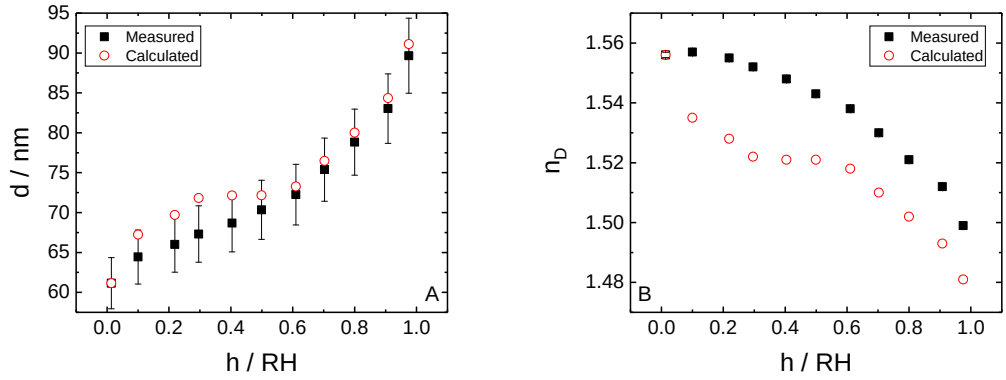

Figure 7.2: (A) Comparison of measured (closed squares) and calculated (open triangles) thicknesses for a PEM of 29 single layers as a function of humidity. The thickness is fitted with the recalculated values of the refractive index calculated with Equation 7.1. (B) Comparison of measured (closed squares) and calculated refractive (open triangles) indices for a PEM of 29 single layers.

All experimental data are compared with this theoretical model. As an example, Figure 7.2A shows the comparison of the measured thickness and calculated thicknesses by the Garnett model for a $(PSS/PDADMAC)_{14}/PSS$ PEM. The calculated thicknesses are higher than the measured values. Especially at low humidity, the calculated values differ significantly from the measured ones. At higher humidity calculated values are higher but within the error bars and also both, measured and calculated values, describe a nonlinear swelling behavior. In contrast, the calculated refractive indices are on average 0.01 lower than the measured ones as shown in Figure 7.2B. The trend of the refractive index as a function of h is the same at high humidity but does not match at low humidity.

The Garnett model assumes a 2-compound system in humid air (polymer + water) and a compact polymer film in dry conditions, i.e. 100 % polymer without any voids. This leads to a lower refractive index of the pure polymer (without air) than the real one. The exchange between air and water during the swelling is not considered by this model and overestimates the decrease of the refractive index at low humidity.[47] Therefore, the *extended void model* was applied to describe the refractive index during changing h.

Extended Void Model

Different transition values were tried out to get best fit results. Figure 7.3 shows 3 different values for a PEM of 29 single layers. The optimizing procedure was done to get a maximal number of data points into increasing region without getting values larger than one. A value larger than one for parameter a has no physical meaning due to the definition of Equation 7.3.

$$\epsilon_{swollen} = S \cdot \epsilon_{H_2O} + (1 - S) \cdot [x \cdot \epsilon_{Poly} + (1 - x) \cdot (a \cdot \epsilon_{H_2O} + (1 - a) \cdot \epsilon_{air})] \qquad (7.2)$$

$$a = \begin{cases} b \cdot S, & \text{for } S < 0.08 \\ 1, & \text{for } S \geq 0.08 \end{cases} \tag{7.3}$$

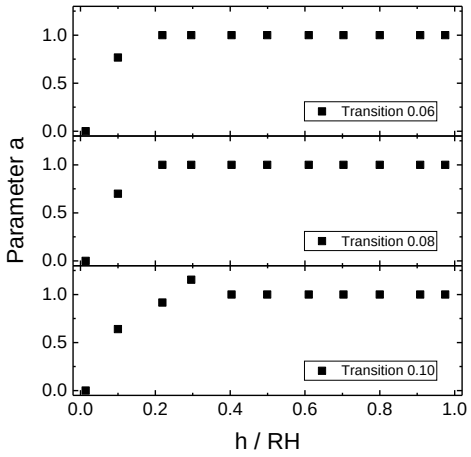

Figure 7.3: Parameter a for a PEM of 29 single layers as a function of relative humidity for different transition values.

Void Fraction

To compare our results with other publications the void water can be converted to the void fraction by

$$x = 1 - \frac{\phi_{void}}{1 - S} \tag{7.4}$$

where x is the void fraction, ϕ_{void} the void water and S the swelling coefficient. The data are shown in Table 7.1.

Table 7.1: Comparison of different void fractions according to Equation 7.4.

Publication	ϕ_{void}	ϕ_{swell}	x
Zerball *et al.*	0.042	0.31	0.94
Delajon *et al.*	—	0.25	up to 0.75

Supporting Information for Chapter 5

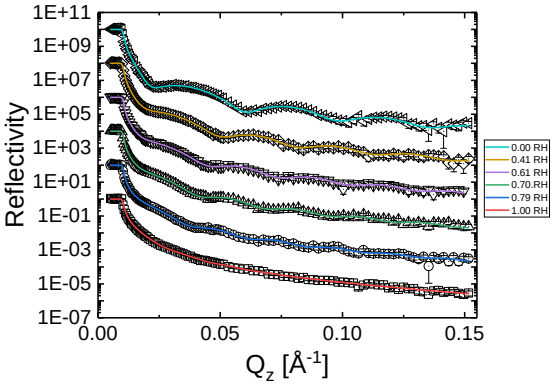

Figure 7.4: Reflectivity data and corresponding fits of the neat brush as a function of relative humidity.

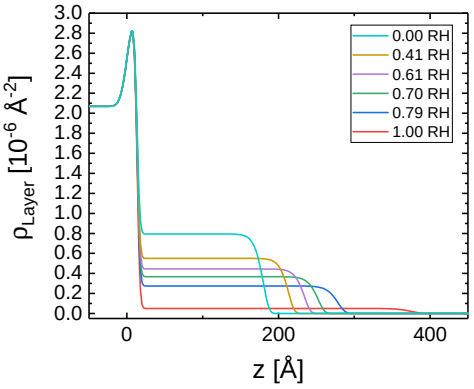

Figure 7.5: Scattering length density profiles of the neat brush as a function of relative humidity.

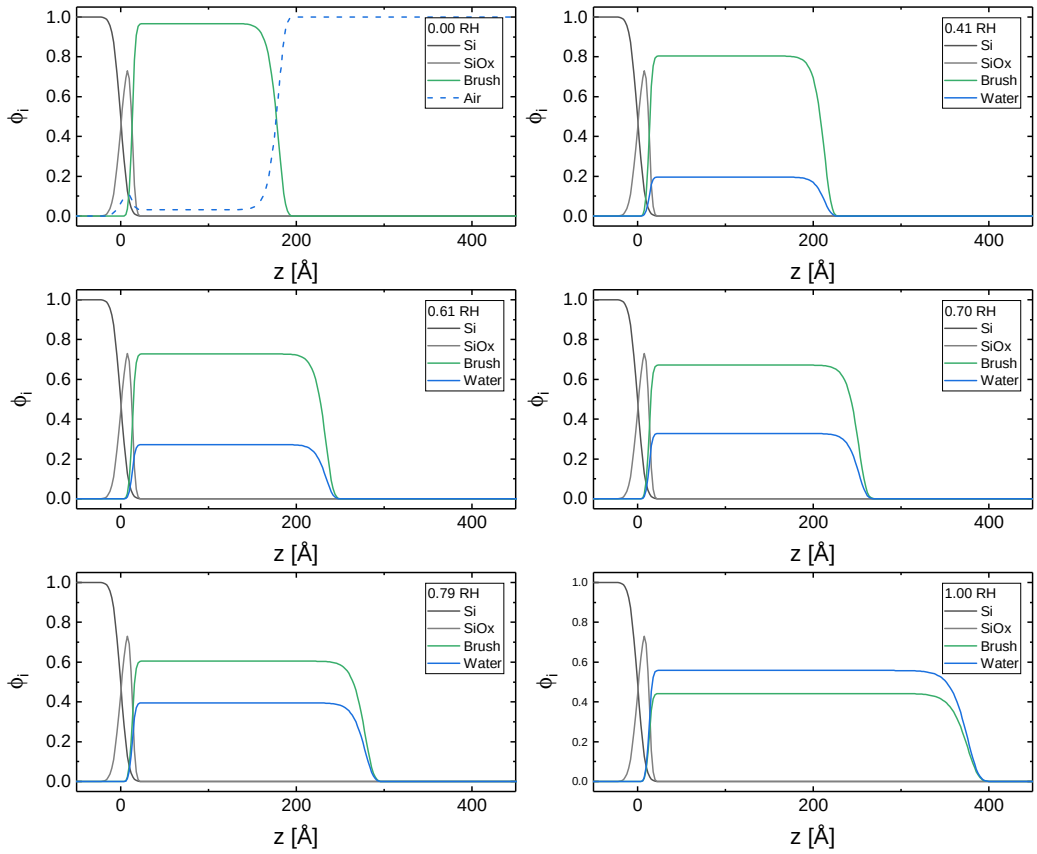

Figure 7.6: Volume fraction profiles of the neat brush as a function of relative humidity.

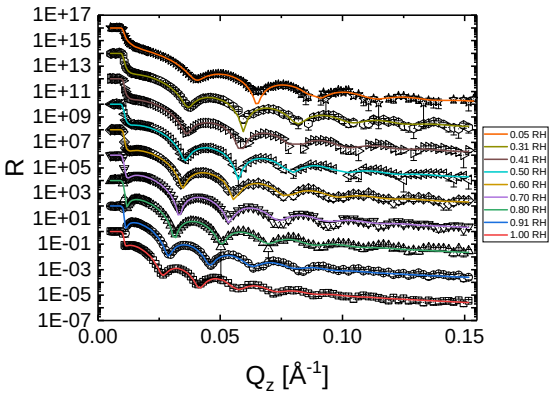

Figure 7.7: Reflectivity data and corresponding fits of the thin composite as a function of relative humidity.

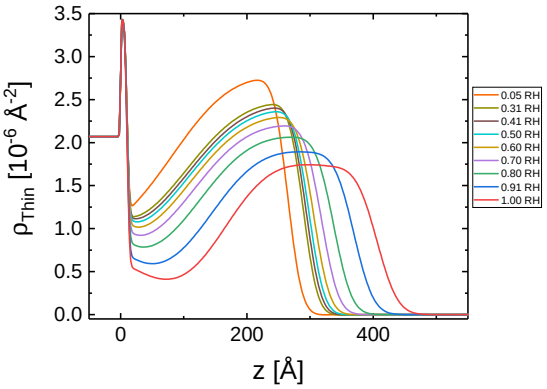

Figure 7.8: Scattering length density profiles of the thin composite as a function of relative humidity

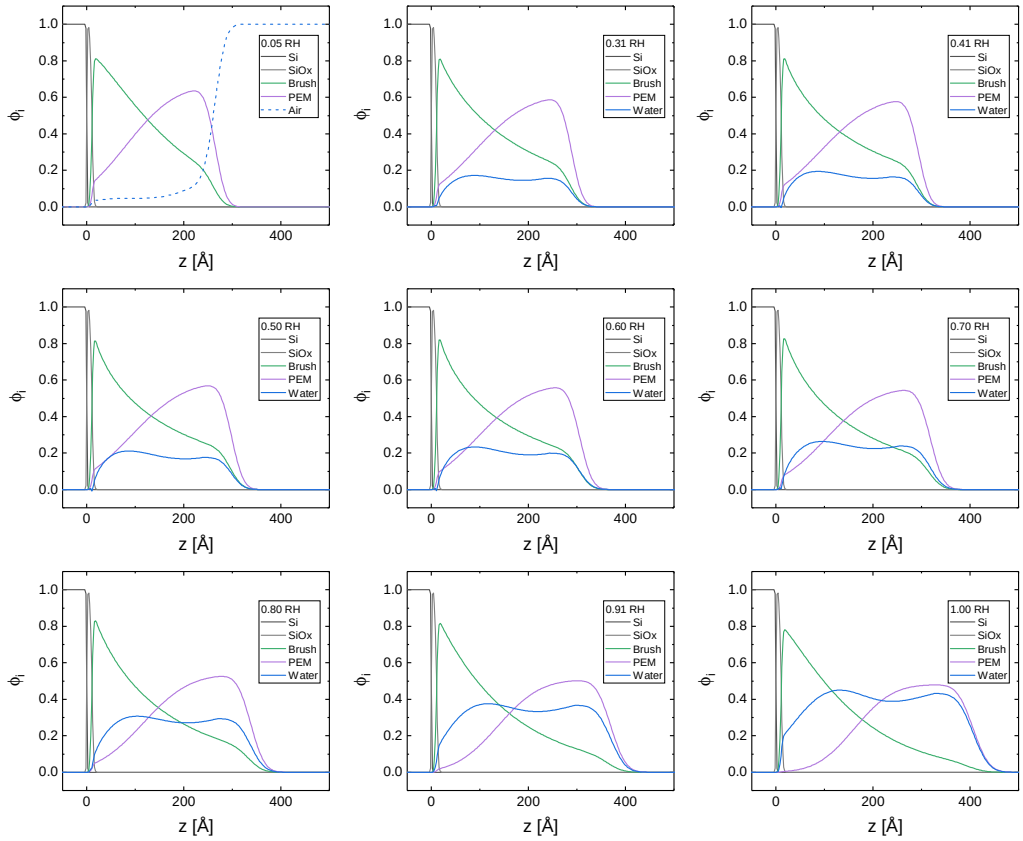

Figure 7.9: Volume fraction profiles of the thin composite as a function of relative humidity.

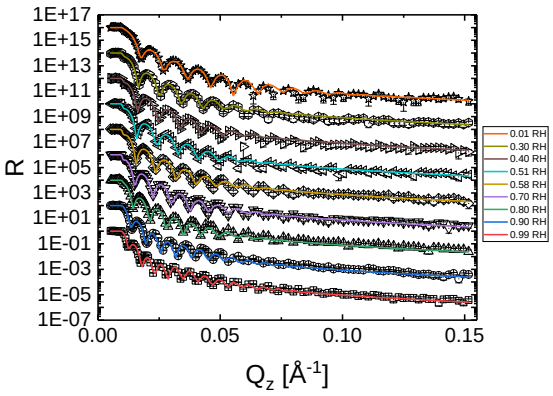

Figure 7.10: Reflectivity data and corresponding fits of the thick composite as a function of relative humidity.

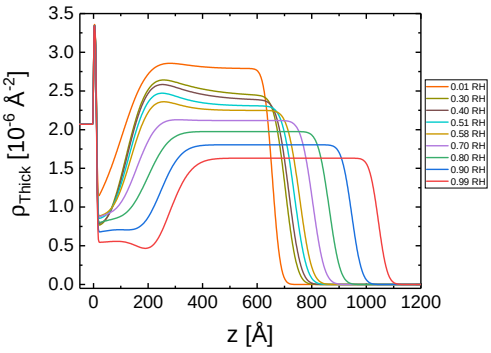

Figure 7.11: Scattering length density profiles of the thick composite as a function of relative humidity

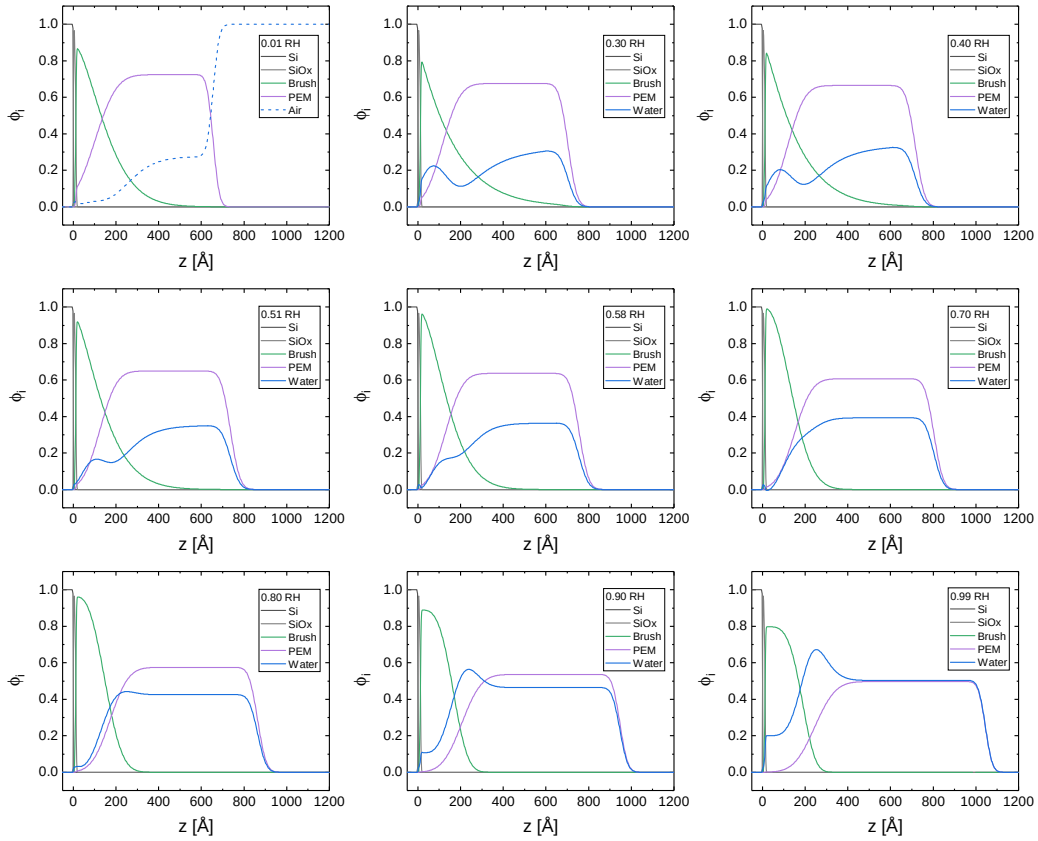

Figure 7.12: Volume fraction profiles of the thick composite as a function of relative humidity.